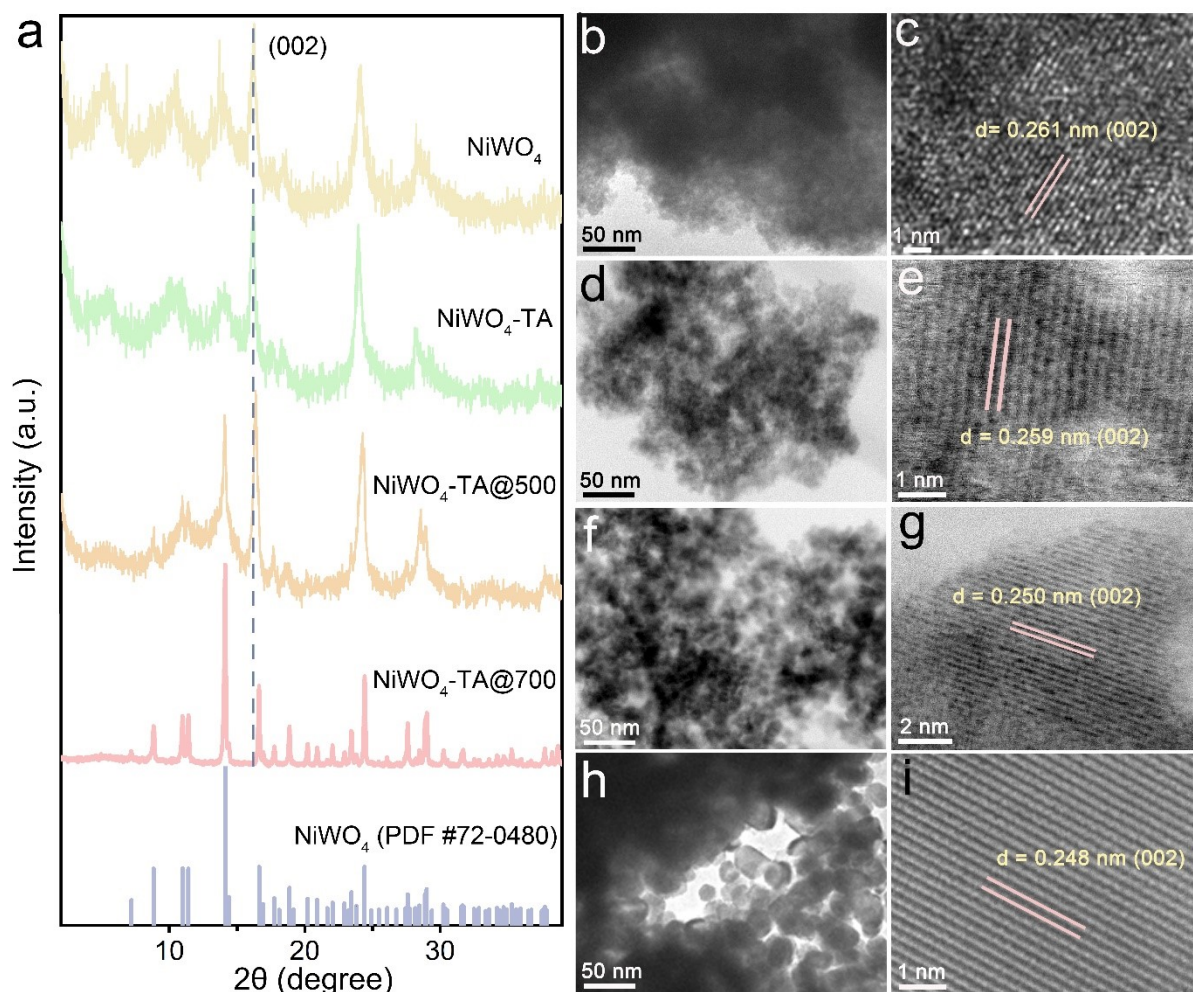## Supplementary Information


Supplementary Fig. 1 Structural and morphological characterization of as-prepared NiWO$_4$-based electrocatalysts. a Powder XRD patterns of NiWO$_4$ and its TA-hybridized derivatives. **b-i** TEM micrographs of (**b, c**) NiWO$_4$, (**d, e**) NiWO$_4$-TA, (**f, g**) NiWO$_4$-TA@500 and (**h, i**) NiWO$_4$-TA@700, respectively.

The synthesis of NiWO$_4$ or NiWO$_4$-TA was performed by a one-step wet-chemistry approach. X-ray diffraction (XRD) patterns in Supplementary Fig. 1a show a pseudo-crystallinity among the hydrothermally-manufactured samples, owing to which only their prominent lattice planes can be clearly identified. After annealing at 500 ^{o}C, the resulted hybrid (NiWO$_4$-TA@500) exhibits increased crystallinity as confirmed by its XRD pattern. Full crystallization of the bimetal oxide was achieved when further raised the sintering temperature to 700 ^{o}C (NiWO$_4$-TA@700). It is noteworthy that the (002) diffraction peak (at 2theta = 14 degree) shifts to higher angle after calcination.

Transmission electron microscopy (TEM) measurement was performed to reveal the impact of carbon substrate and annealing temperature on the morphology of the as-prepared catalysts, as demonstrated in Supplementary Fig. 1b-i. It was unravelled that the bimetal oxide sample possesses a dense structure (Supplementary Fig. 1b), whereas for the NiWO$_4$-TA hybrid, NiWO$_4$ nanocrystals grow on the hydrochar homogeneously (Supplementary Fig. 1d). This can be ascribed to the dispersed nucleation sites due to the addition of TA. As for the annealed samples (NiWO$_4$-TA@500 and NiWO$_4$-TA@700), nanoparticle aggregation (Supplementary Fig. 1f and h), lattice shrinkage and lattice structural integrity (Supplementary Fig. 1c, e, g and i) were witnessed after sintering, pointing to the improved crystallinity, which are in

accordance with the XRD analysis.
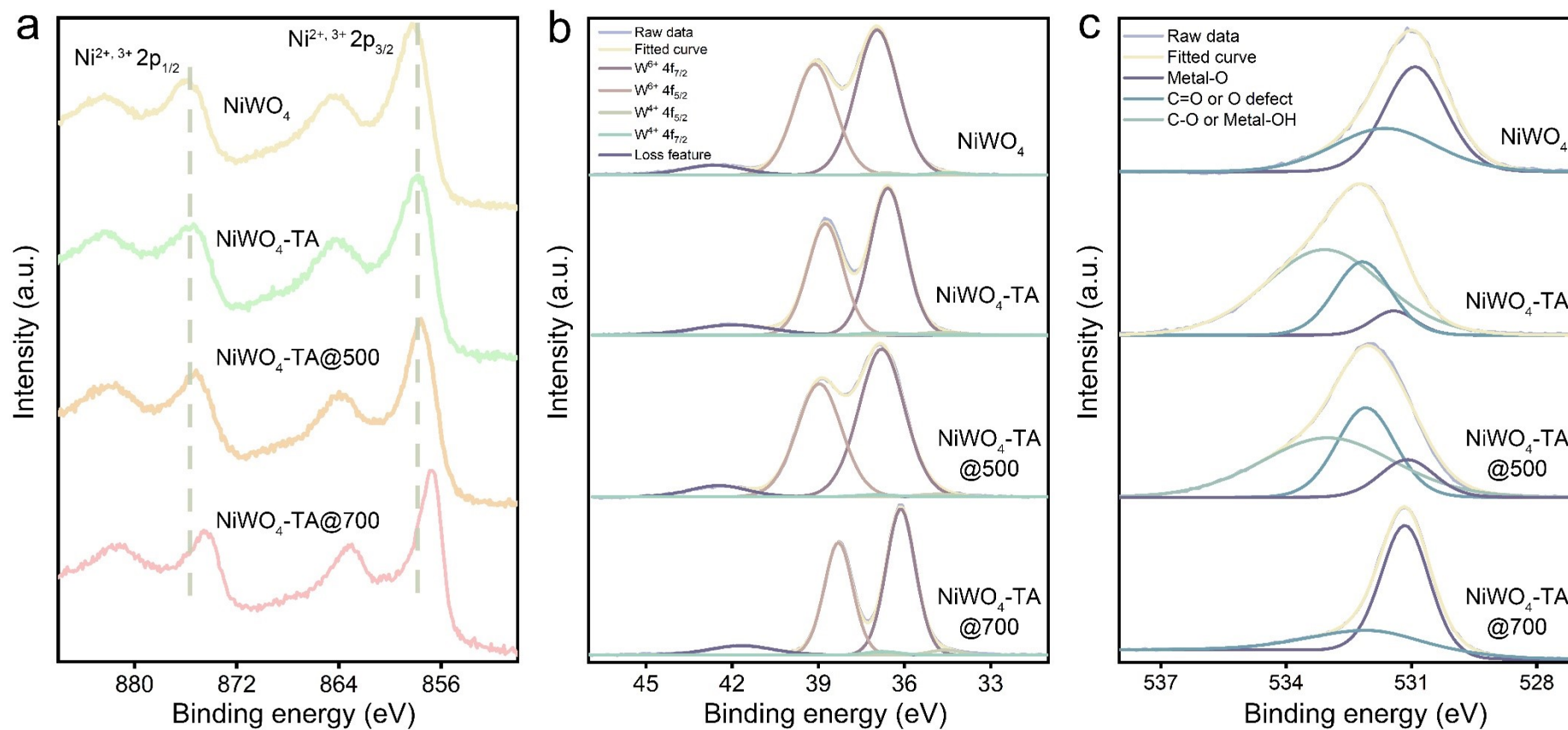
Supplementary Fig. 2 XPS spectra of **a** Ni 2p, **b** W 4f, and **c** O 1s peaks for the NiWO$_4$-based electrocatalysts.

The surface elemental compositions and chemical states of the as-synthesized catalysts were analysed by X-ray photoelectron spectroscopy (XPS) measurement. The peaks around 856-858 eV (dashed lines) in Supplementary Fig. 2a represent surface Ni in 2+ (oxide or hydroxide) or 3+ (oxyhydroxide) oxidation states. It is worth noting that the shift of Ni spin-orbit peaks of the annealed samples to lower binding energy can be attributed to the conversion of their surface oxyhydroxide component to oxide by calcination. Differently, as demonstrated in Supplementary Fig. 2b, the valence state of W, of which W^{6+} species is dominant, remains stable after sintering. XPS O 1s spectra (Supplementary Fig. 2c) reveal the presence of metal-oxygen bond in all samples which can be assigned to metal oxide/(oxy)hydroxide units.
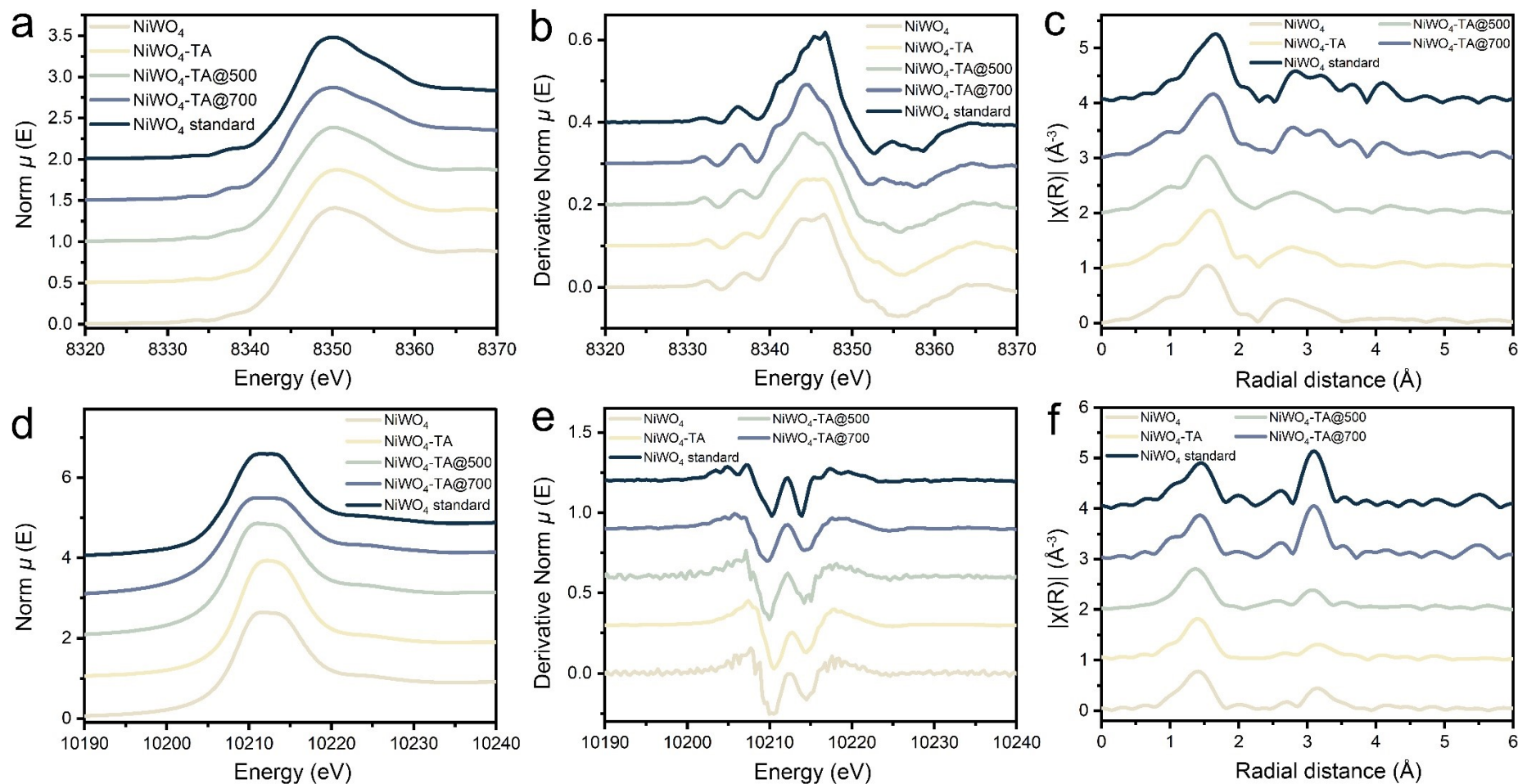
Supplementary Fig. 3 Ni K-edge and W L₃-edge XAFS spectra of NiWO₄ sample series. a-c Ni K-edge (**a**) X-ray absorption near edge structure (XANES), (**b**) second derivative XANES and (**c**) k^2-weighted R-space extended X-ray absorption fine structure (EXAFS) of NiWO₄, NiWO₄-TA, NiWO₄-TA@500, NiWO₄-TA@700 and commercial NiWO₄. **d-f** W L₃-edge (**d**) XANES, (**e**) second derivative XANES and (**f**) k^2-weighted R-space EXAFS of NiWO₄, NiWO₄-TA, NiWO₄-TA@500, NiWO₄-TA@700 and commercial NiWO₄. It can be concluded from the EXAFS that after 700 ℃ calcination, the coordination environment of both Ni and W in NiWO₄-TA@700 is nearly identical to that of the commercial NiWO₄ sample. While the sample without calcination or calcined at 500 ℃ show much weaker second shell scattering features. This

corresponds well with the XRD characterisation, in which significantly improved crystallinity was obtained after 700 $^{\circ}$C calcination.
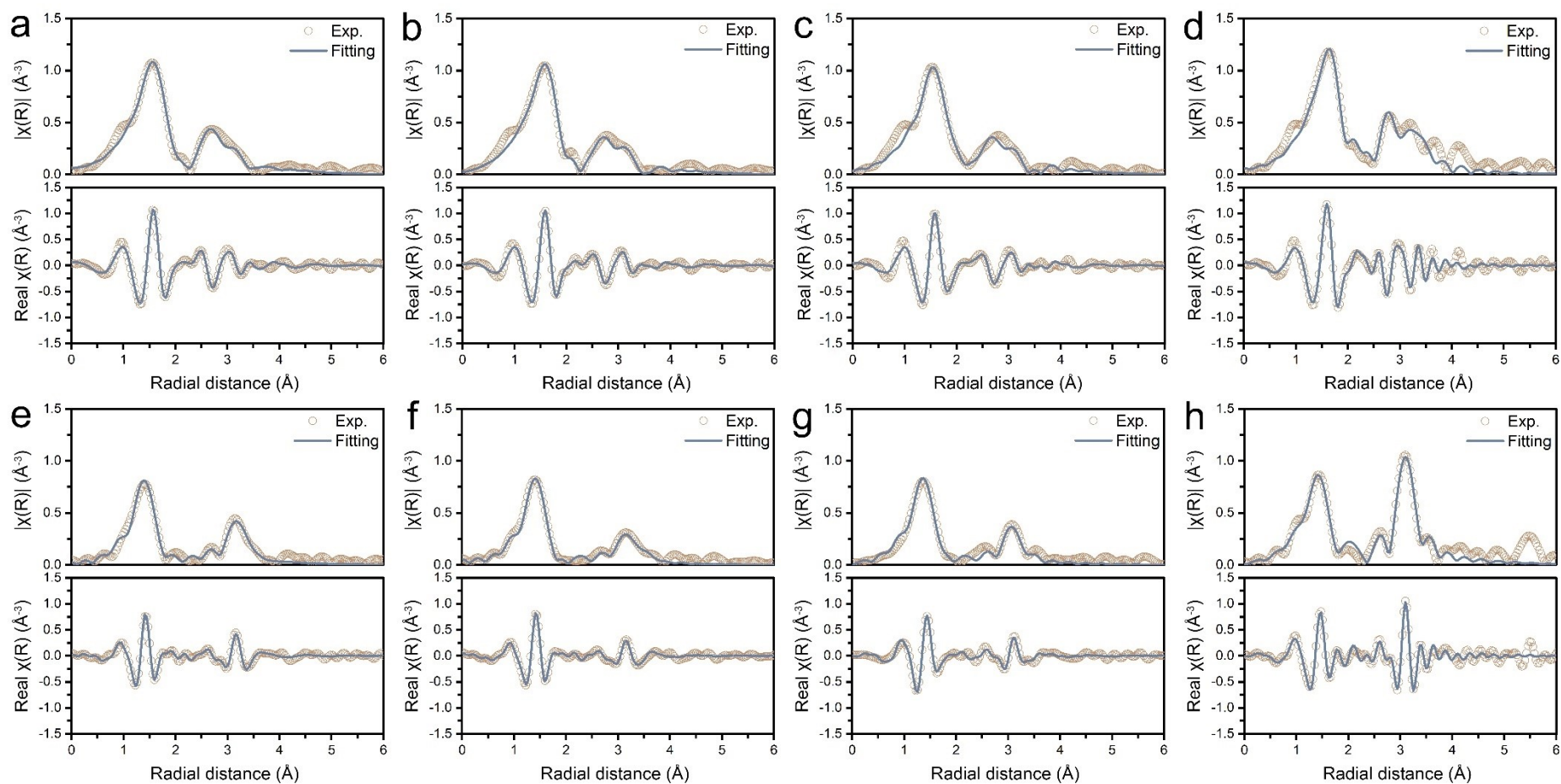
Supplementary Fig. 4 a-d Fitting results of Ni K-edge EXAFS spectra of **(a)** NiWO$_4$, **(b)** NiWO$_4$-TA, **(c)** NiWO$_4$-TA@500 and **(d)** NiWO$_4$-

TA@700. **e-h** Fitting results of W L$_3$-edge EXAFS spectra of (**e**) NiWO$_4$, (**f**) NiWO$_4$-TA, (**g**) NiWO$_4$-TA@500 and (**h**) NiWO$_4$-TA@700. The raw experiment data are plotted in circles, and the fitting results are plotted as cyan curves. The corresponding fitting parameters are presented in Supplementary Table 1.
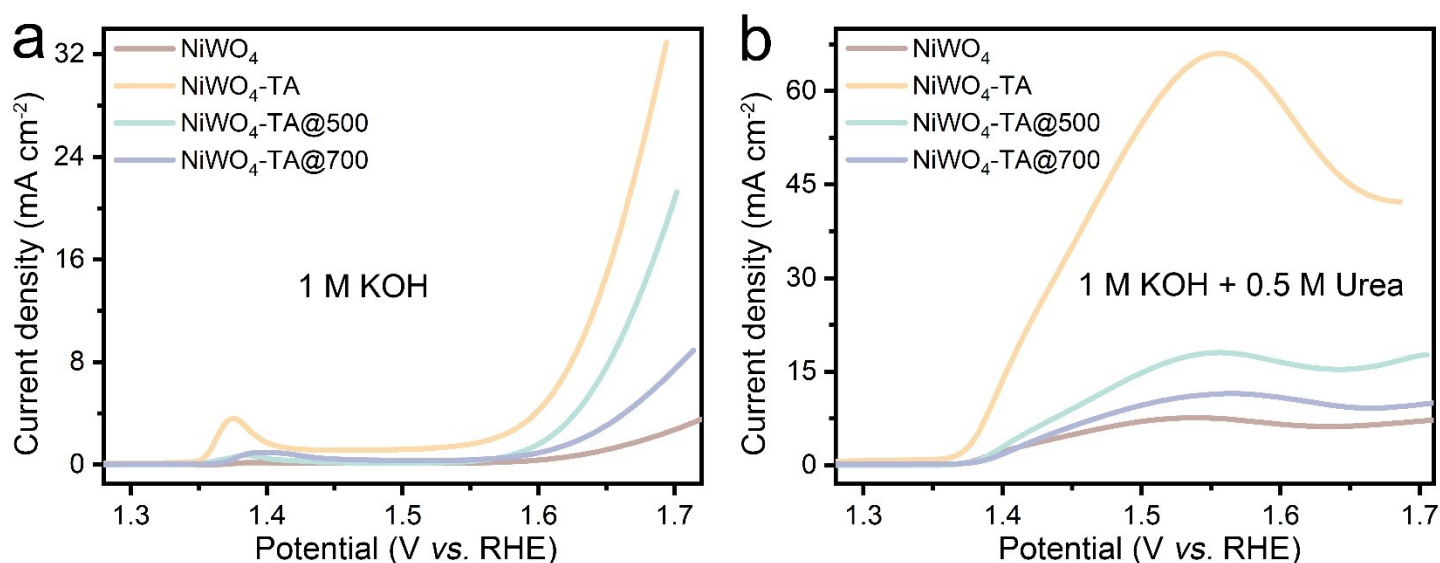

Supplementary Fig. 5 Linear sweep voltammetry (LSV) curves of NiWO$_4$, NiWO$_4$-TA, NiWO$_4$-TA@500 and NiWO$_4$-TA@700 scanned in **a** 1 M KOH and **b** 1 M KOH + 0.5 M urea. An improved water and urea electrolysis performance of NiWO$_4$ can be witnessed after hybridisation with TA. The TA delivered two functions. First, TA provides sufficient nucleation sites, leading to a more homogeneous growth of the NiWO$_4$ particles; second, TA behaves as an electron-conductive support for the semi-conductive NiWO$_4$. Accordingly, NiWO$_4$-TA shows much higher ECSA (Supplementary Fig. 34 and 54) and catalytic activity than that of NiWO$_4$. The decreased activity of the annealed samples (NiWO$_4$-TA@500 and NiWO$_4$-TA@700) can be explained by the elimination of surface oxyhydroxide species (as discussed in the XPS Ni 2p spectra shown in Supplementary Fig. 2a). According to previous literatures, surface oxyhydroxide shows excellent wettability, thus facilitating ion transfer at the electrolyte/catalyst interface.[1] Furthermore, NiOOH can behave as an active centre, directly catalysing electrooxidation reactions.[2] In addition,

aggregation of $NiWO_4$ nanoparticle is witnessed after sintering (the TEM images of $NiWO_4$-TA@500 and $NiWO_4$-TA@700 in Supplementary Fig. 1f and h, respectively). With all the reasons mentioned above, $NiWO_4$-TA shows decreased activity after calcination.
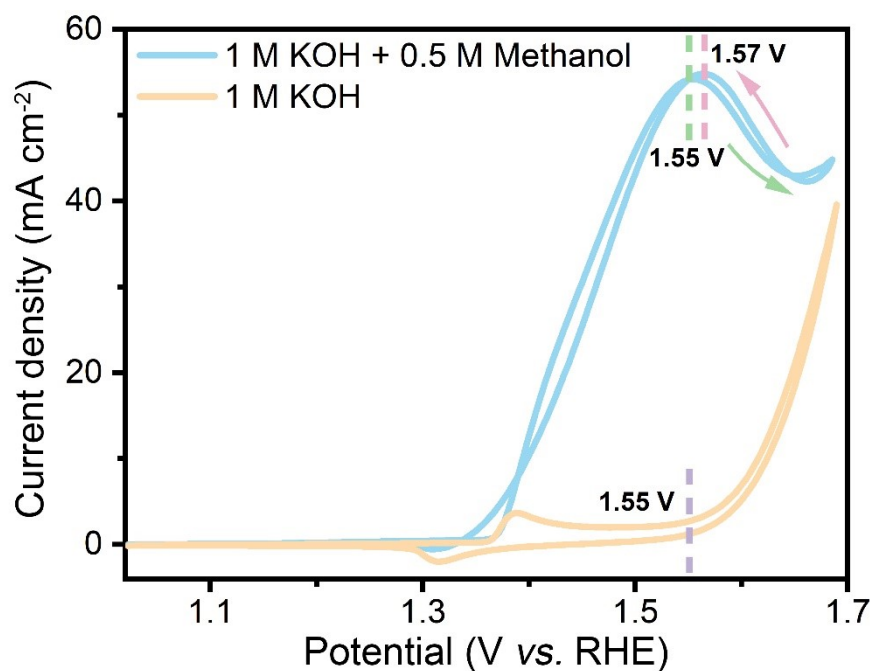
Supplementary Fig. 6 Cyclic voltammetry (CV) curves of $NiWO_4$-TA scanned in 1 M KOH electrolyte with (blue) and without (orange) 0.5 M methanol.
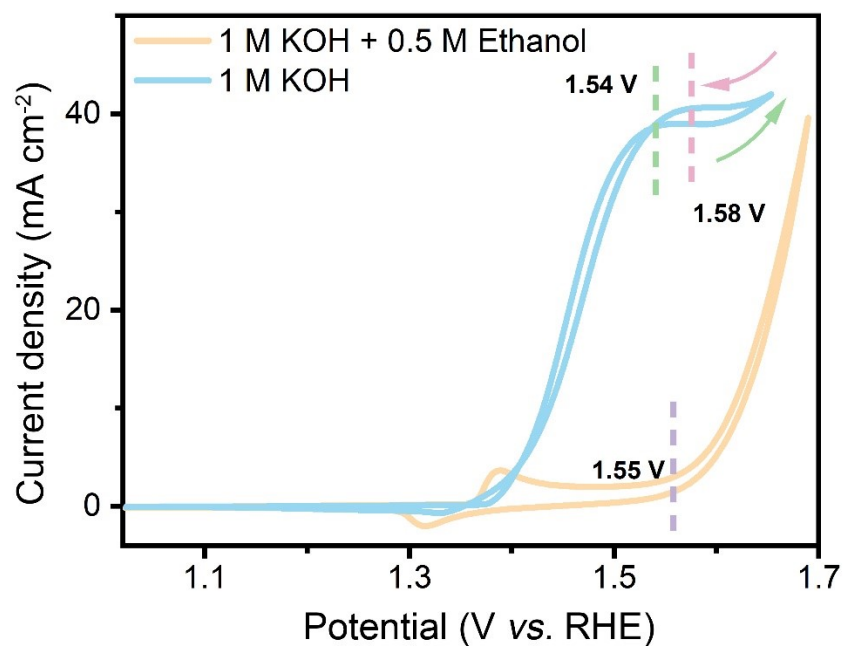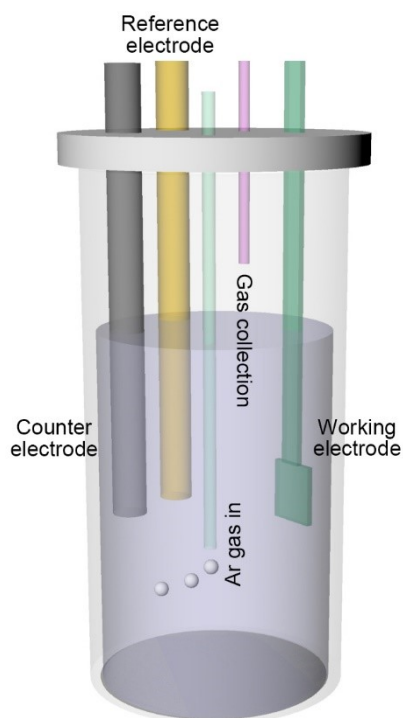
Supplementary Fig. 7 Cyclic voltammetry (CV) curves of NiWO$_4$-TA scanned in 1 M KOH electrolyte with (blue) and without (orange) 0.5 M ethanol.
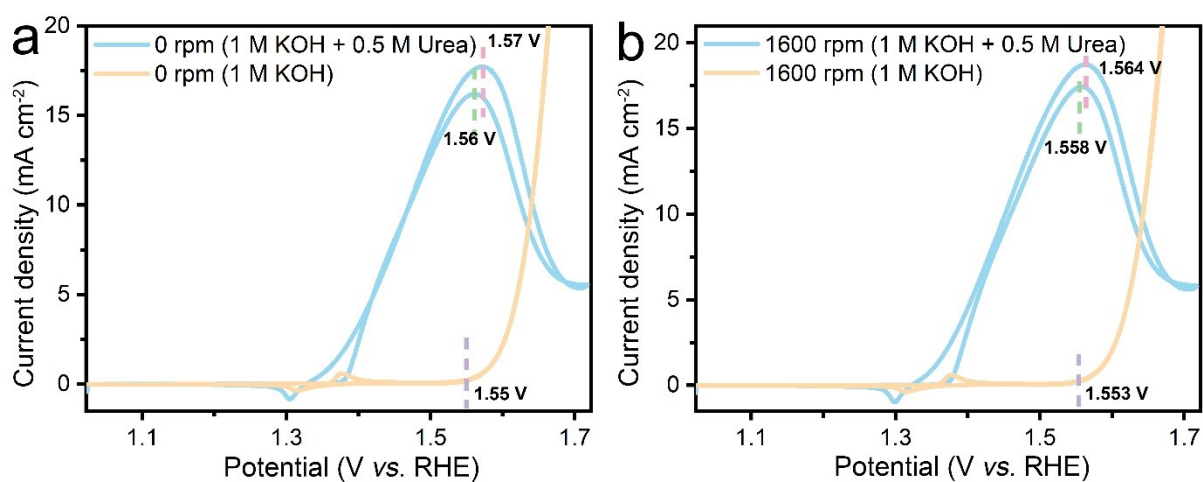
Supplementary Fig. 8 CV curves of NiWO$_4$-TA at rotation rates of **a** 0 and **b** 1600 rpm in 1 M KOH electrolyte with (blue) and without (orange) 0.5 M urea.

Supplementary Fig. 9 Schematic diagram of the real-time mass spectrometry (RTMS) set-up. The working, counter and reference electrodes were placed in a sealed electrochemical cell. Ar gas (flow rate into cell is 70 mL min^{-1}; into MS is 16 mL min^{-1}) was continuously purged into the electrolyte before (to saturate the system with Ar) and during (to transport the gaseous products produced at the working electrode out of the electrolyte) the test. A collection tube was employed to extract the gases above the electrolyte to a MS analyser. To minimize the disturbance from atmospheric gases and the time delay in product analysis, while maximizing the gas extraction efficiency, a small and slim cell is used.
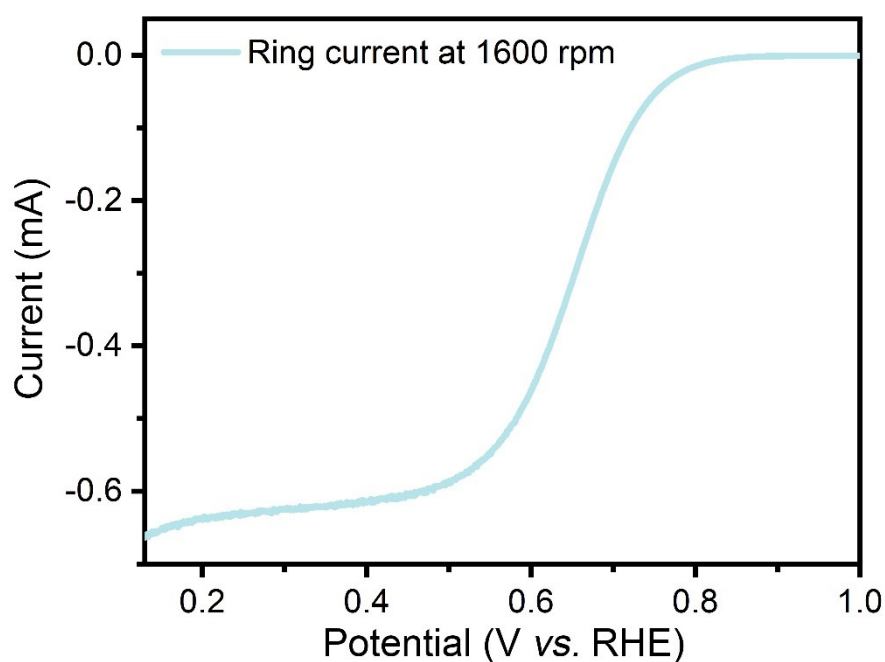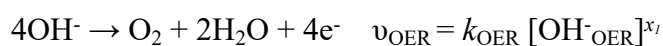
Supplementary Fig. 10 LSV of the ring current for rotation ring-disk electrode (RRDE) electrodes. The Au ring scanned in O_2-saturated 1 M KOH + 0.5 M urea electrolyte at 1600 rpm with a scan rate of 5 mV s^{-1}. The LSV obtained at 1600 rpm reveals that the reduction of O_2 on Au ring reaches diffusion limited current plateau from ~0.5 V *vs*. RHE. Hence, the ring is biased at 0.2 V *vs*. RHE (low enough for O_2 reduction but high enough to prevent H_2 evolution) during the *in situ* O_2 detection.
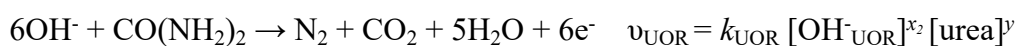
Supplementary Note 1

   To mitigate the negative impacts of the UOR/OER competition, it is important to unravel whether a selectivity shift can be achieved by manipulating the concentration of the reactants. As shown in the below equations, OH$^-$ is a shared reactant, indicating both OER and UOR will be affected by the pH of the reaction medium. Although urea only participates in UOR, any alteration of its concentration will influence the UOR reaction rate directly and indirectly affect OER reaction kinetics through a domino effect (urea concentration → UOR reaction rate → [OH$^-_{UOR}$] → [OH$^-_{OER}$] → OER reaction rate). In addition, it is likely that the intrinsic and *operando* properties of the catalyst will also be affected by the concentration variation. Therefore, the kinetic study of alkaline urea electrolysis should take into consideration not just the effects of KOH and urea concentrations on UOR, but on OER and the catalyst.

OER (in alkaline medium)

$$4OH^- \rightarrow O_2 + 2H_2O + 4e^- \quad \upsilon_{OER} = k_{OER}\,[OH^-_{OER}]^{x_1}$$

UOR (in alkaline medium)

$$6OH^- + CO(NH_2)_2 \rightarrow N_2 + CO_2 + 5H_2O + 6e^- \quad \upsilon_{UOR} = k_{UOR}\,[OH^-_{UOR}]^{x_2}\,[urea]^y$$

Where υ is the reaction rate, k is the rate constant, [OH$^-$] and [urea] represent the concentration of the corresponding reactants (in a particular reaction), x and y are the orders of reaction with respect to the concentration of OH$^-$ and urea, respectively.
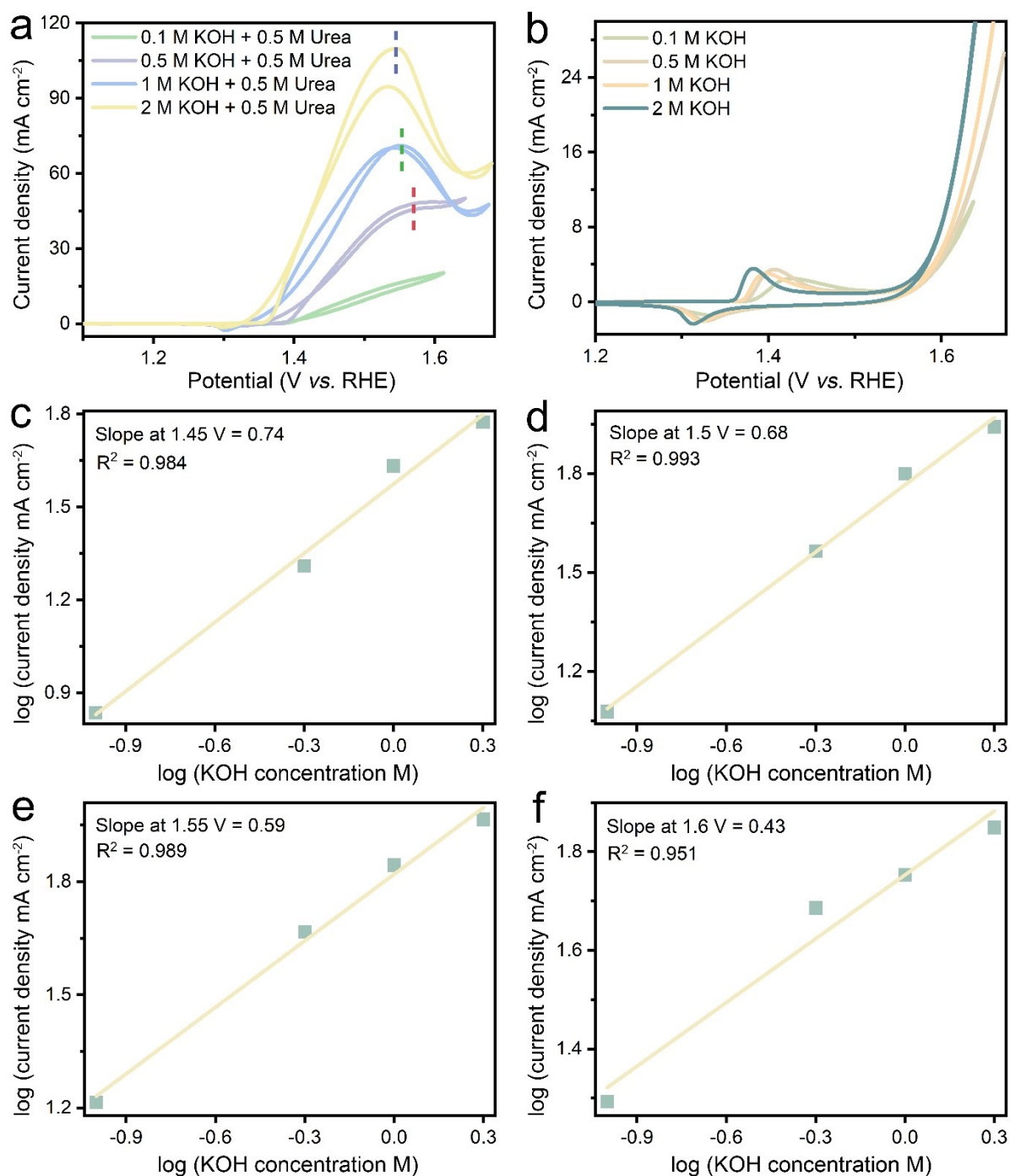
Supplementary Fig. 11 Study of the impact of KOH concentration on the alkaline urea electro-oxidation performance of NiWO₄-TA. a, b CV plots evaluated in various concentrations of KOH aqueous electrolytes (**a**) with and (**b**) without 0.5 M urea. **c-f** The dependence study of the oxidation current density on the KOH concentration at (**c**) 1.45 V, (**d**) 1.5 V, (**e**) 1.55 V, and (**f**) 1.6 V *vs.* RHE. The linear slope is equivalent to the reaction order of OH⁻.

As displayed in Supplementary Fig. 11a and b, higher KOH concentration leads to better performance of NiWO₄-TA in both electrolysis systems with and without urea. Nevertheless, higher pH value also results in fiercer UOR/OER competition as evidenced by the shift of the "anodic peaks" to a lower potential. In addition, as can be seen in Figure 11c-f, urea electrolysis LSVs exhibit a strong dependence on the concentration of OH⁻. Interestingly, the reaction order of OH⁻ declines with the increased potential (from 0.74 at 1.45 V *vs.* RHE down to 0.43 at 1.6

V *vs.* RHE). As UOR and OER have different reaction orders with respect to the concentration of OH^- due to their distinctive reaction mechanism (Supplementary Note 1), the decreased OH^- reaction order of the entire urea electrolysis system suggests an ever-changing UOR reaction kinetics which can be attributed to the influence from OER. It is noteworthy that although no sign of UOR/OER competition can be observed when the KOH concentration is adjusted to an ultra-low level (0.1 M), the corresponding electrolysis performance is also seriously affected due to the insufficiency of OH^-. Hence, the control of UOR/OER competition cannot be accomplished by simply adjusting OH^- concentration, which agrees with the as-reached conclusion in Supplementary note 1.
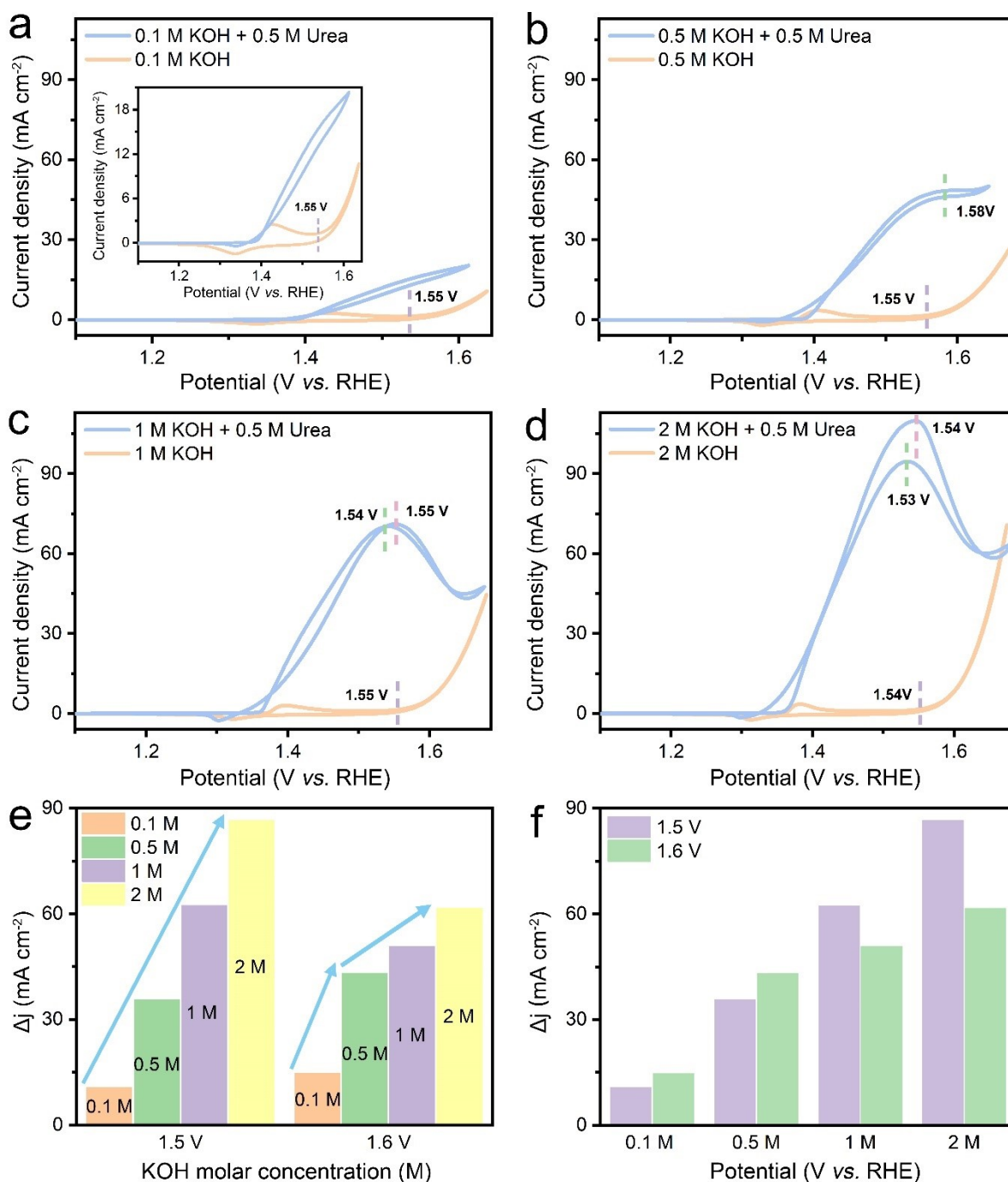
**Supplementary Fig. 12 a-d** CVs of NiWO$_4$-TA evaluated in (**a**) 0.1 M, (**b**) 0.5 M, (**c**) 1 M and (**d**) 2 M KOH with and without 0.5 M urea. **e, f** Current density difference between urea and water electrolysis systems at different pH and applied potentials (derived from the results in Supplementary Fig. 12a-d).

As displayed in Supplementary Fig. 12a-d, with the rise of KOH concentration, a growingly fierce UOR/OER competition can be identified by the negatively shifted competition peak and the ever-enlarging current density cut-off in the OER zone. To have a comprehensive understanding of the relationship between KOH concentration and UOR/OER competition, the as-described electrochemical results were reformatted based on the assumption of $j_{UOR} = \Delta j = j_{KOH + urea} - j_{KOH}$. As can be found in Supplementary Fig. 12e, both Δj at 1.5 and 1.6 V $vs.$ RHE (potentials locate in the UOR and competition zone, respectively) increase with the KOH concentration, suggesting the positively correlated KOH concentration-UOR activity

relationship. Nevertheless, the sluggish Δj increase at 1.6 V *vs.* RHE indicates UOR is heavily disturbed by OER in the high-potential region. Supplementary Fig. 12f reveals that the interference from OER increases with the rise of KOH concentration (when KOH concentration = 0.1 or 0.5 M, Δj at 1.5 V is less than that at 1.6 V; when KOH concentration = 1 or 2 M, Δj at 1.5 V surpasses that at 1.6 V).
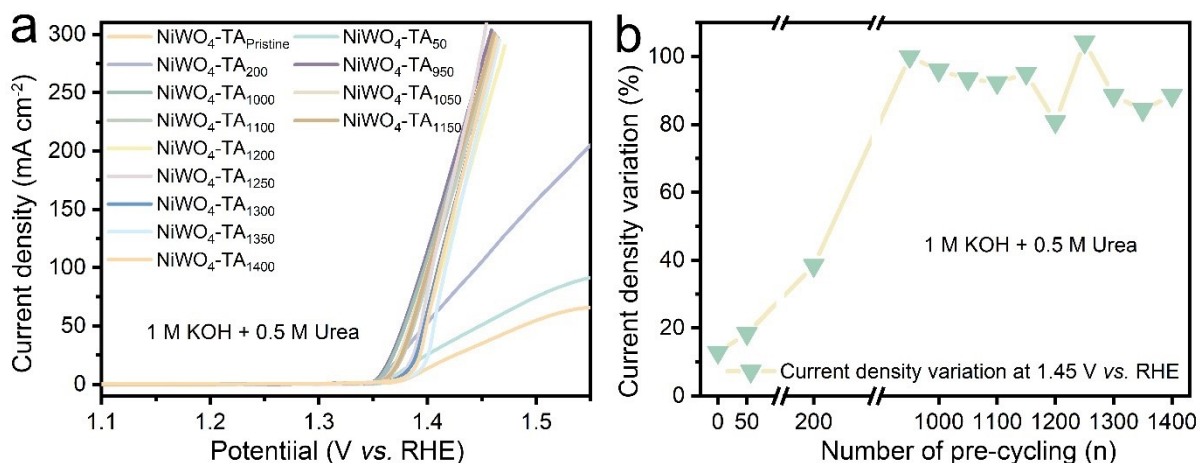
Supplementary Fig. 13 a LSVs of $NiWO_4$-TA_x (x = 0-1400) tested in 1 M KOH + 0.5 M urea. **b** The comparison of urea electrolysis current of $NiWO_4$-TA_x (x = 0-1400) at 1.45 V *vs.* RHE (derived from the data in Supplementary Fig. 13a).
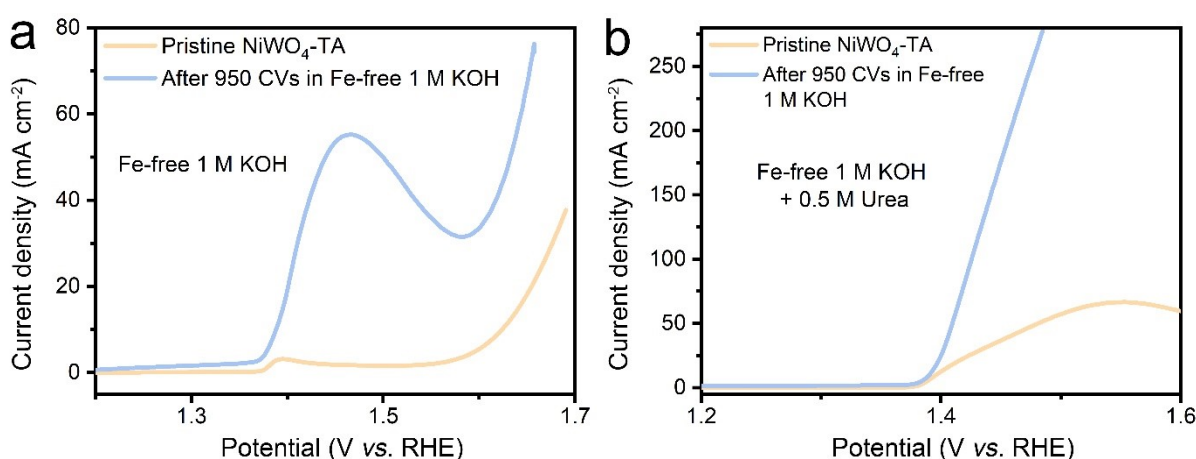
Supplementary Fig. 14 LSVs of pristine and cycled $NiWO_4$ scanned in Fe-free (**a**) 1 M KOH and (**b**) 1 M KOH + 0.5 M urea. Please note all the electrochemical tests relevant to Supplementary Fig. 14, including the CV cycling process, were performed in purified and Fe-free electrolyte.

To explore the influence of trace Fe ion in the electrolyte to the catalyst performance alteration , $NiWO_4$ was cycled and tested in Fe-free electrolyte (before any test, cells were cleaned by soaking in hydrochloric acid overnight and then rinsed with DI water, electrolyte was purified according to the method introduced by Wang *et al.*[3]). The electrochemical data acquired in the purified electrolyte (Supplementary Fig. 14) shows similar trend with that recorded in the impurified electrolyte (Fig. 2a and b in the manuscript). Though this does not mean Fe ion is totally irrelevant to the reconstruction of the catalyst (it is possible that the influence of Fe ion overlaps with the impact from the W leaching), we believe the impact of trace Fe ion in the electrolyte can be ignored in this study.
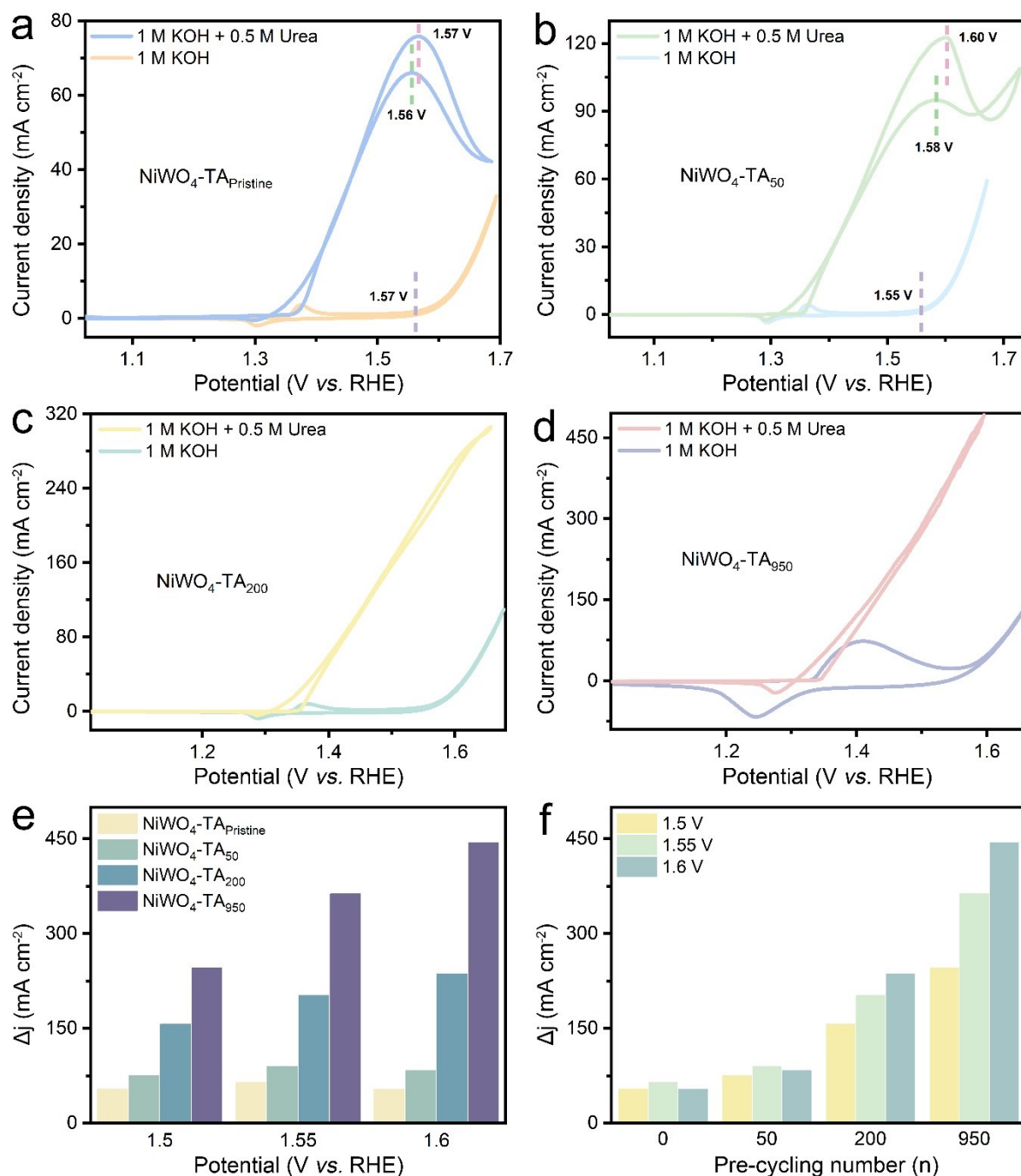
Supplementary Fig. 15 a-d CVs of (**a**) NiWO$_4$-TA$_{Pristine}$, (**b**) NiWO$_4$-TA$_{50}$, (**c**) NiWO$_4$-TA$_{200}$ and (**d**) NiWO$_4$-TA$_{950}$ evaluated in 1 M KOH with and without 0.5 M urea. **e, f** Current density difference between urea and water electrolysis systems governed by NiWO$_4$-TA with different electrochemical aging degrees or under different applied potentials (derived from Supplementary Fig. 15a-d).

As demonstrated in Supplementary Fig. 15a and b, the UOR/OER competition peaks of NiWO$_4$-TA$_{50}$ witnesses a 20-30 mV positive shift compare to those observed for NiWO$_4$-TA$_{Pristine}$, indicating a postponed UOR/OER competition. Interestingly, there is no sign of the competition peak in the CVs of NiWO$_4$-TA$_{200\ or\ 950}$ which suggests the competition between UOR and OER either vanishes or its 'damage' has been compensated by the escalated OER current. To analyse the correctness of the latter hypothesis, the as-discussed electrochemical data was reformatted (based on the assumption of $j_{UOR} = \Delta j = j_{KOH + urea} - j_{KOH}$) and the results

are presented in Supplementary Fig. 15e and f. The Δj trends in both low- and high-potential regions are $NiWO_4$-TA_{950} > $NiWO_4$-TA_{200} > $NiWO_4$-TA_{50} > $NiWO_4$-$TA_{Pristine}$, implying the activity growth (with the pre-activation degree of the catalysts) of the urea electrolysis system actually exceeds that of the water electrolysis system (Supplementary Fig. 15e). Thus, the rise of OER activity is unlikely the driving force for the 'elimination' of the competition peak. In addition, as shown in Supplementary Fig. 15f, the Δj value of $NiWO_4$-$TA_{Pristine\ or\ 50}$ peaks at 1.55 instead of 1.6 V *vs.* RHE which indicates the progress of UOR is disturbed in the OER region. Whereas, as for the $NiWO_4$-$TA_{200\ or\ 950}$, the oxidation current that believes to be related to UOR exhibits a positive correlation with the applied potential, revealing either UOR exhibits superior kinetics over OER or at least escapes from its influence when governed by the deeply-cycled samples.
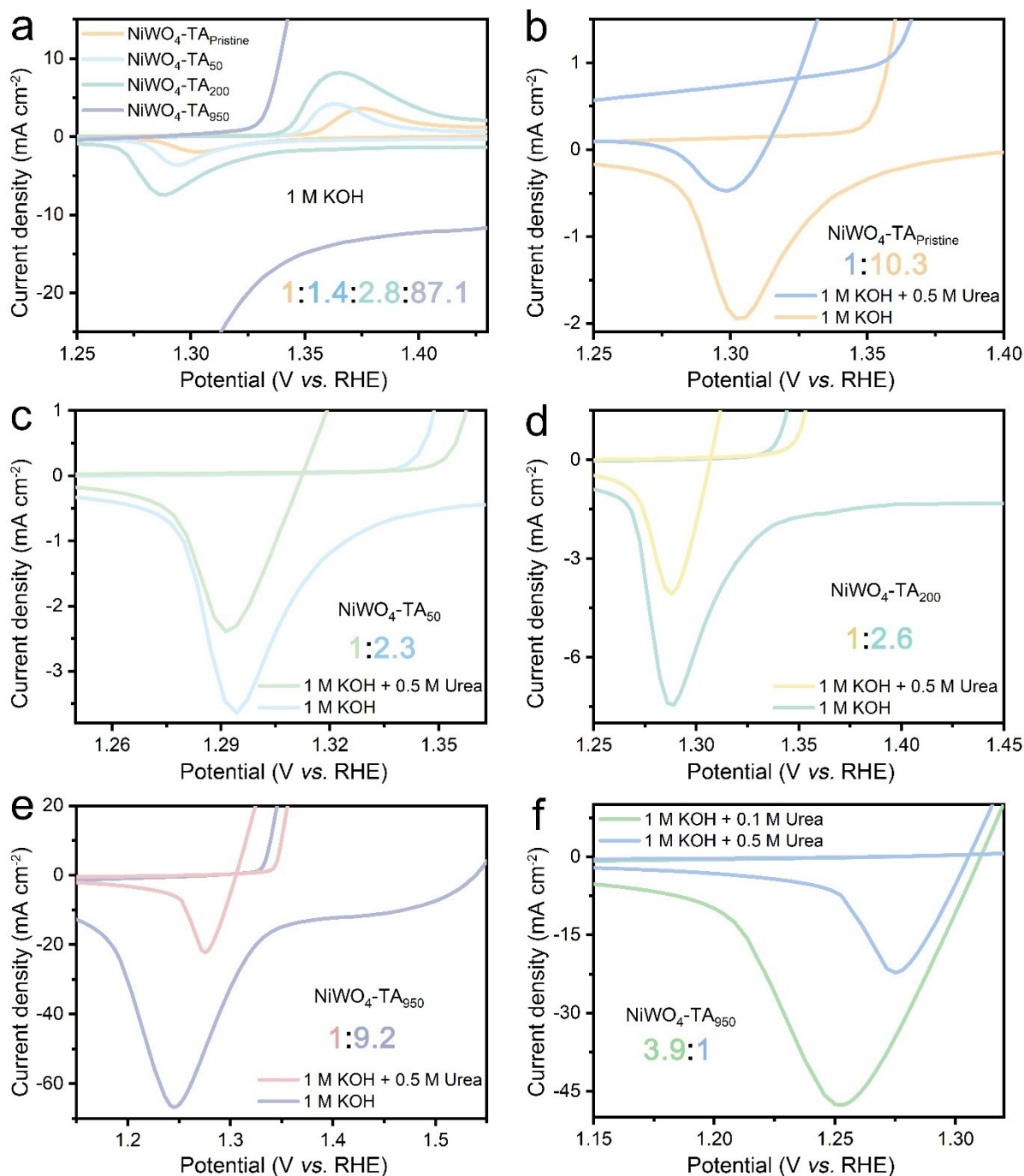
Supplementary Fig. 16 Comparisons of the Ni²⁺/Ni³⁺ redox features of NiWO₄-TA_x examined in water and urea electrolysis systems. a Pseudocapacitive behaviour transformation of NiWO₄-TA during CV cycling in 1 M KOH. **b-e** Comparisons of the Ni cathodic redox of (**b**) NiWO₄-TA_Pristine, (**c**) NiWO₄-TA₅₀, (**d**) NiWO₄-TA₂₀₀ and (**e**) NiWO₄-TA₉₅₀ during water (in 1 M KOH) and urea (in 1 M KOH + 0.5 M urea) electrolysis, respectively. **f** Reduction peaks of NiWO₄-TA₉₅₀ evaluated in 1 M KOH containing 0.1 or 0.5 M urea, respectively. The colourful number sequence in each paragraph represents the approximate areal ratio of the redox peaks.

As presented in Supplementary Fig. 16a, an increasingly active Ni redox (Ni²⁺/Ni³⁺) chemistry of NiWO₄-TA_x can be witnessed which is in accordance with their water and urea electrolysis activity trends, revealing the enrichment of dynamic Ni³⁺ is likely responsible for the catalytic activity enhancement. Interestingly, the Ni³⁺ to Ni²⁺ reduction peaks in the urea electrolysis

systems are consistently lower than that in the water electrolysis systems regardless of the pre-cycling degree of the catalysts (Supplementary Fig. 16b-e). In addition, higher urea concentration was found to result in smaller Ni cathodic redox peak (Supplementary Fig. 16f). The as-described findings confirm the consumption of Ni^{3+} during UOR and accordingly the indispensable role of Ni^{3+} upon promoting the decomposition of urea molecules. Such conclusion is in obedience to the insights provided by the previous research.[4-6]

Supplementary Note 2

To understand the UOR and OER reaction mechanism over Ni^{3+}, density-functional theory (DFT) calculations were carried out to evaluate the adsorption chemistry of several key intermediates during the reaction process. It is worth to mention that despite NiOOH (001) surface may not be the model that fits the Ni coordination chemistry in our pristine/aged $NiWO_4$ catalyst perfectly, it is chosen as the host for Ni^{3+} active sites in this simulation due to its well-recognised intrinsic and catalytic properties.[7-9] The surface of NiOOH (001) was saturated with OH ligands, which ensures the calculation model is close to operating conditions. The optimized structures of *OH, *O and *OOH on NiOOH are provided in the upper panel of Fig. 2d (main text). Moreover, the adsorption structure of urea on NiOOH is presented in the lower region of Fig. 2d. There is one bond generated between N and Ni with a bond length of 2.27 Å. The bond length between H from urea and lattice O from NiOOH is 1.94 Å, indicating the presence of hydrogen bond interaction between urea molecules and the catalytic surface. The adsorption free energy of urea on NiOOH (001) is calculated as -0.49 eV.

In addition, we evaluated the free energy diagram of OER process on NiOOH (001) as Fig. 2d (main text) shows, from which it can be observed that the adsorption strength of *OH is the key to determine the overall reaction barrier. In other words, the progress of OER is hindered by the high adsorption strength of OH ligand on the (001) surface. Hence, the elementary step (*OH → *O) is the rate-determining step. At the potential of 0 V *vs.* normal hydrogen electrode (NHE), the overall reaction free energy is 1.62 eV. At the equilibrium potential (0.404 V *vs.* NHE), it can be observed that the energy state of *OH is under 0 eV, while those of *OH and *OOH are above 0 eV, resulting in an insurmountable energy barrier for the deprotonation of *OH. On the other side, when the applied voltage reaches 0.87 V *vs.* NHE (overpotential of 0.47 V), there is no energy barrier anymore and the OER can start to perform. In a word, OER on NiOOH (001) is a relative sluggish process in terms of reaction kinetics.
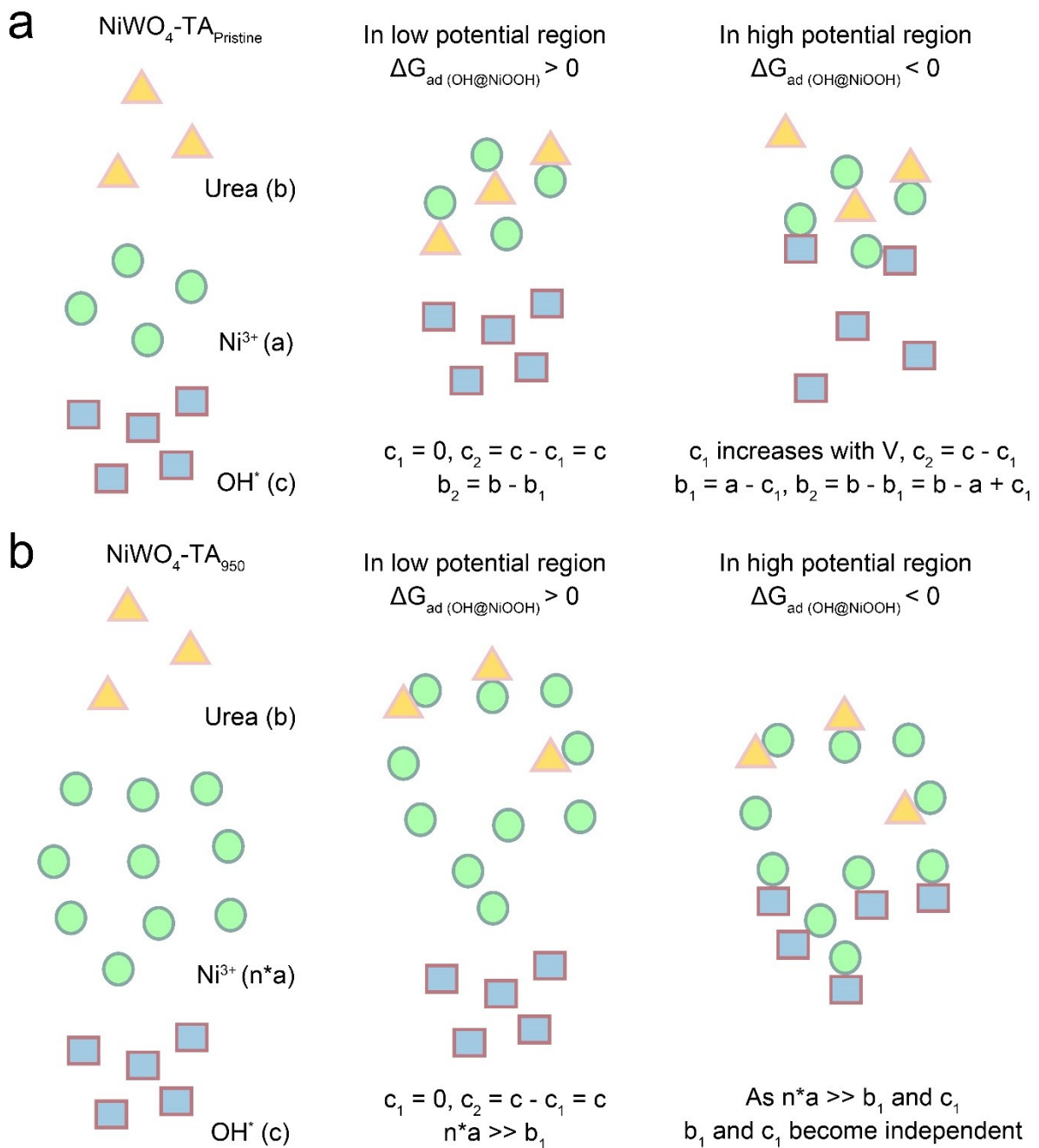
Supplementary Fig. 17 Schematic illustration of the effect of Ni³⁺ quantity on the adsorption behaviour of OH*, urea and Ni³⁺. Proposed scenarios based on **a** deficient and **b** sufficient Ni³⁺ active sites in the systems. a, b and c represent the quantity of Ni³⁺, urea and OH*, respectively. b_1 and c_1 represent the quantity of urea and OH* that bound with Ni³⁺. b_2 and c_2 represent the quantity of urea and OH* that cannot be absorbed by Ni³⁺.

To better clarify the as-proposed 'competing for Ni³⁺' hypothesis, two scenarios of the adsorption chemistry based on limited and excess number of available Ni³⁺ sites during the urea electrolysis have been constructed and shown in Supplementary Fig. 17. In the Ni³⁺-deficient scenario (Supplementary Fig. 17a), as $\Delta G_{ad(OH*@NiOOH)} > 0$, influences from OH* is negligible to the urea-Ni³⁺ adsorption chemistry in the low potential region. However, as the applied potential increases, OH* starts to be adsorbed by Ni³⁺, leading to the rise of c_1 and accordingly the drop of b_1. As a result, a UOR current cut-off will be witnessed. It can be imagined that with the further increase in the applied voltage, it is possible that no Ni³⁺ will be

accessible for urea eventually. On the contrary, as illustrated in Supplementary Fig. 17b, b_1 and c_1 will stay independent when sufficient Ni^{3+} sites are available.
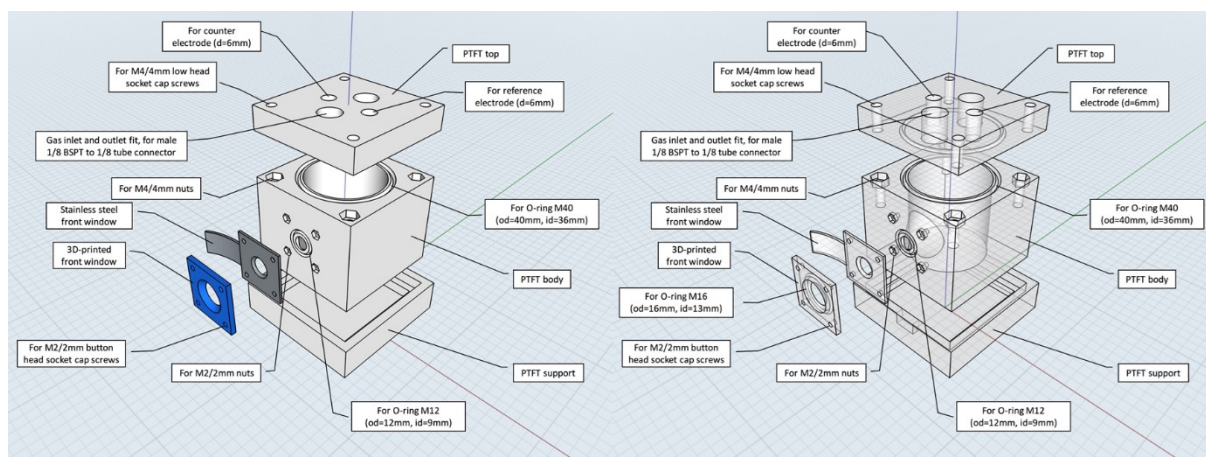
Supplementary Fig. 18 Design of the electrochemical cell for *operando* XANES measurement.[10]

Supplementary Fig. 18 shows the *operando* electrochemical cell operating in fluorescence mode. The cell was equipped with a three-electrode system. The catalyst was loaded on the carbon cloth as the working electrode and sealed at hole on the wall by a Kapton foil. The cell was filled with electrolyte solution (1 M KOH or 1 M KOH with 0.5 M urea), and the graphite rod counter electrode and saturated Ag/AgCl reference electrode were soaked in. The cell was placed 45 degrees to incident X-ray beam direction. The 36-element solid state Ge detector was positioned from vertical direction to measure the X-ray fluorescence.
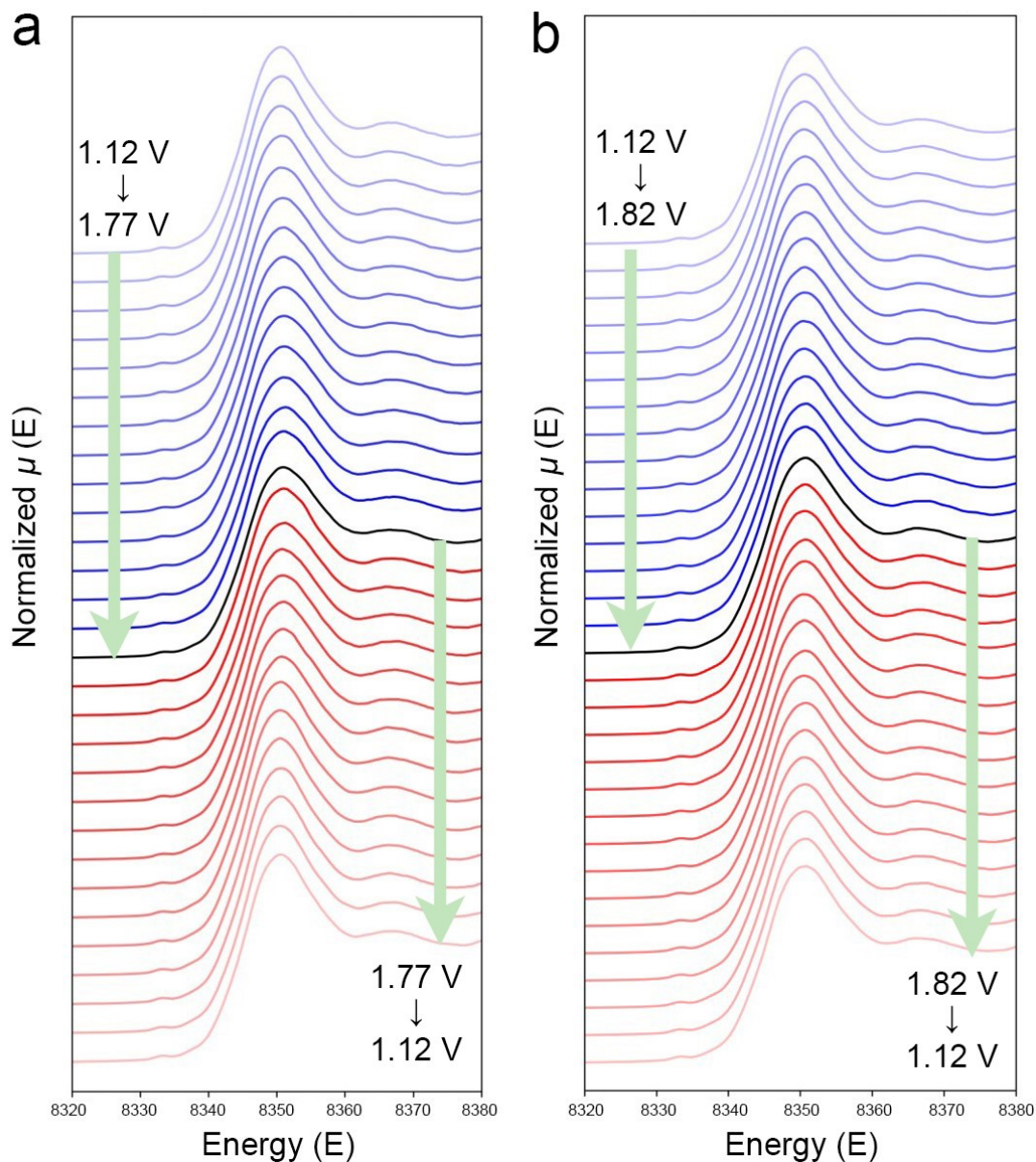
Supplementary Fig. 19 *Operando* Ni K-edge XANES spectra of $NiWO_4$-TA_{950} during CV of **a** water and **b** urea electrolysis. The anodic and cathodic scans are showed in red and blue curves respectively. The black curve corresponds to the highest potential applied to the catalysts. During water electrolysis, the edge position at 1.82 V *vs.* RHE shifted approximately 0.5 eV to higher energies compared with that at 1.12 V *vs.* RHE, accompanied with the decrease of white line intensity by nearly 8%. Here, with the activated sample, much larger amount of Ni^{3+} could be produced than that of $NiWO_4$-$TA_{pristine}$ under OER conditions. On the contrary, XANES difference during the urea electrolysis is negligible, indicating that with presence of urea, the accumulation of unoccupied Ni^{3+} is prohibited since a new redox process between Ni^{3+} and urea is introduced. It is important to point out that even the occupied Ni^{3+} was not observed (in Fig. 3b in the manuscript) which can possibly be ascribed to the following two reasons. First, most of the Ni^{3+} signal observed in the *operando* water electrolysis test (Fig. 3a in the manuscript) can be attributed to unoccupied Ni^{3+} which agrees with the DFT results that the reconstructed catalyst shows weakened OH^* adsorption ability (Supplementary Fig. 44). Second, the *operando* urea electrolysis test (Fig. 3b in the manuscript) did not scan into a potential window which is high enough to trigger the mass adsorption of OH^* by the dynamic

Ni^{3+} active site of the reconstructed sample (please be aware the potentials in the *operando* test results are not *iR* corrected; considering urea electrolysis exhibits much higher current than water electrolysis, the CV scan range during *operando* urea electrolysis test would be smaller than that of *operando* water electrolysis test if *iR* corrected; no *iR* correction has been made in the *operando* experiments in this work including the RTMS test, this is because it is impossible to correlate *iR*-corrected potential with current and MS/XAFS signal at the same time in a CV/LSV test). In other words, within the CV range shown in Fig. 3b (in the manuscript), the dynamic Ni^{3+} tends to adsorb urea molecules rather than OH*. Unlike OER which is thermodynamically sluggish (Fig. 2d and Supplementary Fig. 44), decompose of urea on Ni^{3+} site is more thermodynamically favourable (Supplementary Fig. 45). Consequently, no Ni^{3+} accumulation was observed in Fig. 3b. It is believed the accumulation of Ni^{3+} could be observed at higher potentials, at which OH* shows more favourable adsorption chemistry than urea molecule on Ni^{3+} site. This test did not scanned into a higher potential region due to the following reasons. First, noticeable amount of bubbles were formed during the urea electrolysis test. Although the XANES signal was not affected, the EXAFS signal was heavily disturbed. Considering the beamtime allocation and the poor EXAFS noise-to-signal ratio at high potentials, we limited the CV scan range. Additional experiments are demanded to observe the Ni chemistry during urea electrolysis at the high potential region.
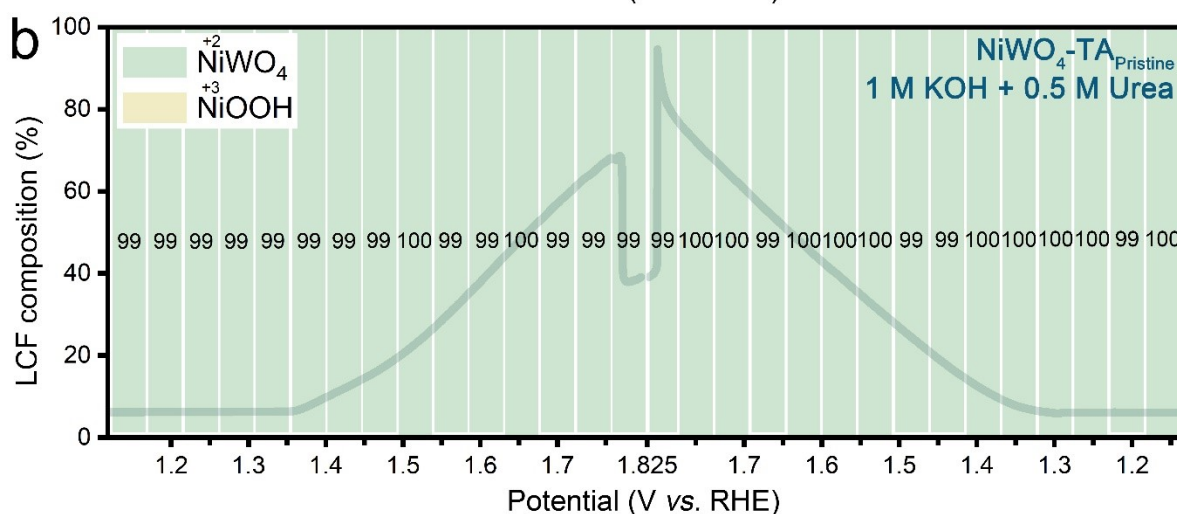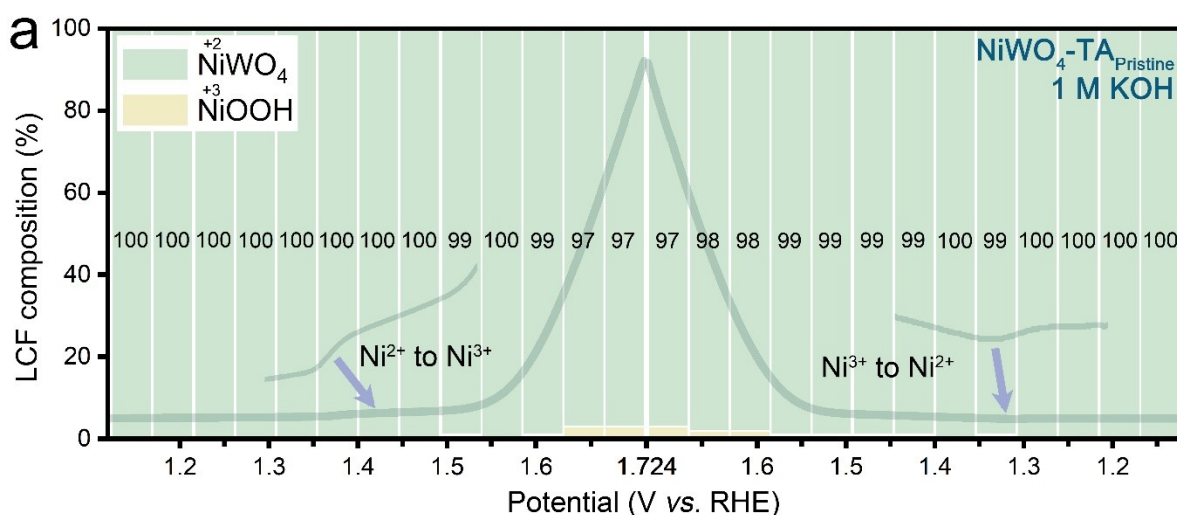
Supplementary Fig. 20 *Operando* **monitoring of the Ni chemical states of NiWO$_4$-TA$_{Pristine}$ during water and urea electrolysis**. LCF (linear combination fitting) results of Ni K-edge XANES spectra of NiWO$_4$-TA$_{950}$ under *operando* conditions in **a** 1 M KOH and **b** 1 M KOH + 0.5 M urea. The dark lines in the background are the corresponding LSVs without *iR* correction. Please note the response from XANES has a ~0.1 V delay compared to the electrochemical signal.

As shown in Supplementary Fig. 20a, for the pristine bimetal oxide catalyst, only trace amount of Ni^{3+} can be found during water electrolysis (above ~1.6 V *vs.* RHE), indicating the quantity of dynamic Ni^{3+} is at a low-level. Subsequently, a fewer number of the unoccupied Ni^{3+} are expected. As a result, the current collapse can be witnessed during urea electrolysis (Supplementary Fig. 20b). In addition, considering the low production rate of dynamic Ni^{3+} but the high consumption demand from UOR and OER, the whole catalyst kept at nearly 100% 2+ valence state during the *operando* urea electrolysis scan, even at 1.8 V *vs.* RHE.
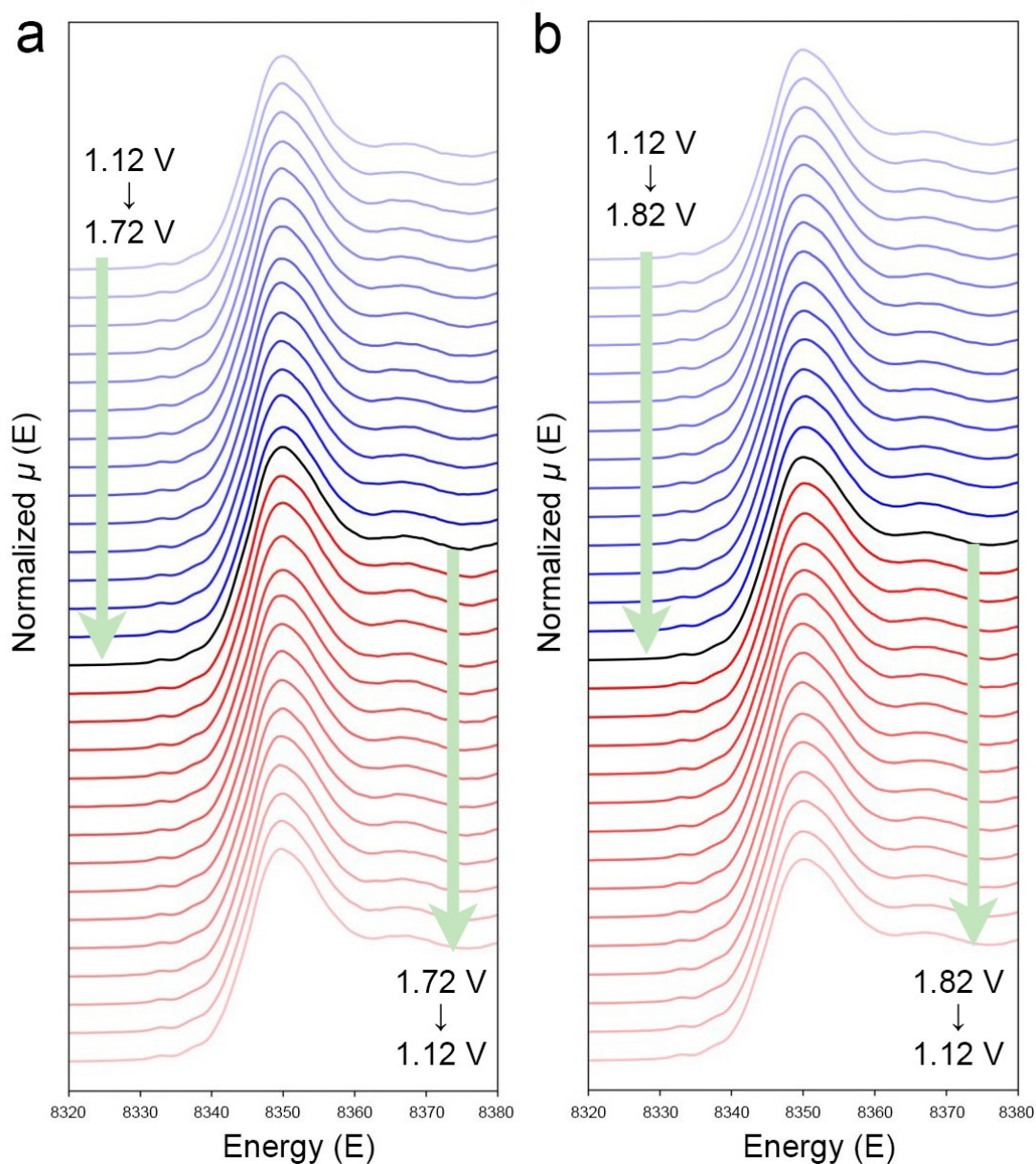
Supplementary Fig. 21 *Operando* Ni K-edge XANES spectra of NiWO$_4$-TA$_{pristine}$ during CV of **a** water and **b** urea electrolysis. The anodic scans and cathodic scans are showed in red and blue curves respectively. The black curve corresponds to the highest potential applied to the catalysts. No significant changes could be found in the Ni K-edge XANES spectra, in which edge position, white line intensity and other XANES features are almost identical at different potentials. This result confirms that Ni^{2+} is the dominant valence states in NiWO$_4$-TA$_{pristine}$ during both water and urea electrolysis.
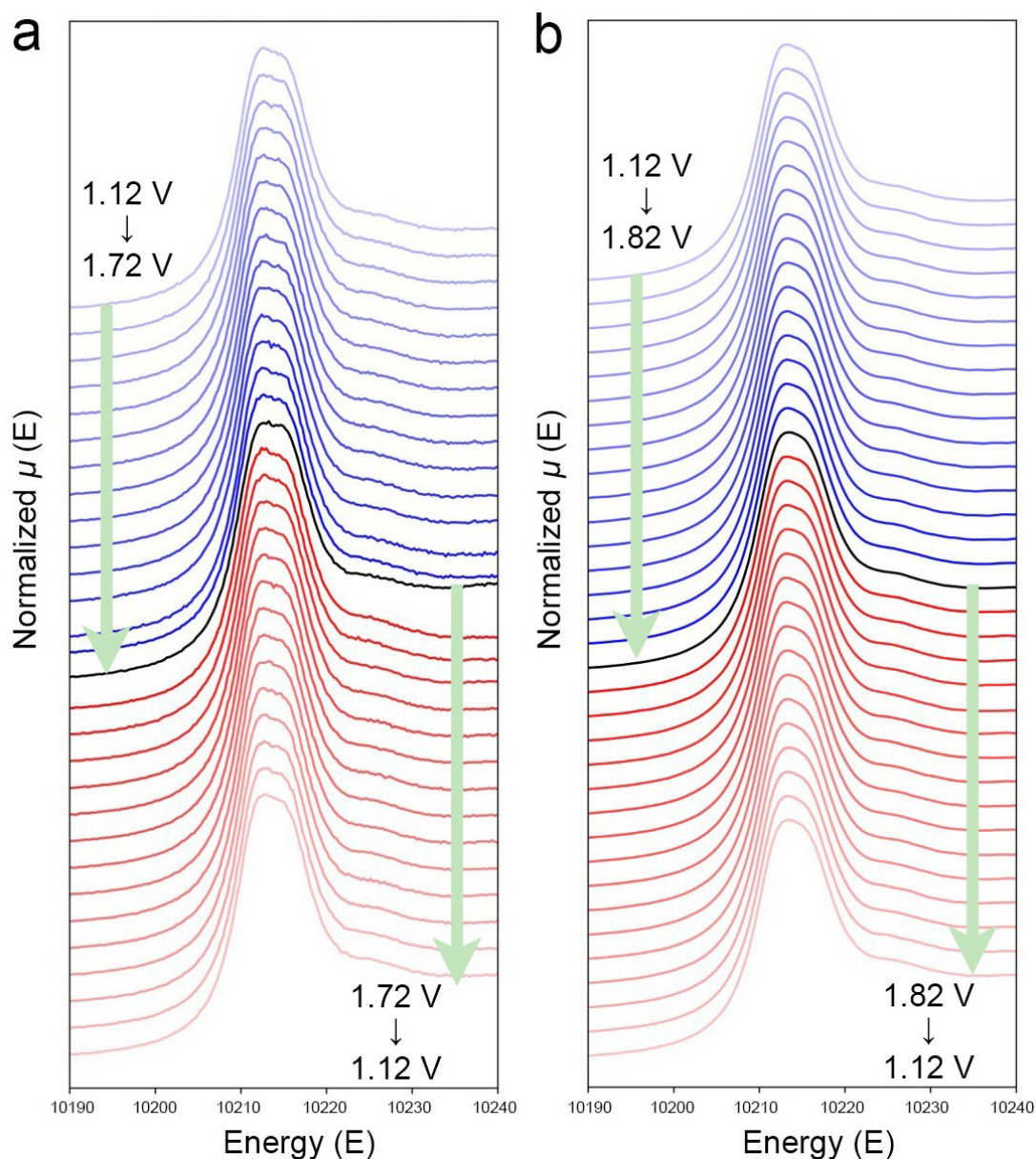
Supplementary Fig. 22 *Operando* W L$_3$-edge XANES spectra of NiWO$_4$-TA$_{pristine}$ during the CV of **a** water and **b** urea electrolysis. The anodic and cathodic scans are showed in red and blue curves respectively. The black curve corresponds to the highest potential applied to the catalysts. No significant change could be found in the W L$_3$-edge XANES spectra, in which edge position, white line intensity and other XANES features are almost identical at different potentials as well. Since we believe that the W^{6+} is not directly participate in the electron transition during OER and UOR conditions, this result is fully consistent with our hypothesis.
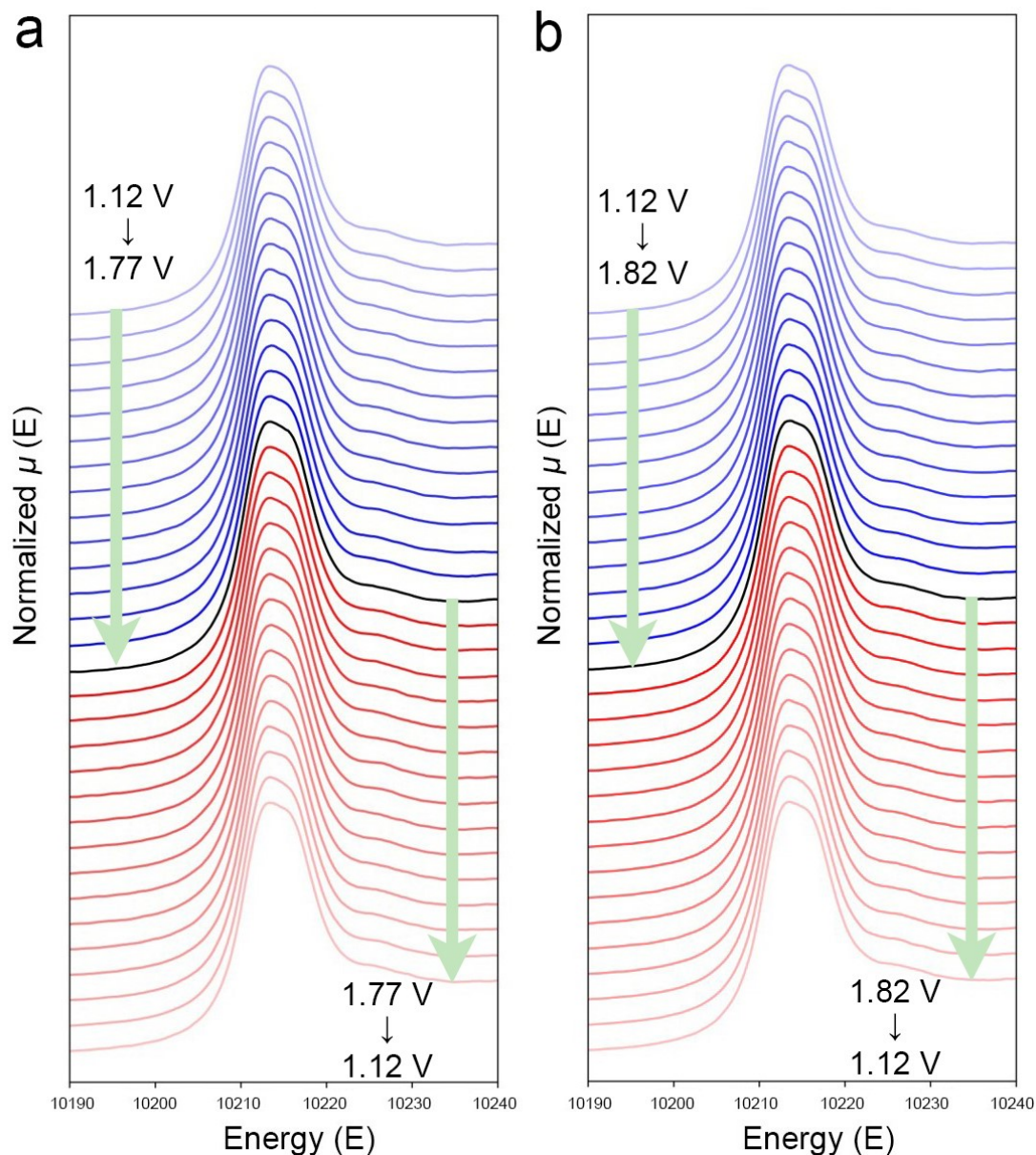
Supplementary Fig. 23 *Operando* W L$_3$-edge XANES spectra of NiWO$_4$-TA$_{950}$ during CV of **a** water and **b** urea electrolysis. The anodic and cathodic scans are showed in red and blue curves respectively. The black curve corresponds to the highest potential applied to the catalysts. No significant change could be found in the W L$_3$-edge XANES spectra, in which edge position, white line intensity and other XANES features are almost identical at different potentials as well. Therefore, even for the pre-activated NiWO$_4$-TA$_{950}$, W species acted as structural components rather than participated in the OER or UOR by W^{6+}/W^{4+}redox process.
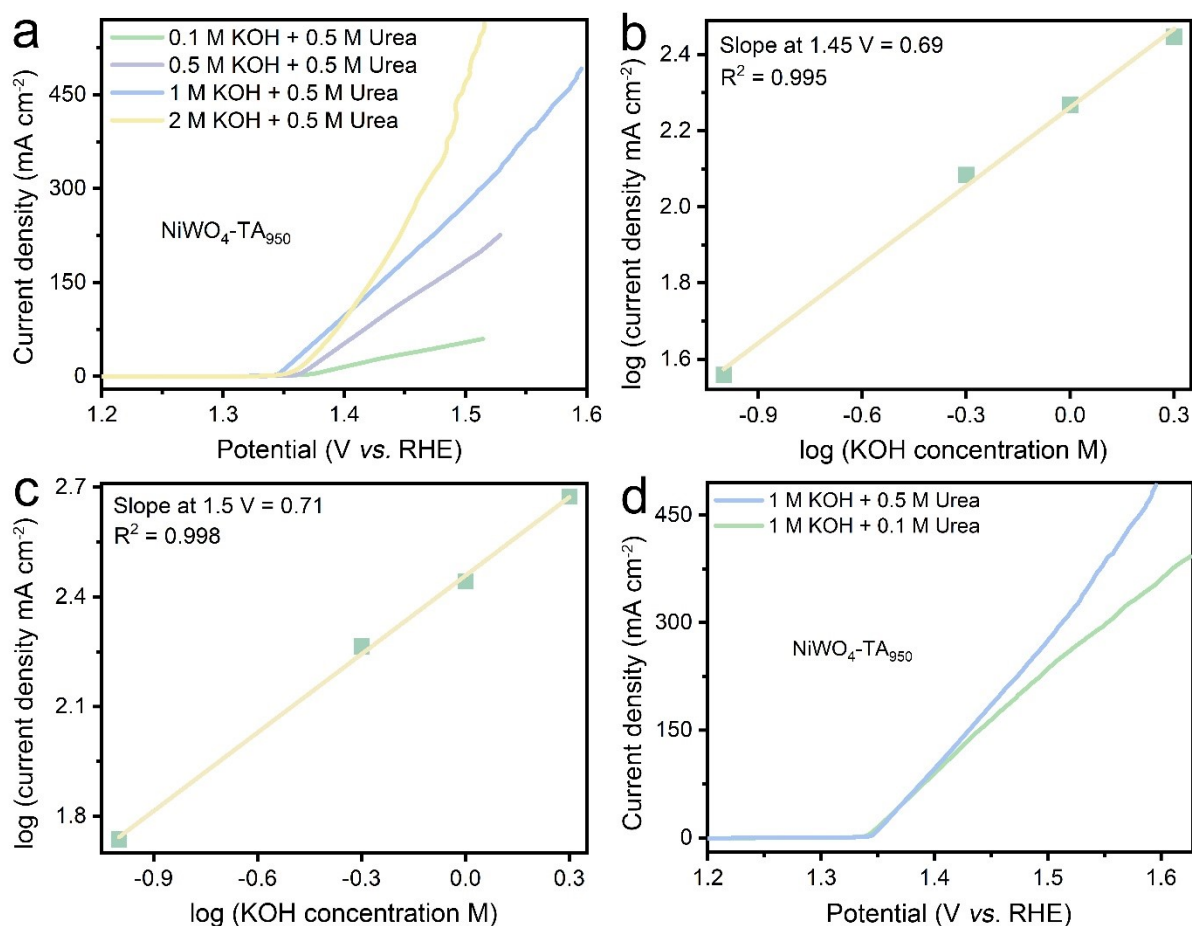
Supplementary Fig. 24 Study of the impact of KOH and urea concentration on the alkaline urea electro-oxidation performance of NiWO$_4$-TA$_{950}$. a LSVs obtained in various concentrations of KOH aqueous electrolytes containing 0.5 M urea. **b, c** The dependence study of the oxidation current density on the KOH concentration at (**b**) 1.45 V and (**c**) 1.5 V *vs.* RHE. **d** LSVs evaluated in 1 M KOH containing 0.1 or 0.5 M urea.

As it presents in Supplementary Fig. 24a, no sign of UOR/OER competition peak can be observed in the urea electrolysis polarization curves that governed by NiWO$_4$-TA$_{950}$ regardless of the KOH concentration. As a result, according to Supplementary Fig. 24b and c, the reaction order of OH$^-$ remains constant at different applied potentials (0.69 and 0.71 at 1.45 and 1.5 V *vs.* RHE, respectively) which indicates UOR is independent of OER when a consistent and sufficient Ni^{3+} supply chain is guaranteed. In addition, Supplementary Fig. 24d shows the LSVs measured in 1 M KOH containing 0.1 or 0.5 M urea, respectively, from which a positive urea concentration-current density relationship can be identified. It is noteworthy that the increase in urea concentration only leads to limited oxidation current density improvement which suggests the formation of dynamic Ni^{3+} is likely the rate-determining step/factor for UOR rather than the mass transfer of urea molecules.
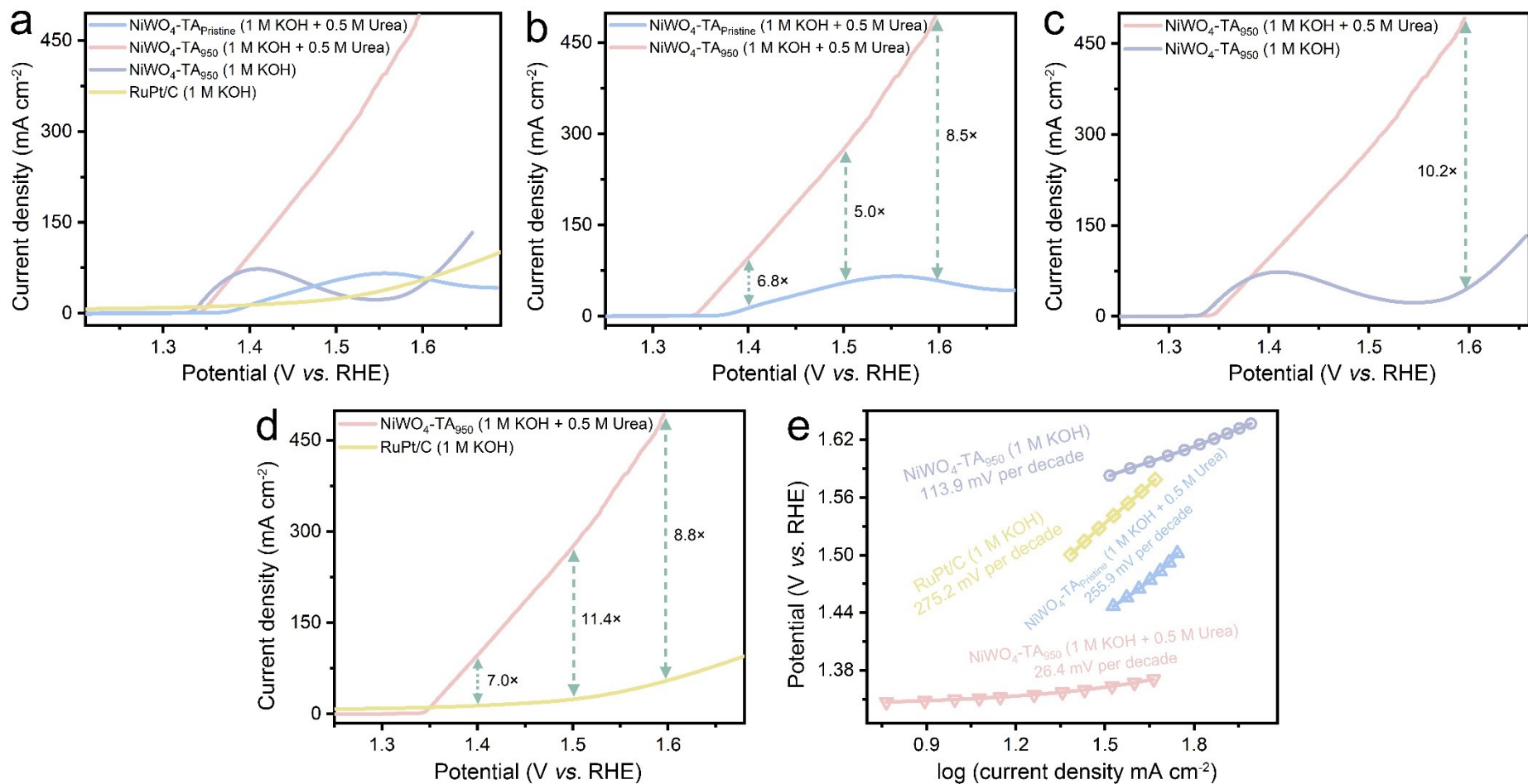
Supplementary Fig. 25 a Polarization curves for the urea and water electrolysis tests of various catalysts. **b-d** Comparisons of the (**b**) urea electrolysis performance of NiWO$_4$-TA$_{Pristine}$ and NiWO$_4$-TA$_{950}$, (**c**) urea and water electrolysis performance of NiWO$_4$-TA$_{950}$ and (**d**) NiWO$_4$-TA$_{950}$-governed urea electrolysis polarization curve and commercial RuPt/C-induced OER LSV. **e** Tafel plots derived from Supplementary Fig. 25a.

As can be learned from Supplementary Fig. 25a, $NiWO_4$-TA_{950} exhibits an outstanding urea electrolysis performance which is evidenced by its low onset (1.34 V *vs.* RHE when current density reaches 10 mA cm^{-2}) and high oxidation current density (larger than 300 and 500 mA cm^{-2} at 1.5 and 1.6 V *vs.* RHE, respectively). More specifically, the urea electrolysis current densities of $NiWO_4$-TA_{950} at 1.4, 1.5 and 1.6 V *vs.* RHE are 7.0, 11.4 and 8.8 times higher than that of $NiWO_4$-$TA_{Pristine}$ which again underscores the importance of dynamic Ni^{3+} for the oxidation of urea (Supplementary Fig. 25b). Moreover, the superiority of UOR over OER as an anodic half reaction is confirmed by its 6.8, 5.0 and 8.5 times higher current densities at 1.4, 1.5 and 1.6 V *vs.* RHE, respectively (Supplementary Fig. 25c). In addition, the activity of $NiWO_4$-TA_{950} was also compared to that of commercial RuPt/C catalyst whose result is shown in Supplementary Fig. 25d. The 7.0, 11.4 and 8.8 times higher current densities of $NiWO_4$-TA_{950}-governed urea electrolysis over that of RuPt/C-induced water electrolysis at 1.4, 1.5 and 1.6 V *vs.* RHE, respectively provide solid evidence for the supremacy of UOR compared to traditional noble metal-prompted OER. Furthermore, our experiments revealed that $NiWO_4$-TA_{950} possesses an ultra-small Tafel slope of 26.4 mV dec^{-1} for the urea electrolysis process, pointing to its favourable catalytic kinetics.
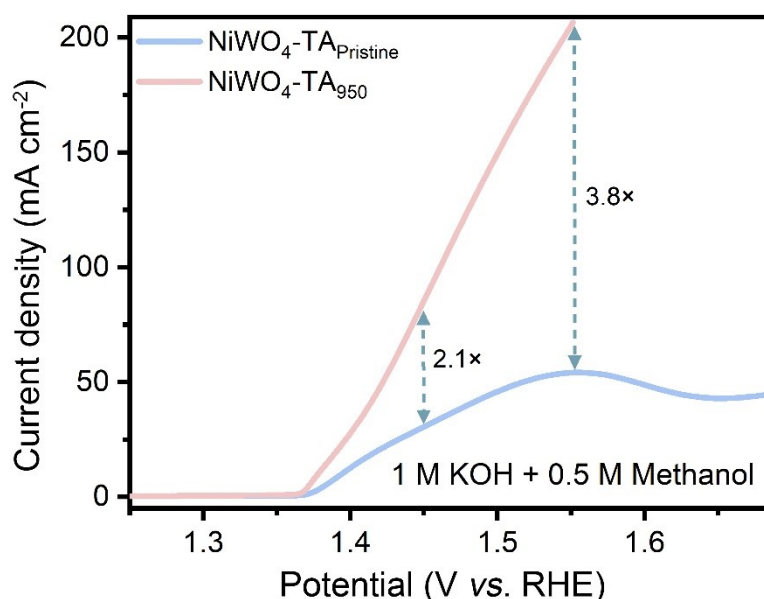
Supplementary Fig. 26 LSVs of $NiWO_4$-$TA_{Pristine}$ and $NiWO_4$-TA_{950} acquired in 1 M KOH containing 0.5 M methanol. Unlike the LSV of $NiWO_4$-$TA_{pristine}$, no sudden current drop can be witnessed throughout the methanol electrolysis test when governed by the activated bimetal oxide catalyst. Therefore, considering the conclusion we reached from the UOR/OER, it is believed the MOR/OER competition is also provoked by the insufficiency of Ni^{3+} active sites. When the dynamic Ni^{3+} is abundant, the MOR/OER performance saturation can be avoided.
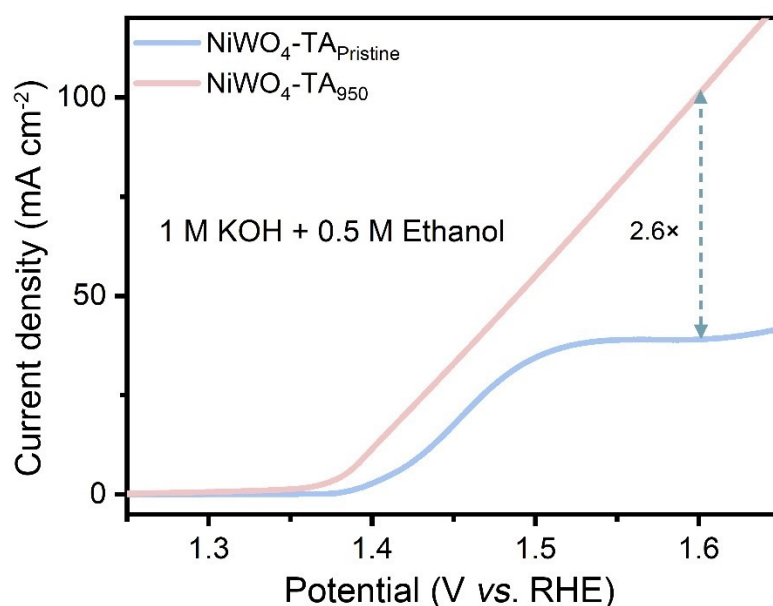
Supplementary Fig. 27 LSVs of $NiWO_4$-$TA_{Pristine}$ and $NiWO_4$-TA_{950} acquired in 1 M KOH containing 0.5 M ethanol. EOR results agree with the as-reached conclusion that when the dynamic Ni^{3+} is abundant, the OCOR/OER performance saturation can be avoided.
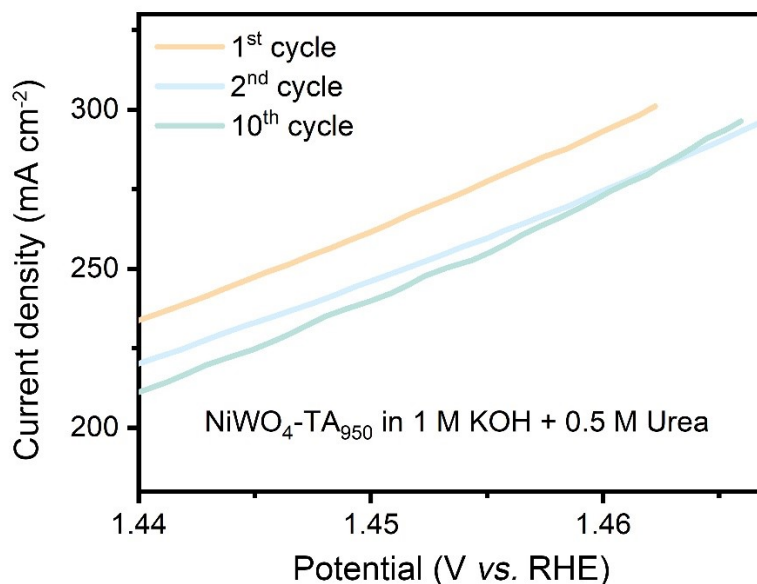
Supplementary Fig. 28 The 1st, 2nd and 10th LSVs of $NiWO_4$-TA_{950} recorded in 1 M KOH + 0.5 M urea. As can be found in Supplementary Fig. 28, the urea electrolysis current of $NiWO_4$-TA_{950} witnesses a minor but still visible decrease after the first scan. The LSV remains stable afterwards. It is believed the current density decrease in the second scan compared to that in the first scan can be ascribed to the irreversible consumption of intrinsic surface NiOOH active sites. This indicates the reconstructed surface oxyhydroxide species are not recyclable, hence are not regarded as major contributors of the boosted catalytic activity of $NiWO_4$-TA_{950}.
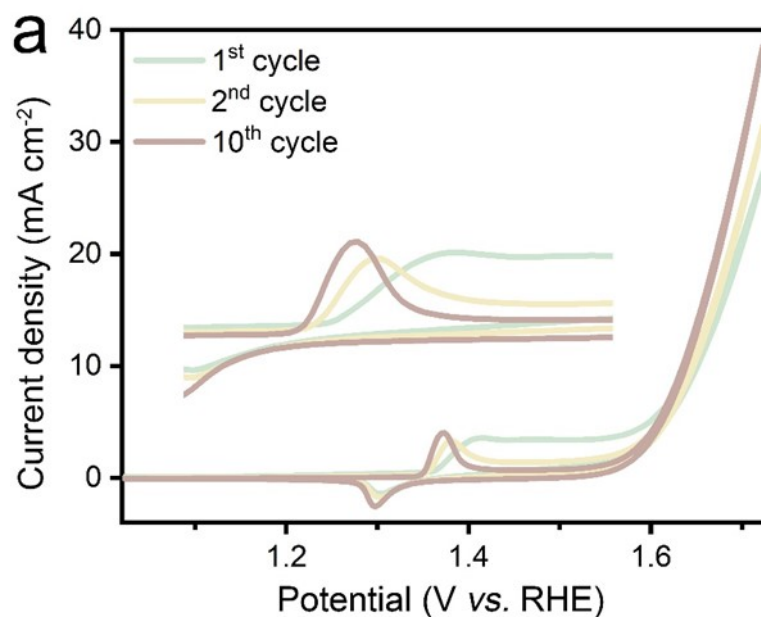
Supplementary Fig. 29 Ni^{2+}/Ni^{3+} redox chemistry evolution of $NiWO_4$-$TA_{Pristine}$ in the first 10 CV cycles in 1 M KOH.

As presented in Supplementary Fig. 29, the transformation of the oxide or hydroxide phase to oxyhydroxide can be identified by the decreased Ni^{2+} to Ni^{3+} oxidation peak in the 2nd CV compared to that in the 1st cycle. Interestingly, when further cycling the bimetal catalyst, a stronger other than weaker Ni^{2+} to Ni^{3+} peak can be witnessed, indicating the oxyhydroxidization process terminates within the first few cycles. Nevertheless, to observe obvious catalytic performance change of $NiWO_4$-TA, dozens or even hundreds of CVs have to be performed which indicates surface oxyhydroxidization is not the major promoter of the boosted Ni redox chemistry.
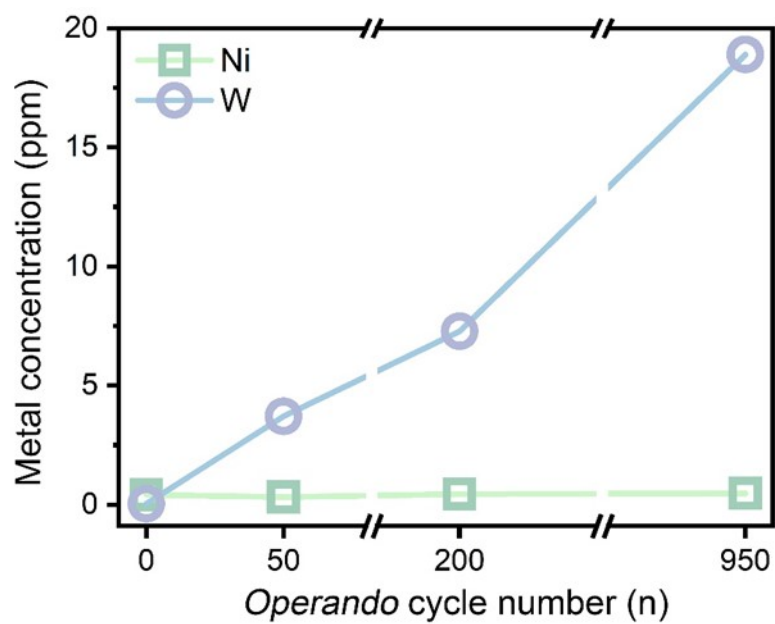
Supplementary Fig. 30 Inductively coupled plasma atomic emission spectroscopy (ICP-AES) test of the electrolyte for NiWO$_4$-TA cycling between 0-0.7 V *vs.* Ag/AgCl in 1 M KOH for 950 CV cycles.
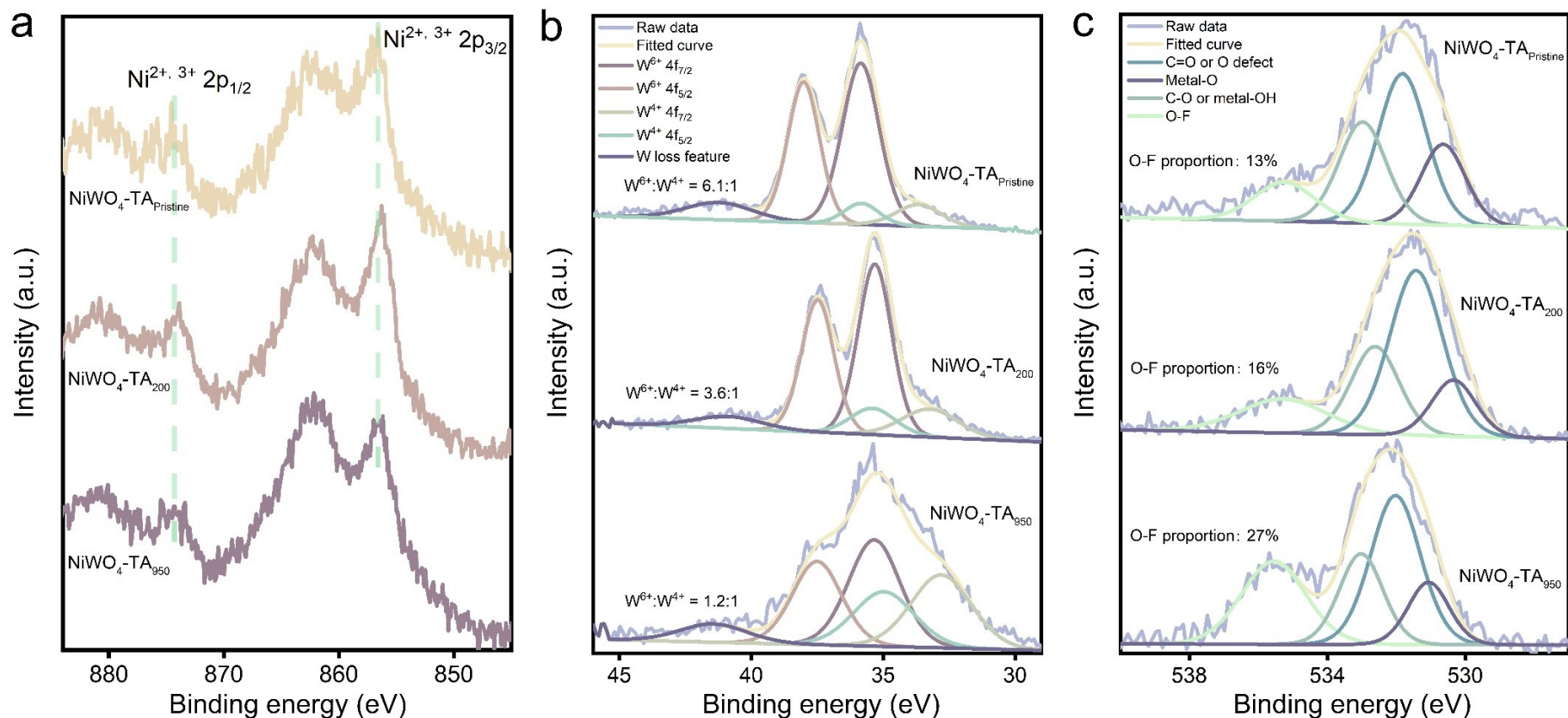
Supplementary Fig. 31 XPS spectra of **a** Ni 2p, **b** W 4f, and **c** O 1s peaks for NiWO$_4$-TA$_x$ (x = 0, 200 and 950).

Ex-$situ$ XPS was performed to investigate the surface chemistry of NiWO$_4$-TA before and after cycling in alkaline medium. As it shows in Supplementary Fig. 31a, no obvious change can be found in the XPS Ni 2p spectra despite the formation of the surface oxyhydroxide layer during the first few CVs. It is suspected that the signal of the high valence Ni is too weak to be observed due to its low population. Moreover, the highly overlapped binding energy of Ni^{2+} and Ni^{3+} makes them difficult to be distinguished. As for the W 4f spectra (Supplementary Fig. 31b), a decrease in the ratio of W^{6+}/(W^{6+} + W^{4+}) can be witnessed after the electrochemical treatment which can be explained by the leaching of W^{6+} during CV cycling. Additionally, as presented in Supplementary Fig. 31c, O loss can be identified by the increased O-F bond composition (F-containing Nafion was used as the binder for electrode preparation, its composition over the entire O 1s spectrum can be used as a reference for the detection

of O signal intensity variation). Therefore, based on our XPS observation, it is highly likely that W was leached from the catalyst into the electrolyte in the form of WO_4^{2-} .
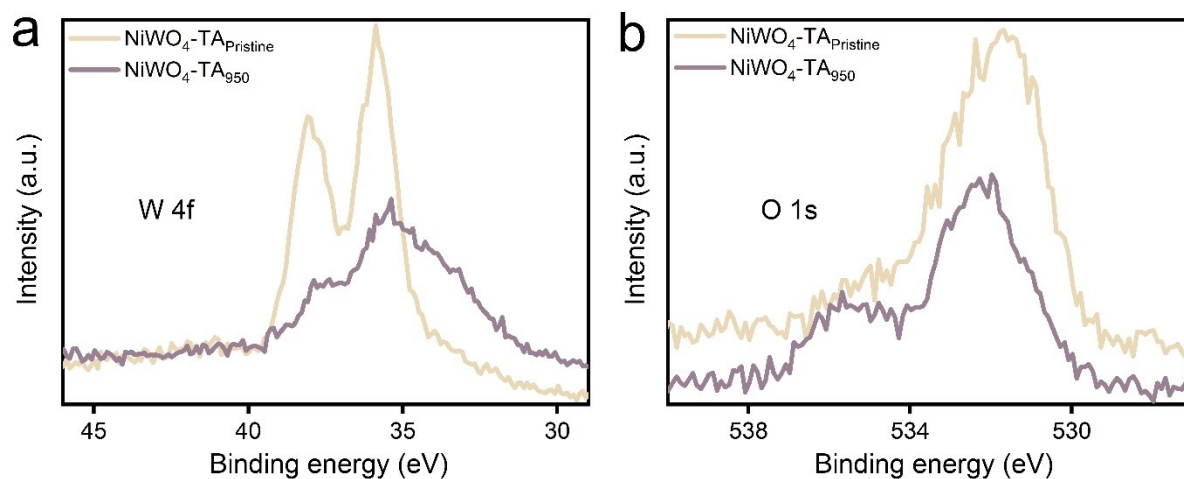
Supplementary Fig. 32 Comparison of the XPS **a** W 4f and **b** O 1s spectra of NiWO$_4$-TA$_{Pristine}$ and NiWO$_4$-TA$_{950}$. Although XPS is not widely used for quantifying chemical composition, the obvious intensity difference between the W 4f and O 1s spectra of pristine and aged samples provides further evidence for the leaching of W and O during the electrochemical treatment.
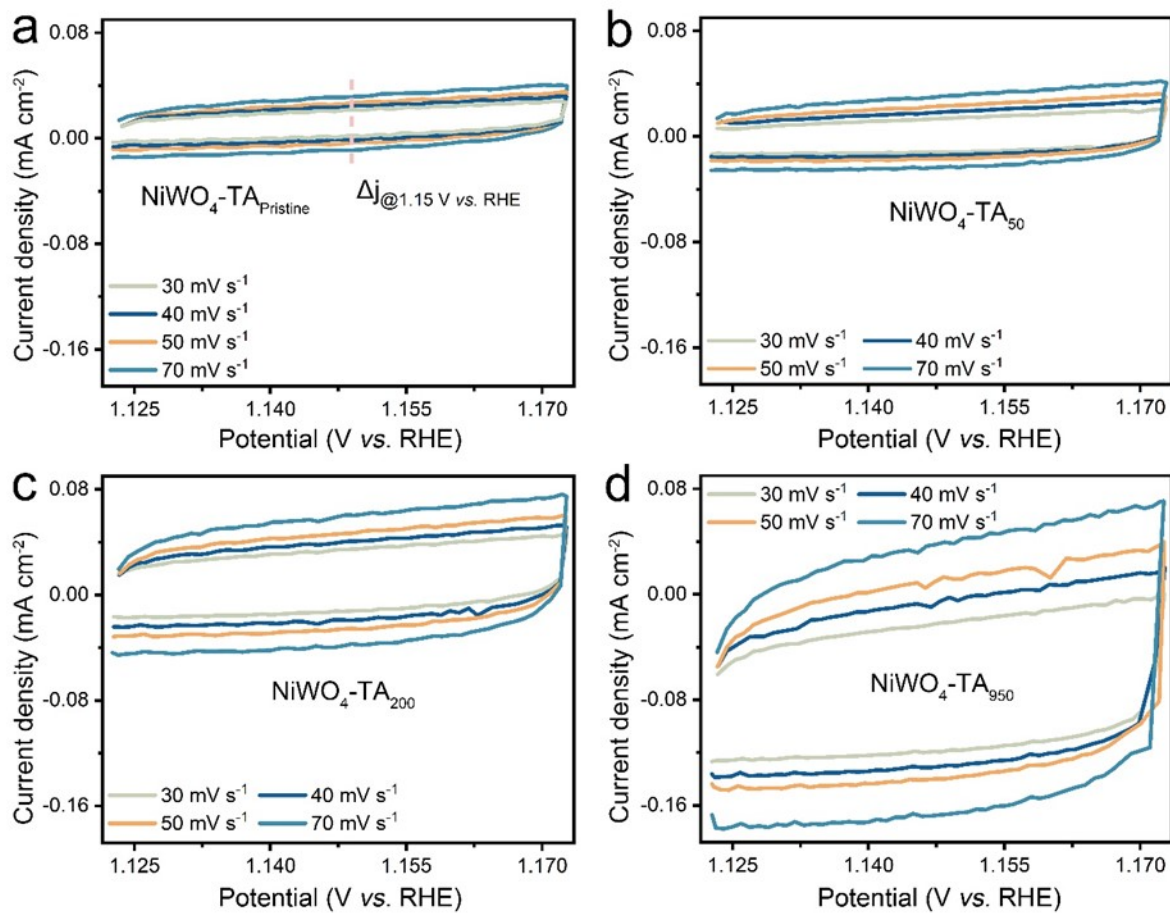
Supplementary Fig. 33 CV scanning curves of **a** NiWO$_4$-TA$_{Pristine}$, **b** NiWO$_4$-TA$_{50}$, **c** NiWO$_4$-TA$_{200}$ and **d** NiWO$_4$-TA$_{950}$ catalysts in 1 M KOH solution at different scan rates in the non-Faradaic potential region (1.12-1.17 V *vs.* RHE).
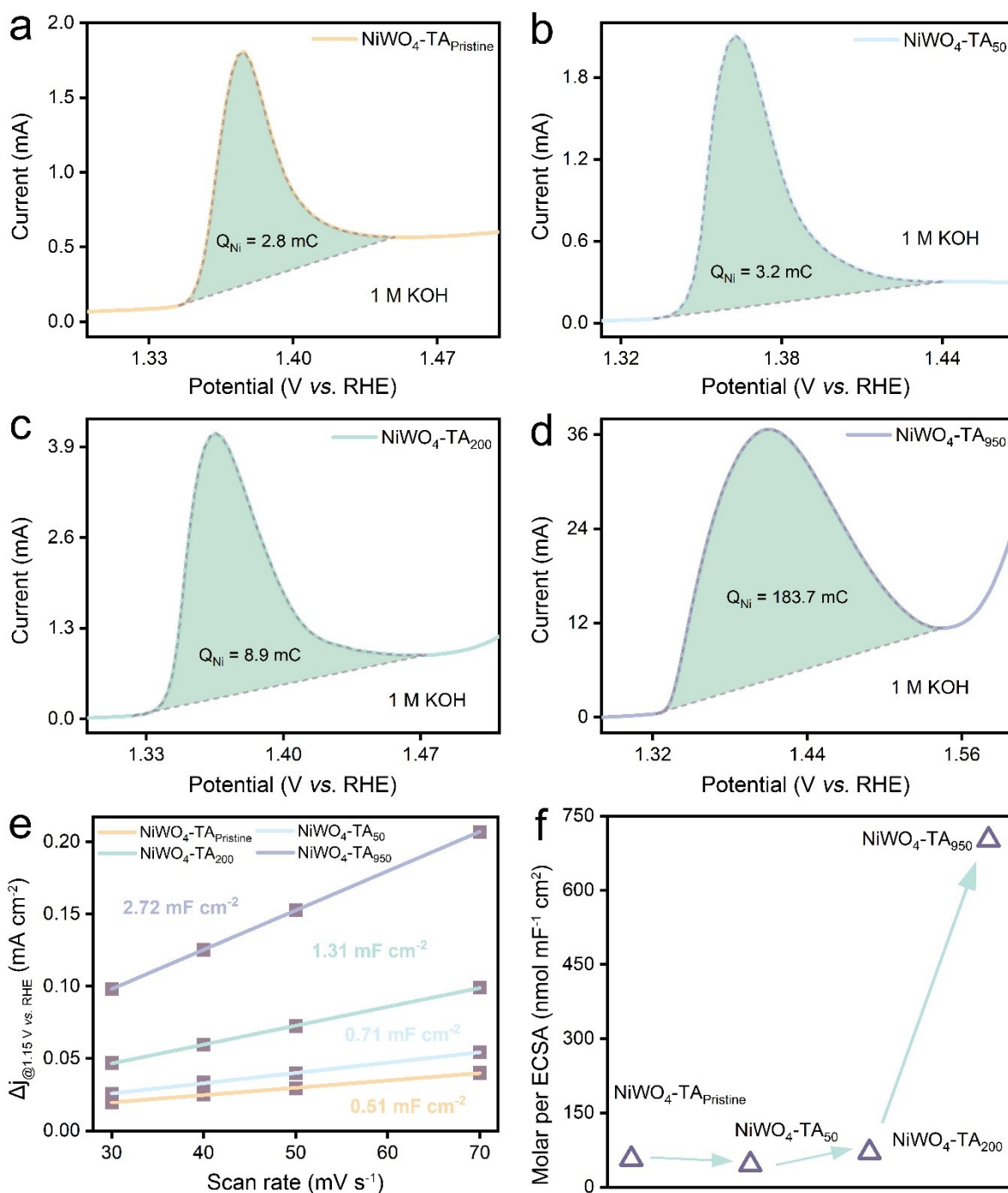
Supplementary Fig. 34 Determination of the dynamic Ni³⁺ formation ability per electrochemical active surface area (ECSA) for NiWO₄-TAₓ catalysts. a-d Integrated Ni^{2+} to Ni^{3+} oxidation peak of (**a**) $NiWO_4\text{-}TA_{Pristine}$, (**b**) $NiWO_4\text{-}TA_{50}$, (**c**) $NiWO_4\text{-}TA_{200}$ and (**d**) $NiWO_4\text{-}TA_{950}$. Q_{Ni} represents the faradic charge transfer of Ni^{2+} to Ni^{3+} redox which is calculated as follows: $Q_{Ni} = \dfrac{S}{v}$, where S is the integrated mathematical area (green shadow), v is the LSV scan rate. **e** Capacitive current density differences at 1.15 V *vs.* RHE as a function of scan rate (data obtained from Supplementary Fig. 33). The linear slope is equivalent to the ECSA of the electrodes. **f** Molar of dynamic Ni³⁺ formed per ECSA (denoted as MPE_{Ni}) under *operando* condition for $NiWO_4\text{-}TA_x$ catalysts. MPE_{Ni} is defined as follows:

$$MPE_{Ni} = \frac{N_A \times Q_{Ni}}{ECSA \times q_e}$$, where N_A represents the Avogadro constant (6.02×10^{23} mol^{-1}), q_e represents the elementary charge (1.6×10^{-19} C).

As can be found in Supplementary Fig. 34f, the molar of dynamic Ni^{3+} formed per ECSA under *operando* condition gradually increases with the activation-degree of the catalysts which rises our curiosity. In general, MPE_{Ni} is mainly governed by the active site type and density of an electrode rather than its ECSA, hence should remain stable in this case. The dramatically boosted MPE_{Ni} of NiWO$_4$-TA$_{950}$ compared to that of NiWO$_4$-TA$_{Pristine}$ indicates the possible formation of a more redox-active phase after the electrochemical treatment in alkaline medium.
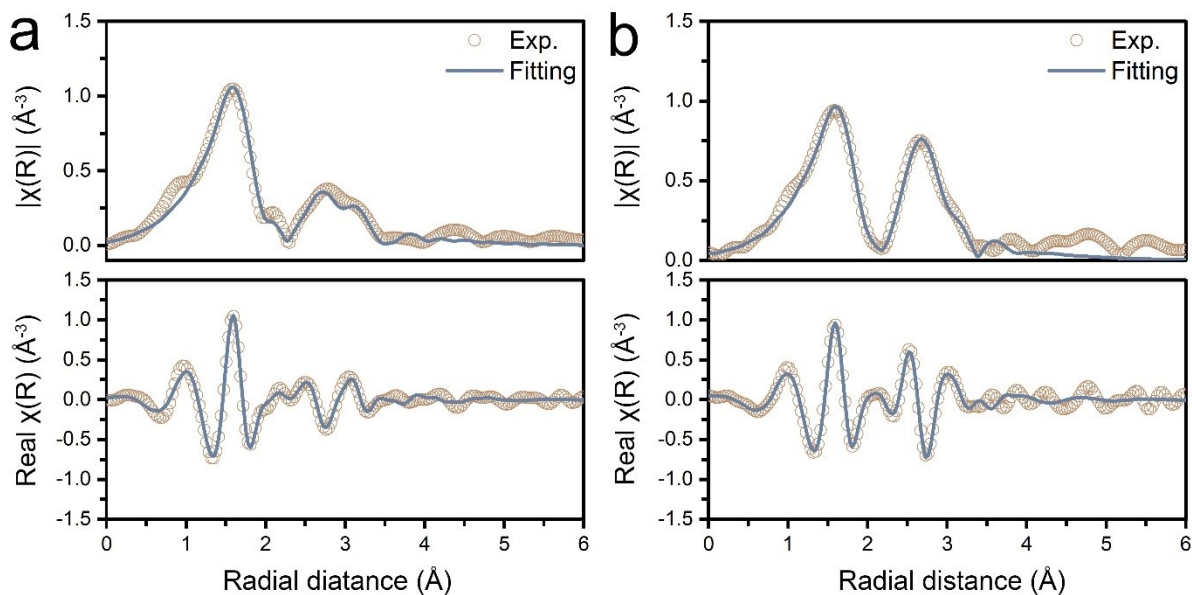
Supplementary Fig. 35 Ni K-edge fitting results. a k^2-weighted R-space EXAFS fitting results of NiWO$_4$-TA$_{pristine}$. **b** k^2-weighted R-space EXAFS fitting results of NiWO$_4$-TA$_{950}$.
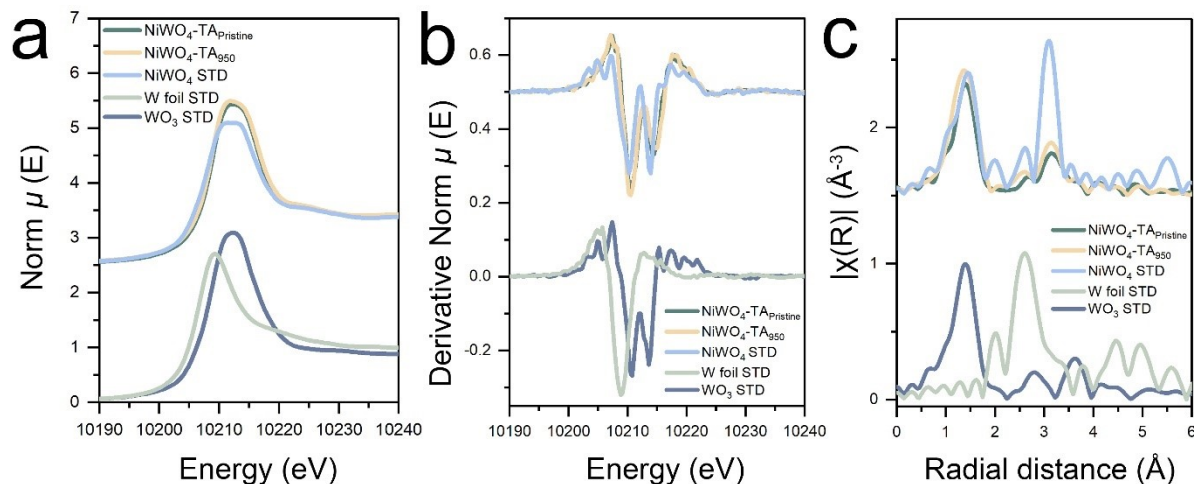
Supplementary Fig. 36 W L_3-edge **a** XANES, **b** Second derivative XANES and **c** k^2-weighted R-space EXAFS of $NiWO_4$-$TA_{pristine}$, $NiWO_4$-TA_{950}, commercial $NiWO_4$, commercial WO_3 and commercial Ni foil. XANES spectra of $NiWO_4$-TA, as the most important bulk characterisation, provide the average valence states of Ni and W contents in the samples. By comparing the Ni K-edge absorption edge position (Figure 4c in the main text) and XANES features (Figure 4d in the main text), a conclusion could be made that Ni^{2+} is the only valence states of Ni species in both $NiWO_4$-$TA_{pristine}$ and $NiWO_4$-TA_{950}. While the EXAFS spectra show completely different coordination structure of Ni content in $NiWO_4$-$TA_{pristine}$ and $NiWO_4$-TA_{950}. The fitting results are listed in Supplementary Table 1. Meanwhile, no obvious changes could be found in XANES spectra at W L_3-edge (Supplementary Fig. 36a), suggesting W^{6+} is dominant in both the pristine and activated samples. The second derivative XANES present a typical two peak feature, which corresponds to 2p to 5d t_{2g} and 2p to 5d e_g electron transitions, respectively (Supplementary Fig. 36b). Therefore, the W species are in octahedral configuration with 6 oxygen atoms coordinated in the first coordination shell, and such octahedral geometry was maintained after the electrochemical treatment.
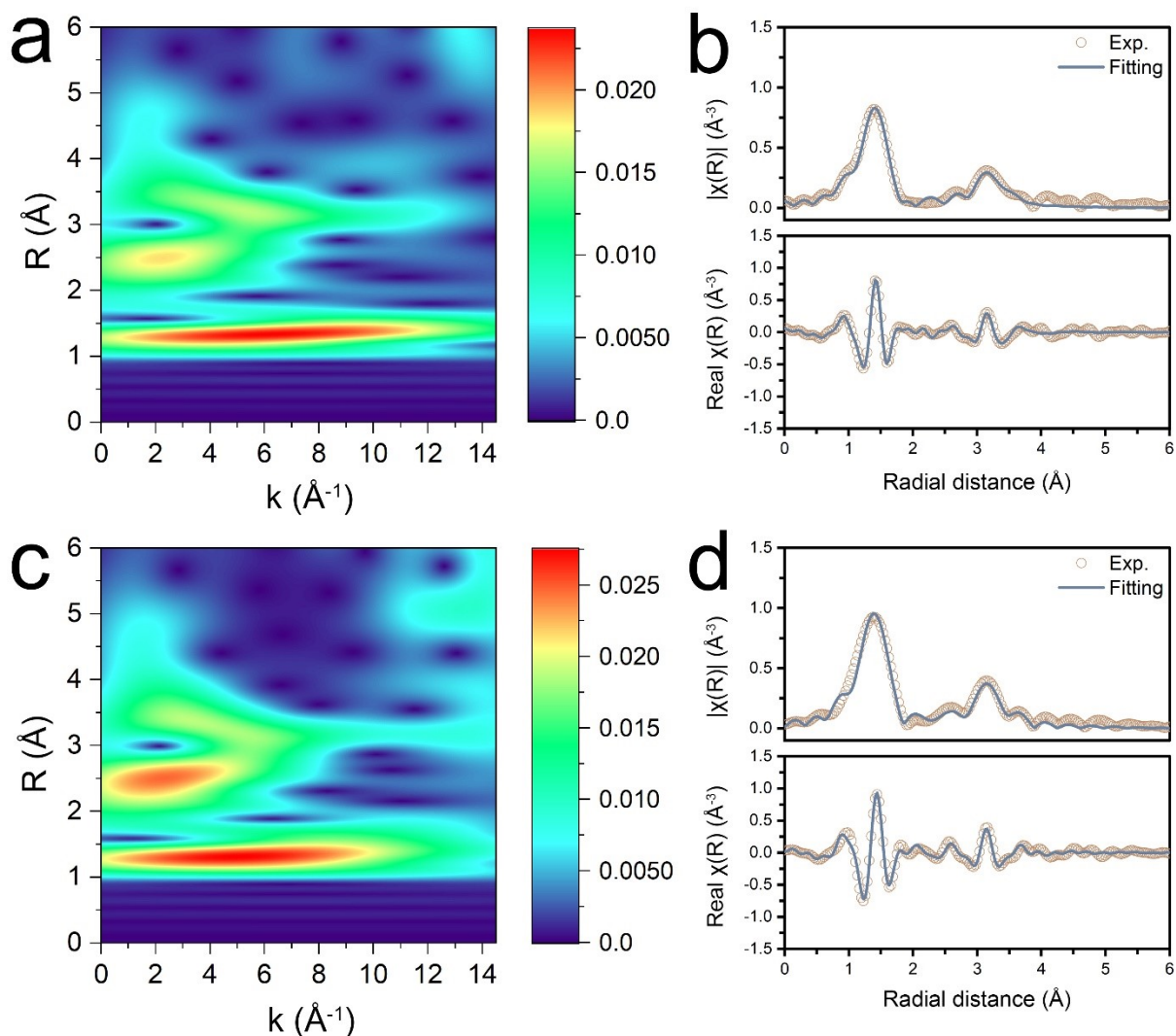
Supplementary Fig. 37 W L_3-edge and fitting results of NiWO$_4$-TA$_{Pristine}$ and NiWO$_4$-TA$_{950}$. **a** k^2-weighted WT-EXAFS and **b** k^2-weighted R-space EXAFS fitting results of NiWO$_4$-TA$_{pristine}$. **c** k^2-weighted WT-EXAFS and **d** k^2-weighted R-space EXAFS fitting results of NiWO$_4$-TA$_{950}$. When comparing the W L_3-edge EXAFS spectra of the pristine and aged catalysts, negligible changes can be observed even in the WT-EXAFS (Supplementary Fig. 37a and c). Therefore, we conclude that W species remained in the aged sample is constant with its original state in the pristine sample, while the significant changes in the second coordination shell of Ni K-edge EXAFS result from the loss of W content and formation of Ni oxides/(oxy)hydroxides.

Supplementary Table 1 Fitting parameters of Ni K-edge EXAFS of NiWO$_4$ sample series.[*]

Paths	Name	NiWO$_4$	NiWO$_4$-TA	NiWO$_4$-TA@500	NiWO$_4$-TA@700	NiWO$_4$-TA$_{950}$
	S_0^2	0.8 (fixed)				
	ΔE_0 (eV)	-4.2±1.8	-5.9±1.2	-4.6±1.7	-3.7±1.6	-4.4±1.4
Ni-O(1)	C.N.	3.1±0.7	3.0±0.6	3.3±0.3	2.0±0.1	2.6±0.4
	R (Å)	1.97±0.03	1.98±0.03	1.98±0.02	1.99±0.01	1.96±0.02
	σ^2	0.003±0.001	0.004±0.002	0.003±0.001	0.005±0.001	0.003±0.001

	C.N.	2.9±0.7	3.0±0.6	2.7±0.3	4.0±0.1	3.4±0.4
Ni-O(2)	R (Å)	2.08±0.03	2.07±0.03	2.11±0.02	2.07±0.01	2.083±0.02
	σ²	0.003±0.001	0.004±0.002	0.003±0.001	0.005±0.001	0.003±0.001
	C.N.	2.0±0.2	2.0±0.2	2.0±0.2	2.0±0.3	5.1±1.0
Ni-Ni(1)	R (Å)	2.96±0.02	2.98±0.02	2.96±0.03	3.04±0.01	2.98±0.01
	σ²	0.011±0.002	0.013±0.003	0.015±0.003	0.005±0.001	0.011±0.002
	C.N.	4.0±0.4	4.0±0.4	4.1±0.5	4.0±0.6	2.7±1.1
Ni-W(1)	R (Å)	3.53±0.03	3.54±0.02	3.52±0.03	3.48±0.01	3.55±0.04
	σ²	0.009±0.004	0.008±0.002	0.008±0.002	0.006±0.001	0.011±0.002
	C.N.	2.0±0.2	2.0±0.2	2.0±0.2	2.0±0.3	1.4±0.6
Ni-W(2)	R (Å)	3.62±0.05	3.66±0.04	3.65±0.04	3.57±0.01	3.70±0.04
	σ²	0.009±0.004	0.008±0.002	0.008±0.002	0.006±0.001	0.011±0.002
	C.N.	2.0±0.2	2.0±0.2	2.0±0.2	2.0±0.3	1.4±0.6
Ni-W(3)	R (Å)	3.70±0.06	3.72±0.04	3.72±0.04	3.72±0.01	3.80±0.04
	σ²	0.009±0.004	0.008±0.002	0.008±0.002	0.006±0.001	0.011±0.002

[*] Correlations of the fitting parameters for each sample,: (1) The sum of C.N. of Ni-O(1) and Ni-O(2) were fixed to be 6.0; (2) For each sample except for NiWO$_4$-TA$_{950}$, the C.N. values of Ni-Ni(1), Ni-W(1), Ni-W(2) and Ni-W(3) were fitted using the same parameter; (3) The σ² values of Ni-O(1) and Ni-O(2) were fitted using the same parameter. set to be the same as σ² of Ni-O(2); (4) The σ² values of Ni-W(1), Ni-W(2) and Ni-W(3) were fitted using the same parameter.

**Supplementary Table 2** Fitting parameters of W L$_3$-edge EXAFS of NiWO$_4$ sample series.[*]

Paths	Name	NiWO$_4$	NiWO$_4$-TA	NiWO$_4$-TA@500	NiWO$_4$-TA@700	NiWO$_4$-TA$_{950}$
	S$_0$²	0.87 (fixed)				
	ΔE$_0$ (eV)	-5.6±2.5	6.4±2.4	1.7±0.8	2.6±1.4	5.1±3.8
	C.N.	2.8±0.1	2.8±0.1	3.0±0.2	2.1±0.3	3.2±0.2
W-O(1)	R (Å)	1.79±0.01	1.79±0.01	1.78±0.01	1.77±0.01	1.79±0.01
	σ²	0.003±0.001	0.003±0.001	0.003±0.001	0.003±0.001	0.003±0.001
	C.N.	1.6±0.1	1.6±0.1	1.5±0.1	2.1±0.3	1.4±0.1
W-O(2)	R (Å)	2.01±0.02	2.01±0.02	1.95±0.03	1.88±0.01	2.01±0.03
	σ²	0.003±0.001	0.003±0.001	0.003±0.001	0.003±0.001	0.003±0.001
	C.N.	1.6±0.1	1.6±0.1	1.5±0.1	2.1±0.3	1.4±0.1
W-O(3)	R (Å)	2.18±0.02	2.18±0.01	2.14±0.03	2.10±0.01	2.18±0.03
	σ²	0.003±0.001	0.003±0.001	0.003±0.001	0.003±0.001	0.003±0.001
	C.N.	2.1±0.2	2.0±0.3	1.9±0.3	2.0±0.4	1.9±0.3
W-W(1)	R (Å)	3.01±0.03	3.02±0.03	2.95±0.04	2.99±0.02	3.01±0.04
	σ²	0.011±0.004	0.012±0.003	0.011±0.004	0.005±0.002	0.006±0.003
	C.N.	4.2±0.5	4.0±0.6	3.9±0.7	4.1±0.8	4.2±0.8
W-Ni(1)	R (Å)	3.50±0.05	3.49±0.03	3.43±0.03	3.46±0.03	3.46±0.04
	σ²	0.011±0.004	0.011±0.004	0.011±0.004	0.003±0.001	0.006±0.003
	C.N.	2.1±0.2	2.0±0.3	2.1±0.3	2.0±0.4	2.1±0.4
W-Ni(2)	R (Å)	3.56±0.04	3.59±0.5	3.53±0.07	3.43±0.06	3.57±0.06
	σ²	0.011±0.004	0.011±0.004	0.011±0.004	0.003±0.001	0.006±0.003
	C.N.	2.1±0.2	2.0±0.3	2.1±0.3	2.0±0.4	2.1±0.4
W-Ni(3)	R (Å)	3.68±0.09	3.69±0.03	3.66±0.06	3.65±0.02	3.67±0.06
	σ²	0.011±0.004	0.011±0.004	0.011±0.004	0.003±0.001	0.006±0.003

[*] Correlations of the fitting parameters for each sample,: (1) The sum of C.N. of W-O(1), W-O(2) and W-O(3) were fixed to be 6.0; (2) The C.N. values of W-Ni(1), W-Ni (2) and W-Ni (3) were fitted using the same parameter; (3) The σ² values of W-O(1), W-O(2) and W-O(3) were fitted using the same parameter; (4) The σ² values of W-Ni(1), W-Ni (2) and W-Ni (3) were fitted using the same parameter.
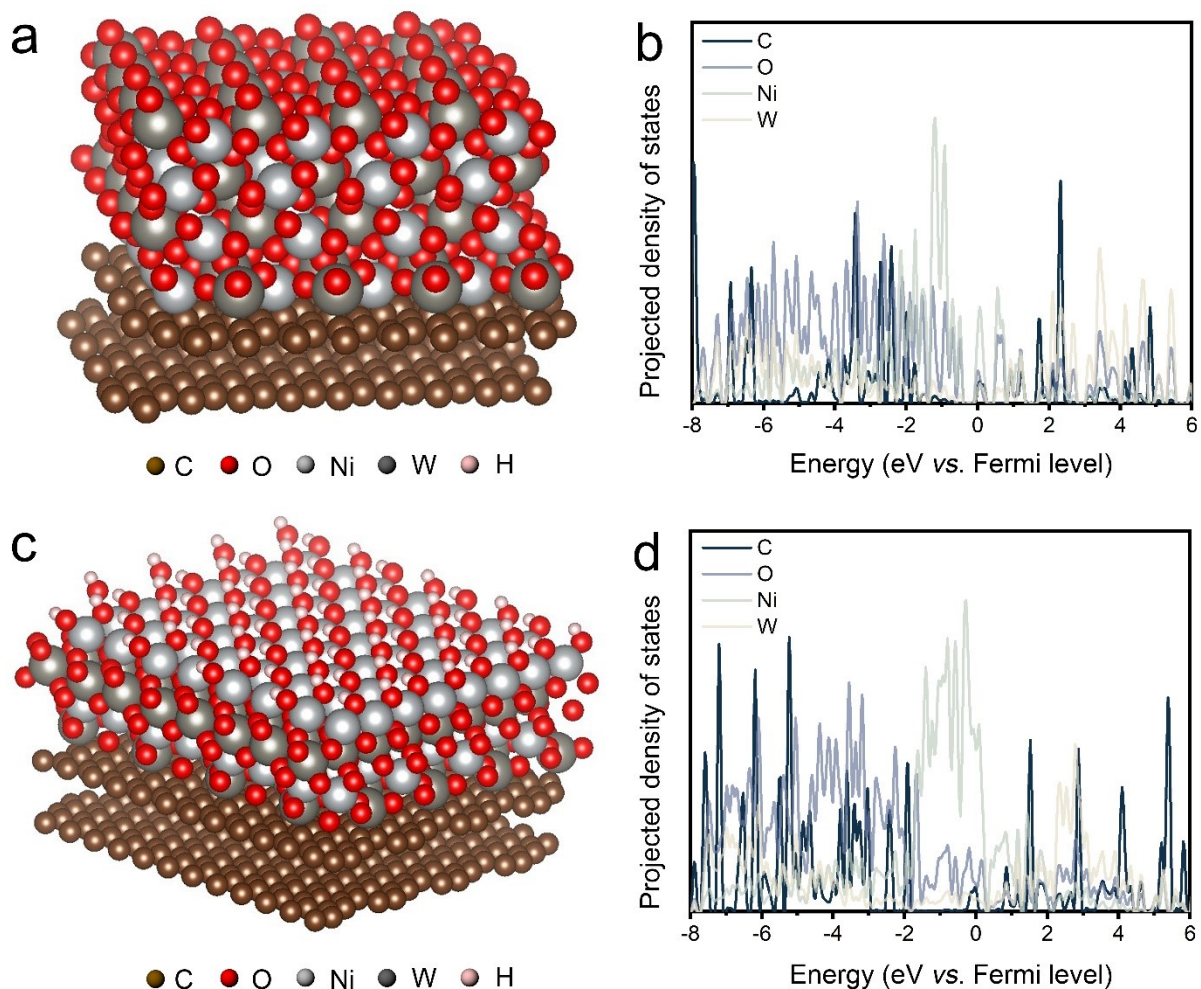
Supplementary Fig. 38 a Schematic illustration and **b** PDOS of pristine NiWO$_4$-TA. **c** Schematic illustration and **d** PDOS of reconstructed NiWO$_4$-TA. Please note the reconstructed NiWO$_4$-TA model is established and TA formed carbon support after hydrothermal reactions, based on the DFT calculations in Supplementary Note 3 (shown later).

Compared with pristine NiWO$_4$-TA, the projected density of states (PDOS) of all the elements are broadened in activated NiWO$_4$-TA, suggesting a higher degree of delocalization in the latter structure. There is no significant PDOS peak at Fermi level for pristine NiWO$_4$-TA, whereas that can be observed at Fermi level for activated NiWO$_4$-TA. A higher distribution of Ni element at Fermi level enables a stronger adsorption capacity for activated NiWO$_4$-TA.
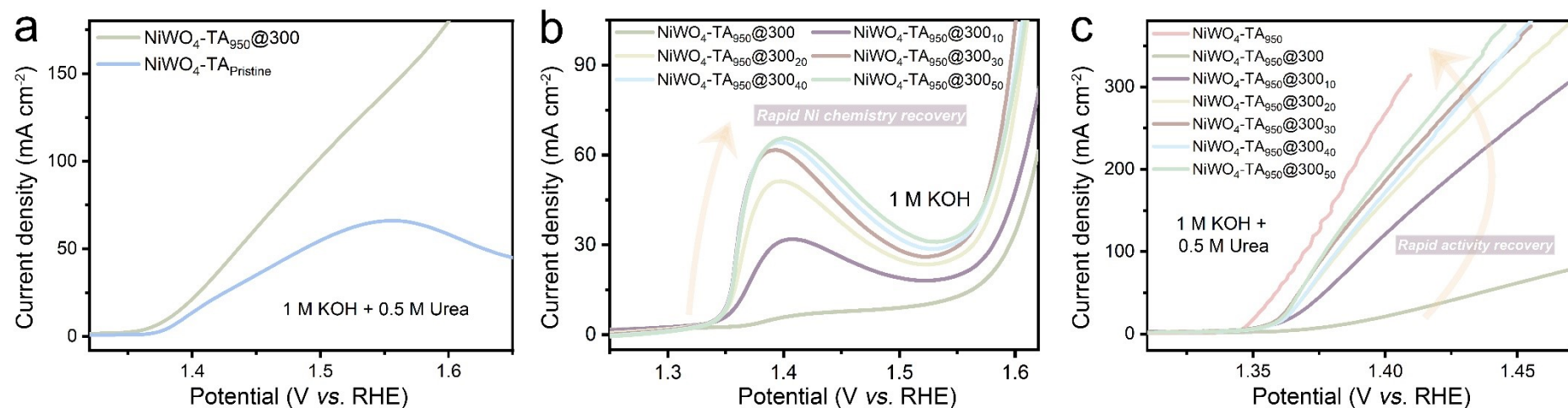
Supplementary Fig. 39 a Urea electrolysis LSVs of NiWO$_4$-TA$_{Pristine}$ and NiWO$_4$-TA$_{950}$@300. **b, c** Evolution of the (**b**) Ni redox chemistry and (**c**) urea electrolysis performance of NiWO$_4$-TA$_{950}$@300$_x$ (*x* represents the number of CV cycles conducted in 1 M KOH prior to water or urea electrolysis test).

To evaluate the influence of the surface oxyhydroxide layer to the electrochemical behaviour of the bimetal oxide catalyst, NiWO$_4$-TA$_{950}$ was annealed at 300 °C (high enough to convert surface oxyhydroxides to oxides but low enough to prevent radical morphological and chemical change in the sub-surface or bulk of the catalyst) under N$_2$ atmosphere for 1 h with a ramp rate of 10 °C min^{-1}. As can be seen in Supplementary Fig. 39a, the annealed catalyst still shows a better activity over that of its pristine counterpart despite loss of the NiOOH layer, confirming the catalytic active nature of the reconstructed Ni-rich phase. Nevertheless, dramatical activity recession can be noticed when comparing the urea electrolysis LSVs of the NiWO$_4$-TA$_{950}$ before and after annealing (Supplementary Fig. 39c). Moreover, the annealed sample also exhibits an inactive Ni redox behaviour (Supplementary Fig. 39b). Surprisingly, a rapid recovery in the Ni chemistry and catalytic activity witnessed after cycling NiWO$_4$-TA$_{950}$@300 in 1 M KOH which can be attributed to the re-formation of the surface oxyhydroxide layer (Supplementary Fig. 39b and c). Hence, it is clear that the NiOOH layer is critical for achieving flexible Ni redox chemistry and desirable catalytic performance despite its insignificant role in directly catalysing chemical reactions. According to previous literatures, nickel oxyhydroxide possesses better wettability than that of nickel (hydro)oxide, thus leading to its superior ion transportation and capacitive behaviour.[11] It takes 30 cycles for NiWO$_4$-TA$_{950}$@300 to achieve a complete oxyhydroxylation since the reconstruction happens not only on the surface, but also within the near-surface region. In a word, the surface oxyhydroxide layer facilitates interaction between the electrolyte and catalyst which is essential for heterogeneous catalysis.
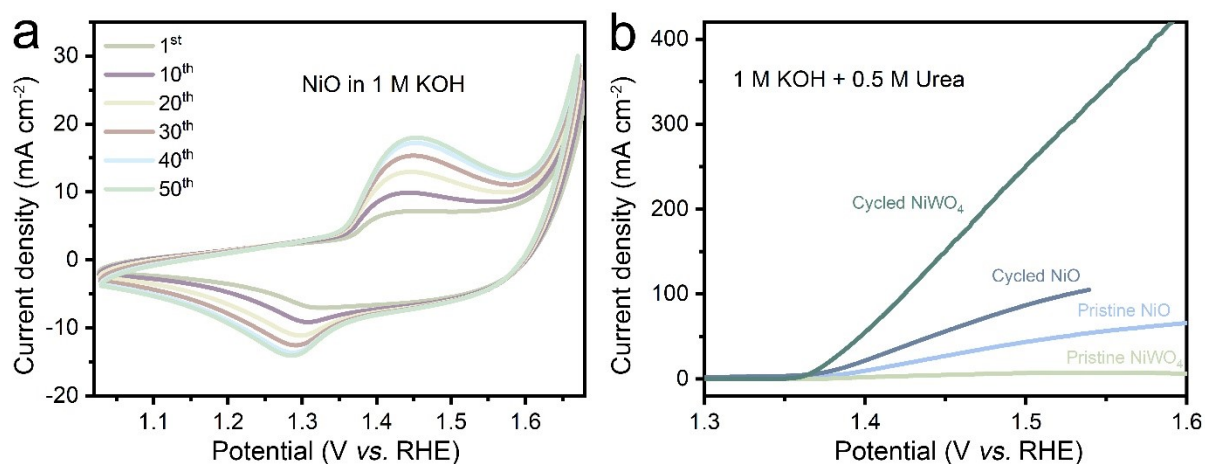
Supplementary Fig. 40 a Evolution of the electrochemical behaviour of NiO in 1 M KOH. **b** LSVs of pristine and activated NiO and $NiWO_4$ scanned in 1 M KOH + 0.5 M urea.

To confirm the role of W leaching in the reconstruction of the $NiWO_4$-series catalysts, the electrochemical behaviour of commercial NiO was investigated. As can be observed in Fig. 40a, the Ni redox chemistry of NiO witnesses an improvement in the first 30-40 CV cycles but remains stable afterwards (similar phenomenon can also be observed on the $NiWO_4$-TA_{950}@300 sample which can be ascribed to the oxyhydroxylation of the oxide species that improves wettability). However, as demonstrated in Supplementary Fig. 40b, such reconstruction only leads to a limited urea electrolysis performance improvement compared to the reconstruction process occurred on $NiWO_4$ (which consists of not only the oxyhydroxylation, but also W leaching). The observation discussed above confirms the importance of W as an leaching agent to generate high performance electrocatalysts.
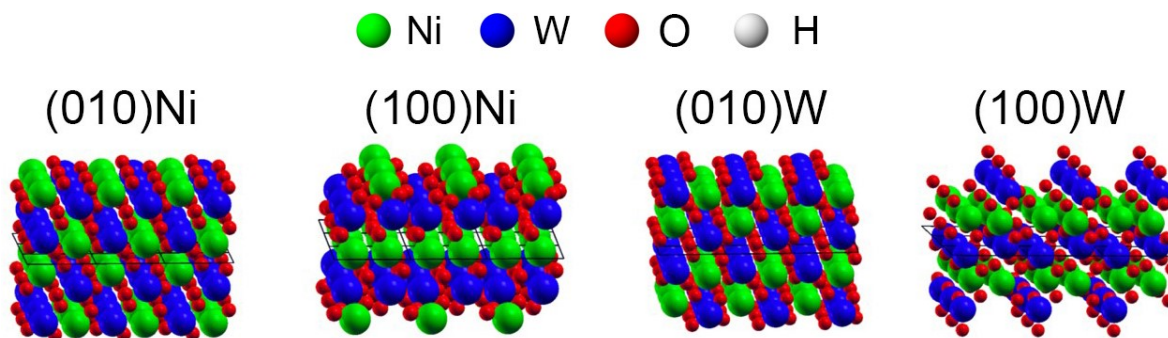
Supplementary Fig. 41 Side views of Ni-terminated (010) and (100), and W-terminated (010) and (100) surface models of $NiWO_4$. The chemical environment of the top and bottom side of the surface models are kept the same. The surface energies are calculated to be 0.63, 1.13, 0.35, and 0.68 J m^{-2} for (010)Ni, (100)Ni, (010)W, and (100)W surface, respectively.
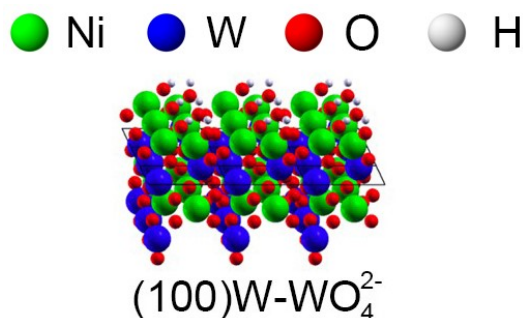
Supplementary Fig. 42 Side views of the (100)W surface after desorption of the surface tungstate ions and their replacement with hydroxide groups. The surface contains a 1:1 ratio of Ni and OH ions.

Supplementary Note 3

DFT calculations were performed by utilizing CRYSTAL17.[12] Basis set were downloaded from CRYSTAL website (http://www.crystal.unito.it/basis-sets.php). All electron basis set were used for Ni (Ni_86-411(41d)G_towler_1992) and O (O_8-411(1d)G_baranek_2013_BaTiO3). Effective core pseudopotentials were used in W basis set (W_cora_1996). The exchange-correlation functional was chosen as PBE0 (including 25% Hartree−Fock exchange). The k-mesh was set to be $8 \times 8 \times 8$. The ferromagnetic (FM) and non-magnetic (NM) phases of $NiWO_4$ were optimised by keeping all the crystal symmetry. The crystal structure of $NiWO_4$ were obtained from Crystallography Open Database (www.crystallography.net, ID: 8103678), with space group P 1 2/c 1 and cell parameters of $a = 4.5992$ Å, $b = 5.6606$ Å, $c = 4.9068$ Å, $\beta = 90.3$. The optimised cell parameters (FM: $a = 4.5855$, $b = 5.7586$, $c = 4.8074$, $\beta = 88.3$; NM: $a = 4.4950$, $b = 5.6287$, $c = 4.8028$, $\beta = 88.69$) have a good agreement with the experimental values. The band gap was calculated to be 4.11 eV in FM calculation. Based on the optimised crystal structure in FM calculation, self-consistent field calculations were performed for two anti-ferromagnetic phase of $NiWO_4$: in AFM(1), the electron spins on Nickel atoms order in the same direction along zigzag atomic chain in c direction, but the spin directions are opposite between two zigzag chain along a direction; in AFM(2), spin directions on Nickel atoms are opposite within one zigzag chain. The total energy results (Supplementary Table 3) agree with literature on that the antiferromagnetic phase is the stable phase at low temperature (below 67 K).[13]

As the focus of this study are the (near)surface properties of $NiWO_4$, and the magnetic order has little effect on energy, we built surface models of $NiWO_4$ based on the optimized FM crystal structure and only consider FM spin polarization of the Ni ions in all surface calculations. Surfaces are modelled with a 2D slab of finite thickness; all slabs considered have symmetrical terminations at the upper and lower faces, as allowed by the inversion centre of the P2/c space group. Only the atomic positions have been relaxed during geometry optimisations of the surface structures, with the lattice parameters fixed at the values optimized for bulk $NiWO_4$.

Structures of the bulk-terminated (100) and (010) surfaces of $NiWO_4$ are shown in Supplementary Fig. 41. Both Ni and W terminations of the (100) and (010) surfaces are possible, and they have been considered individually. Surface energies are calculated as

$E_{surface} = (E_{slab}(n) - nE_{bulk})/2A$, where n is the number of chemical formula units and A the surface area.

The calculated surface energies are 0.63, 0.35, 1.13 and 0.68 J m^{-2} for (010)Ni, (010)W, (100)Ni, and (100)W surfaces. In both (100) and (010) cases the W termination is more stable than the Ni one; this is in contrast with a previous publication,[14] in which W-rich surfaces were found to be unstable, although we note that the (010) surface was considered non polar in [11] while the Ni-W rumpling allows to build both Ni and W exposed terminations. The surface energy for the Ni-terminated surface studied here, of 0.63 J m^{-2} is nearly identical to the value of 0.62 found in [11]. The (100) surface is unstable relative to the (010) both here and in [11], with a similar (100)Ni energy of 1.13 vs 1.01 J m^{-2}. There is therefore good overall agreement of our surface results with literature. All the exposed W ions at the surfaces we have considered are in tetrahedral coordination and form tungstate (WO_4^{2-}) molecular ions, that are stable at high pH values.

Not only are the NiWO$_4$ surfaces electrocatalytically active, as demonstrated by their use in the urea oxidation reaction examined here. In contact with the highly alkaline 1 M KOH electrolyte we may expect redox processes to take place at the NiWO$_4$-electrolyte interface even in absence of an applied voltage. The energy change of the chemical process corresponding to oxidation of the surface Ni^{2+} to Ni^{3+}, balanced by coordination of one hydroxide ion from solution to retain a charge neutral surface cell, was represented through the reaction:

$$Ni^{2+}(surface) + OH^- \rightarrow Ni^{3+}OH^-(surface) + e^-$$
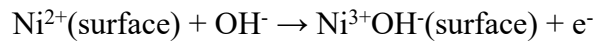
whose calculated reaction energy:

$$E = E_{total} + E_f - E_{solvation(OH^-)}$$

indicates whether spontaneous oxidation of exposed Ni ions can occur. In the expression above, E_{total} is the total energy change of the surface unit cell, E_f is the Fermi energy in the corresponding surface calculation, $E_{solvation(OH^-)}$ is the solvation energy of OH$^-$ taken from literature (-4.77 eV).[15] Only for the Ni-terminated surfaces the calculations converge to stable energy minima. The oxidation energy is calculated as -2.92eV per surface Ni ion on the (100)Ni surface, and -2.74eV/Ni on the (010)Ni one. Both are highly exothermic, indicating that surface Ni is readily oxidized. When normalized to the surface area, the surface Ni oxidation corresponds to energies of -2.00 and -1.69 J m^{-2} on the (010) and (100) surfaces respectively. This energy balance demonstrates two important effects of the catalyst/electrolyte contact: first, Ni oxidation stabilizes Ni-exposed over W-exposed surfaces; it is therefore reasonable to expect that as synthesized NiWO$_4$ will expose preferentially the stable W-terminated planes, while electrocatalytic cycling favours an increased exposure of Ni at surfaces. Second, when normalized to surface area, if all surface Ni is oxidized to 3+ state and hydroxylated, the energy gain of -2.00 and -1.69 J m^{-2} is higher than the surface formation energy for both (010) and (100) surfaces; this suggests that additional surfaces are generated and the exposed surface area increases upon cycling, further enhancing the number of active surface Ni^{3+} sites. Such a process, although energetically feasible is likely to require high activation barriers, hence a large number of CV cycles are needed for it to take place, consistently with the experimental observations.

Experimental measurements also indicate the possibility of W leaching leading to the stable active surfaces. This process is difficult to represent computationally with atomic-level calculations; we have however performed model calculations starting from the (100)W surface, assuming a process in which surface tungstate WO_4^{2-} ions are removed and replaced by two OH$^-$ groups to retain charge neutrality at the surface, corresponding to the reaction:

$$WO_4^{2-} \text{ (surface)} + 2OH^- \text{ (solution)} \rightarrow 2OH^- \text{ (surface)} + WO_4^{2-} \text{ (solution)}$$
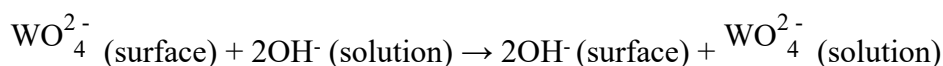
The total energy change for this reaction must accounts for the solvation energy of tungstate and hydroxide ions:

$$E = E_{total} + E_{solvation(WO_4^{2-})} - 2E_{solvation(OH^-)}$$

A picture of the relaxed (100) surface after W leaching (denoted as NiWO-W (100)) is given in Supplementary Fig. 42. The additional hydroxide groups saturate the Ni ions that are exposed upon desorption of the tungstate groups. In this surface each Ni ion is capped by one hydroxide ion; this is the same local environment at the surface observed in the NiOOH compound, that is often taken as representative for the activated catalyst.

The calculated energy for the W leaching process is of +3.13 eV per tungstate ion, excluding the solvation energy of the OH$^-$ and WO_4^{2-} anions. No estimate is available in the literature for the solvation energy of WO_4^{2-}; assuming a value similar to that of the sulfate (SO_4^{2-}) ion of -10.6 eV (-245 Kcal/mol)[16] leaching of surface W in the form of tungstate ions in contact with alkaline electrolytes is predicted as endothermic; the high hydration energy of the tungstate ion may however suggest that dissolution is possible as a slow and irreversible process.

Supplementary Table 3 Calculated energy per formula unit of different magnetic phase of NiWO$_4$.

NiWO$_4$ phase	Energy (Hartree)
FM	-1816.80017
NM	-1816.69082
AFM (1)	-1816.80056
AFM (2)	-1816.80028
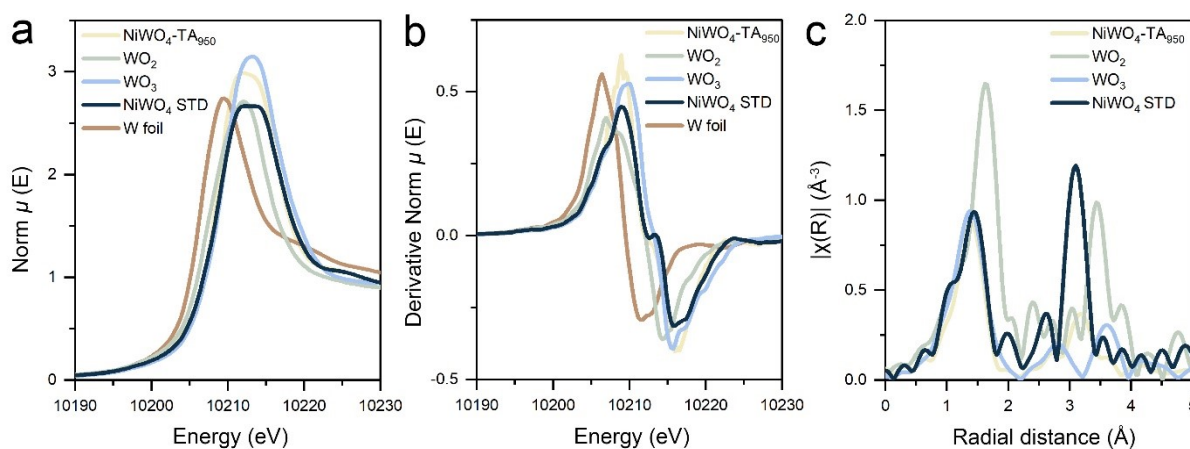
Supplementary Fig. 43 Comparison of NiWO$_4$-TA$_{950}$ with W-foil, WO$_2$, WO$_3$ and NiWO$_4$ standard material in **a** Normalised W L$_3$-edge XANES, **b** Derivative normalised W L$_3$-edge XANES, **c** k^2-weighted R-space EXAFS. The XAFS spectrum of standard sample W-foil, WO$_2$, WO$_3$ and NiWO$_4$ STD are obtained from the SPring-8 BL14B2 XAFS database. The

XAFS spectra of W-foil from Spring-8 is aligned to the XAFS of W-foil measured at DLS, and the calculated energy shift is used to calibrate the other XAFS spectra.

The valence state of W species in our NiWO$_4$-TA$_{950}$ samples is expected to be W^{6+}. First, according to the W L$_3$-edge XANES spectra in Supplementary Fig. 43a and b, the edge position of our NiWO$_4$-TA$_{950}$ sample is nearly identical to that of the standard NiWO$_4$ reference and the WO$_3$ compound, suggesting the 6+ valence state of W in our NiWO$_4$-TA sample. Second, compared to the WO$_2$, the edge position in normalised XANES and the highest inflexion point in the first derivative XANES of NiWO4-TA sample have an energy shift of approx. 0.8 eV and 2.0 eV to higher energies respectively. This is also in good agreement with the previously reported XANES of W^{6+} species.[17-20] Third, the EXAFS spectra of W^{4+} and W^{6+} can be easily distinguished in both first and second coordination shells.[21-23] This is because the ionic radii of the W^{4+}(0.66 Å) are longer than that of W^{6+} (0.60 Å) in oxides. Also, the octahedral [WO$_6$] structure in WO$_3$/NiWO$_4$ are strongly disordered, while the [WO$_6$] in WO$_2$ is nearly symmetric. Therefore, in a brief summary, we conclude the valence state of W in our NiWO$_4$ samples is expected to be W^{6+}.

Moreover, as stated in the Pourbaix (Potential-pH) diagram for tungsten in aqueous solutions at T = 25 °C by Nave *et al.* (please refer to ref. 25), the dissolution of W from NiWO$_4$ should not involve any electrochemical oxidation of W species in either the solid phase catalysts or the liquid phase electrolyte.[24-27] First, the W species in the NiWO$_4$ are already in the form of W^{6+}, which cannot be further oxidised. Second, based on the Pourbaix diagram of W in aqueous solutions, only metallic W and WO_4^{2-} are thermodynamically stable at pH above 8. In our case, our potential was controlled between 0-0.7 V *vs.* Ag/AgCl, which should only associate with WO_4^{2-} in the electrolyte.
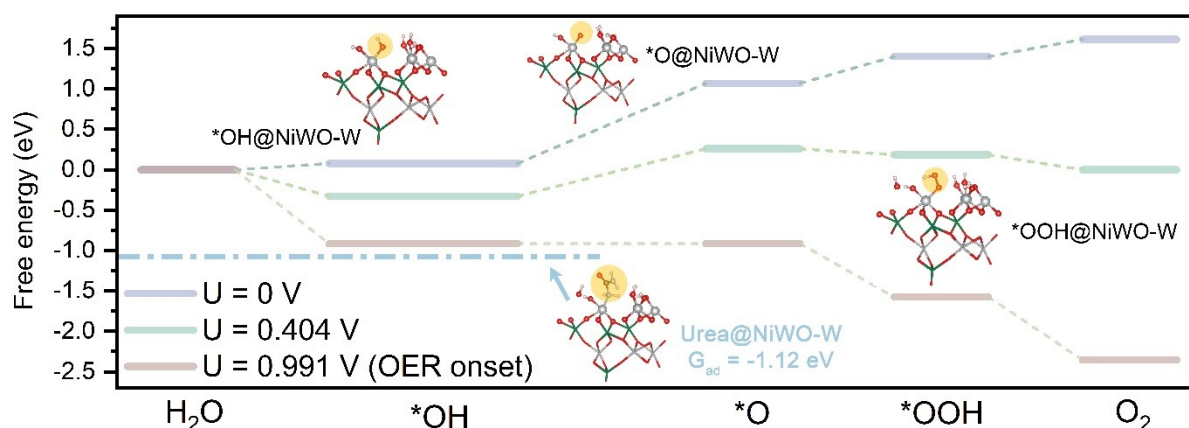
Supplementary Fig. 44 Comparison of the adsorption chemistry of urea and *OH over NiWO-W (100) surface at different applied potentials and free energy diagram of OER over NiWO-W (100) surface at the potential of 0 (grey), 0.404 V (green) and 0.991 V (brown) *vs.* NHE.

To evaluate the adsorption chemistry of several UOR/OER intermediates and OER free energy diagram on the NiWO-W (100) surface, DFT calculations were conducted (simulation methods used here are similar to that in Fig. 2d and Supplementary Note 2). The NiWO-W (100) surface was saturated with OH ligands, which ensures the calculation model is close to

operating condition. The optimized structures of *OH, *O and *OOH on NiWO-W (100) are provided in the upper panel of Supplementary Fig. 44. Moreover, the adsorption structure of urea on NiWO-W (100) is presented in the lower panel of Supplementary Fig. 44. There is one bond generated between N and Ni w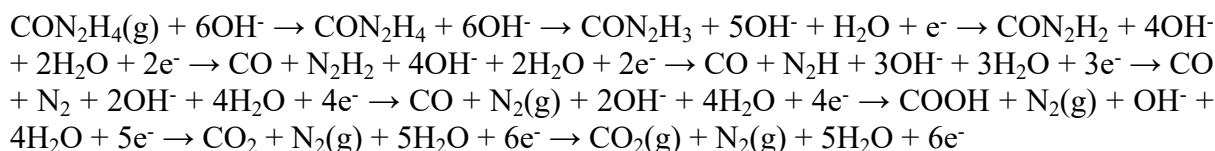ith a bond length of 1.96 Å. The bond length between H from urea and lattice O is 1.61 Å, indicating that there is hydrogen bond interaction between urea and the catalytic surface. The adsorption free energy of urea on NiWO-W (100) is calculated as -1.12 eV which is lower than that simulated on NiOOH (001) surface (-0.49 eV), indicating the more favourable UOR kinetic on the former surface.

Furthermore, we calculated the free energy diagram of OER process on NiWO-W (100) as Supplementary Fig. 44 shows. Similar to the results obtained on NiOOH (001), the adsorption strength of *OH is the key to determine the overall reaction barrier. The reaction rate is hindered by the high adsorption strength of OH ligand on the surface. Hence, the elementary step (*OH → *O) is the rate-determining step. At the potential of 0 V $vs.$ NHE, the overall reaction free energy is 1.61 eV. At the equilibrium potential (0.404 V $vs.$ NHE), it can be observed that the energy state of *OH is under 0 eV, while those of *OH and *OOH are above 0 eV, resulting in an insurmountable energy barrier for the deprotonation of *OH. On the other side, when the applied voltage reaches 0.991 V $vs.$ NHE (overpotential of 0.59 V), there is no energy barrier anymore and the OER can start to perform. It is noteworthy that the OER onset on NiWO-W (100) surface (0.991 V $vs.$ NHE) is higher than that on NiOOH (001) surface (0.87 V $vs.$ NHE), suggesting the more sluggish OER kinetic on the former surface.
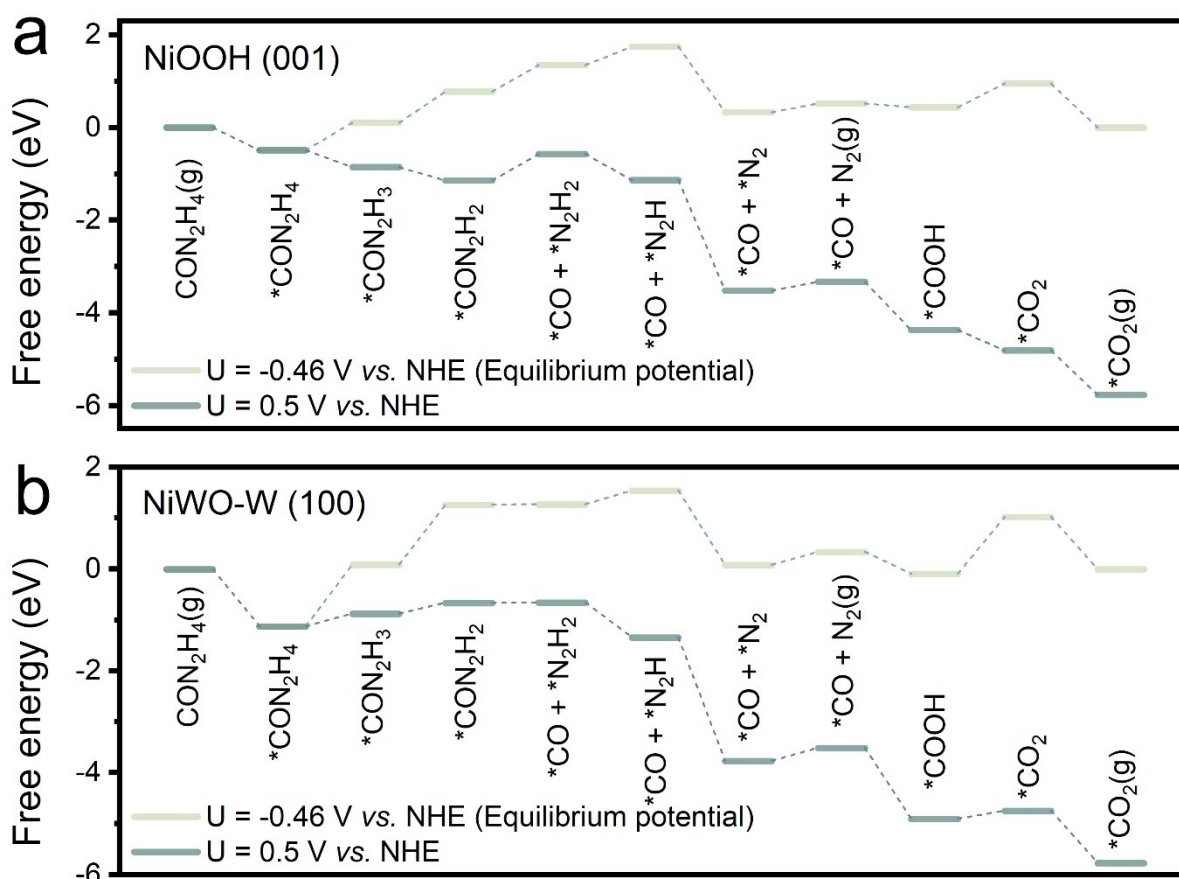
Supplementary Fig. 45 Free energy diagram of UOR on **a** NiOOH (001) and **b** NiWO-W (100) surfaces.

In this calculation, the pH value is 14. The free energy diagram is calculated at equilibrium potential (–0.46 V *vs.* NHE) and working potential (0.5 V *vs.* NHE). The UOR reaction pathways are assumed as:

$CON_2H_4(g) + 6OH^- \rightarrow CON_2H_4 + 6OH^- \rightarrow CON_2H_3 + 5OH^- + H_2O + e^- \rightarrow CON_2H_2 + 4OH^- + 2H_2O + 2e^- \rightarrow CO + N_2H_2 + 4OH^- + 2H_2O + 2e^- \rightarrow CO + N_2H + 3OH^- + 3H_2O + 3e^- \rightarrow CO + N_2 + 2OH^- + 4H_2O + 4e^- \rightarrow CO + N_2(g) + 2OH^- + 4H_2O + 4e^- \rightarrow COOH + N_2(g) + OH^- + 4H_2O + 5e^- \rightarrow CO_2 + N_2(g) + 5H_2O + 6e^- \rightarrow CO_2(g) + N_2(g) + 5H_2O + 6e^-$

For the NiOOH model (Supplementary Fig. 45a), the rate-determining step is $CON_2H_3 + OH^- \rightarrow CON_2H_2 + H_2O + e^-$ at the equilibrium potential, whereas it is $CON_2H_2 \rightarrow CO + N_2H_2$ at the working potential. For the NiWO-W model (Supplementary Fig. 45b), the rate-determining step is $CON_2H_4 + OH^- \rightarrow CON_2H_3 + H_2O + e^-$ at the equilibrium potential, whereas it is $^*N_2 \rightarrow N_2(g)$ at the working potential. Under working potentials, all the oxidative steps in UOR are favourable in thermodynamics for the Ni^{3+}-based surfaces. Similar conclusion was mentioned by Chen *et al.* previously.[28]
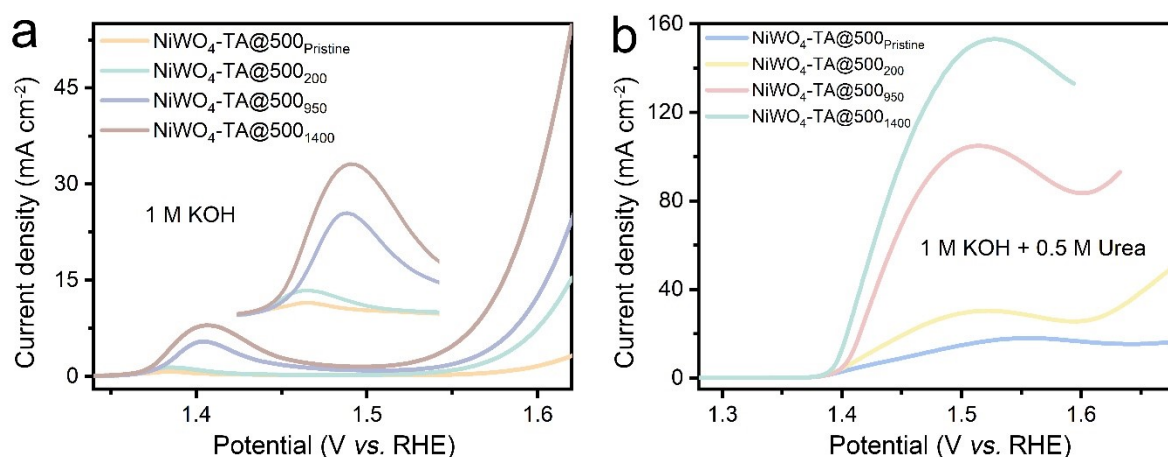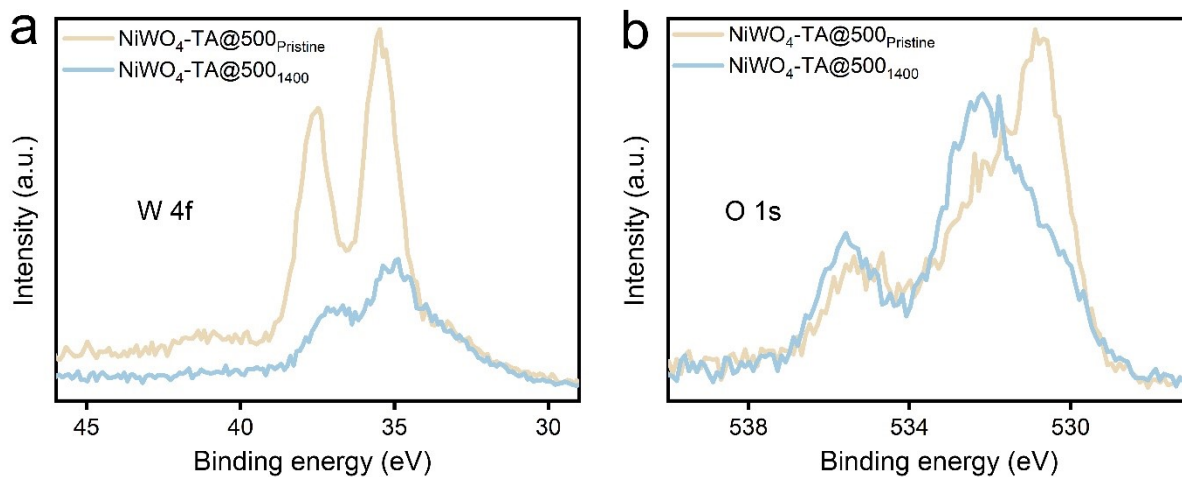

Supplementary Fig. 46 LSVs of NiWO$_4$-TA@500$_x$ (*x* represents the number of CVs conducted in 1 M KOH prior to water or urea electrolysis test) evaluated in (**a**) 1 M KOH and (**b**) 1 M KOH + 0.5 M urea.

Similar to NiWO$_4$-TA, NiWO$_4$-TA@500 also witnessed a boost in its Ni redox chemistry after electrochemical treatment in 1 M KOH (Supplementary Fig. 46a). Moreover, the XPS spectra in Supplementary Fig. 47 and 48 confirm the leaching of W. In addition, the ECSA of the annealed sample is found to increase with its aging degree (Supplementary Fig. 49 and 50e). The observed data suggests NiWO$_4$-TA@500 might have a similar reconstruction scheme with that of NiWO$_4$-TA when cycling in alkaline medium. However, according to Supplementary Fig. 46b, a UOR/OER competition peak can still be noticed even after 1400 CVs. The failure in eradicating the UOR/OER competition can be ascribed to the much less active Ni redox chemistry of the NiWO$_4$-TA@500$_x$ samples compared to that of NiWO$_4$-TA$_x$. Based on the XRD observation in Supplementary Fig. 1a, samples after annealing exhibit higher crystallization degree which might make them difficult to be engineered by the

electrochemical treatment. This hypothesis was later confirmed by *ex-situ* XPS tests. As shown in Supplementary Fig. 47b, the proportion of 6+ W in NiWO$_4$-TA@500 has only reduced 25% and 33%, respectively after 950 and 1400 CVs, much lower than that of NiWO$_4$-TA (37% after 950 CVs), indicating a less vigorous W leaching. Similar conclusion can be reached in the XPS O1s spectra as well (Supplementary Fig. 47c). Therefore, it is believed the high crystallization nature of NiWO$_4$-TA@500 impedes its reconstruction, accordingly resulting in deficient dynamic Ni^{3+} active sites.
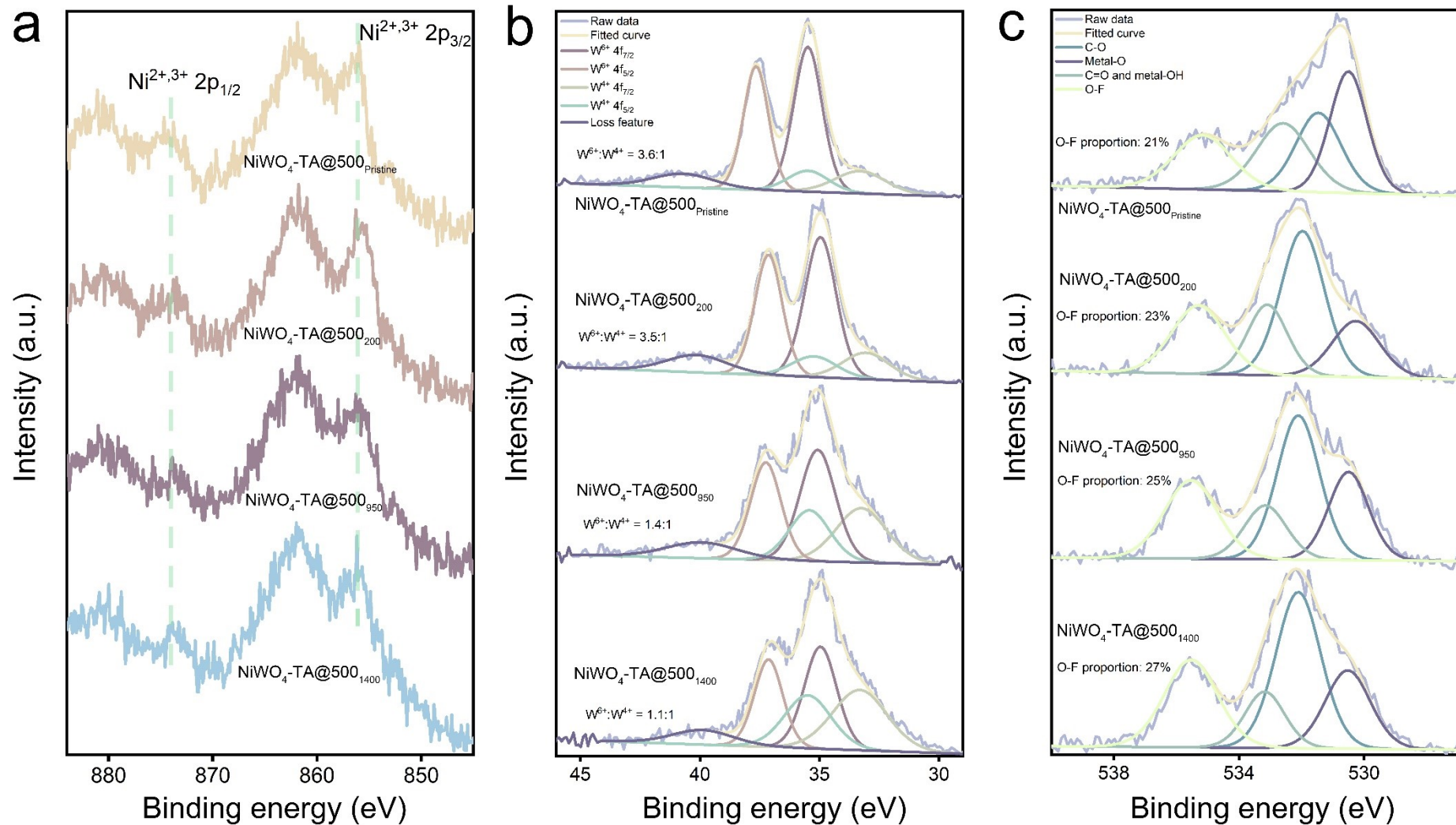
Supplementary Fig. 47 XPS spectra of **a** Ni 2p, **b** W 4f, and **c** O 1s peaks for NiWO$_4$-TA@500$_x$ (x = 0, 200 and 950). No obvious change can be found in the Ni 2p spectra. Meanwhile, the loss of W and O can be evidenced by the increased W^{4+} and O-F bond composition in the W 4f and O 1s spectra. However, the composition change in NiWO$_4$-TA@500 is not as pronounced as that in the NiWO$_4$-TA case.

Supplementary Fig. 48 Comparison of the XPS **a** W 4f and **b** O 1s spectra of NiWO$_4$-TA@500$_{Pristine}$ and NiWO$_4$-TA@500$_{1400}$.
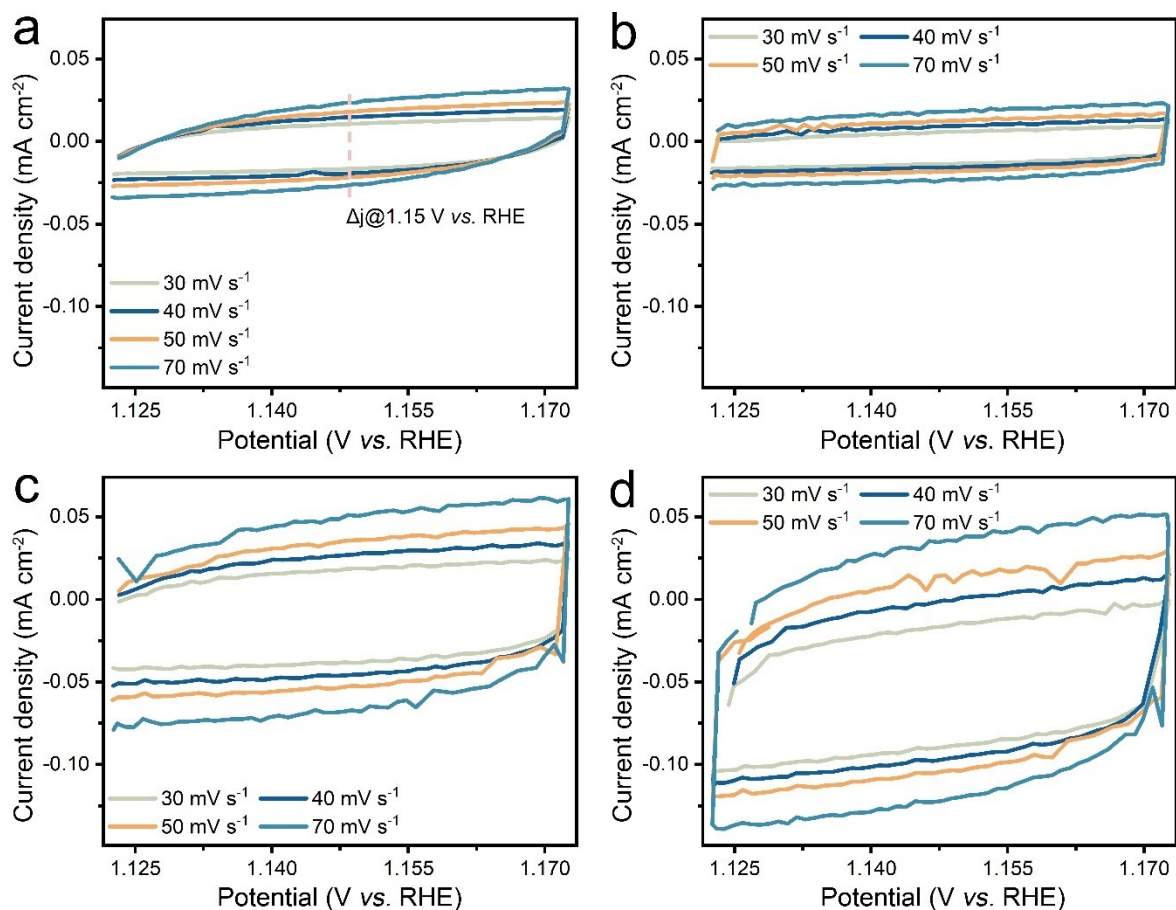
Supplementary Fig. 49 CV scanning curves of **a** NiWO$_4$-TA@500$_{Pristine}$, **b** NiWO$_4$-TA@500$_{200}$, **c** NiWO$_4$-TA@500$_{950}$ and **d** NiWO$_4$-TA@500$_{1400}$ catalysts in 1 M KOH solution at different scan rates in the non-Faradaic potential region (1.12-1.17 V *vs.* RHE).
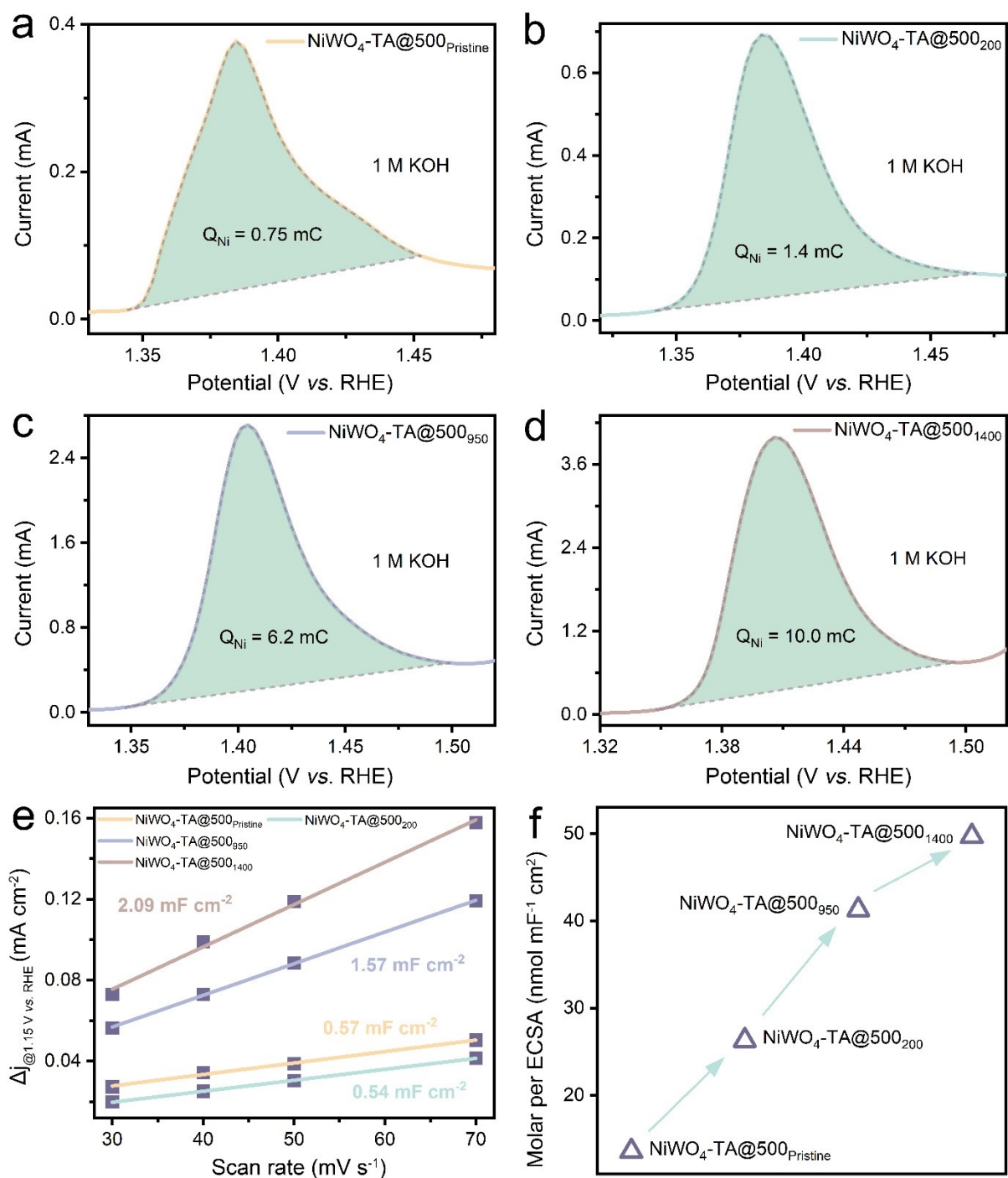
Supplementary Fig. 50 Determination of the dynamic Ni^{3+} formation ability per ECSA for NiWO$_4$-TA@500$_x$ catalysts. a-d Integrated Ni^{2+} to Ni^{3+} oxidation peak of (**a**) NiWO$_4$-TA@500$_{Pristine}$, (**b**) NiWO$_4$-TA@500$_{200}$, (**c**) NiWO$_4$-TA@500$_{950}$ and (**d**) NiWO$_4$-TA@500$_{1400}$. **e** Capacitive current density differences at 1.15 V *vs*. RHE as a function of scan rate (data obtained from Supplementary Fig. 49). The linear slope is equivalent to the ECSA of the catalysts. **f** MPE$_{Ni}$ under *operando* condition for NiWO$_4$-TA@500$_x$ catalysts. Similar to that of NiWO$_4$-TA$_x$, the MPE$_{Ni}$ value of NiWO$_4$-TA@500$_x$ increases with the aging degree of the catalysts, double confirming the formation of the reconstructed redox active Ni-rich phase.
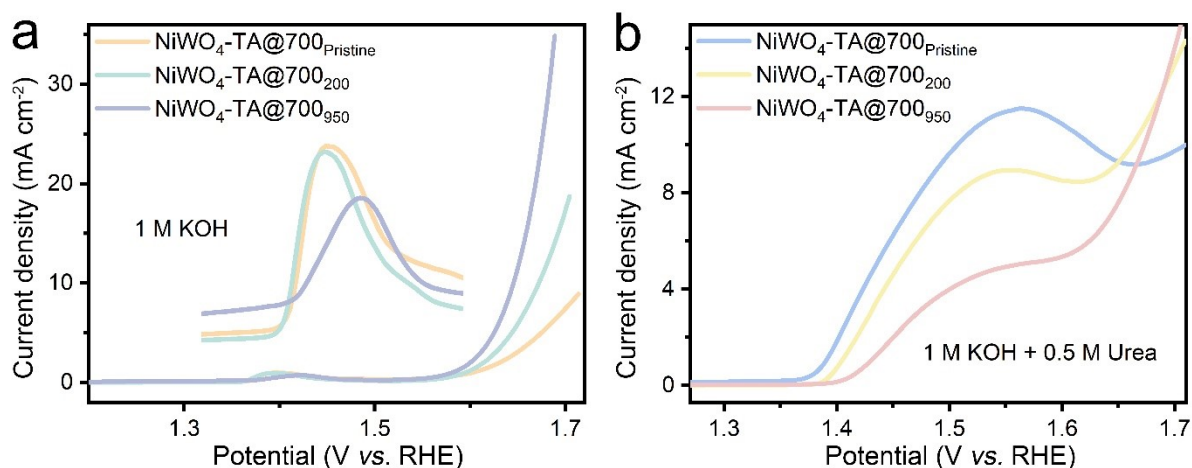
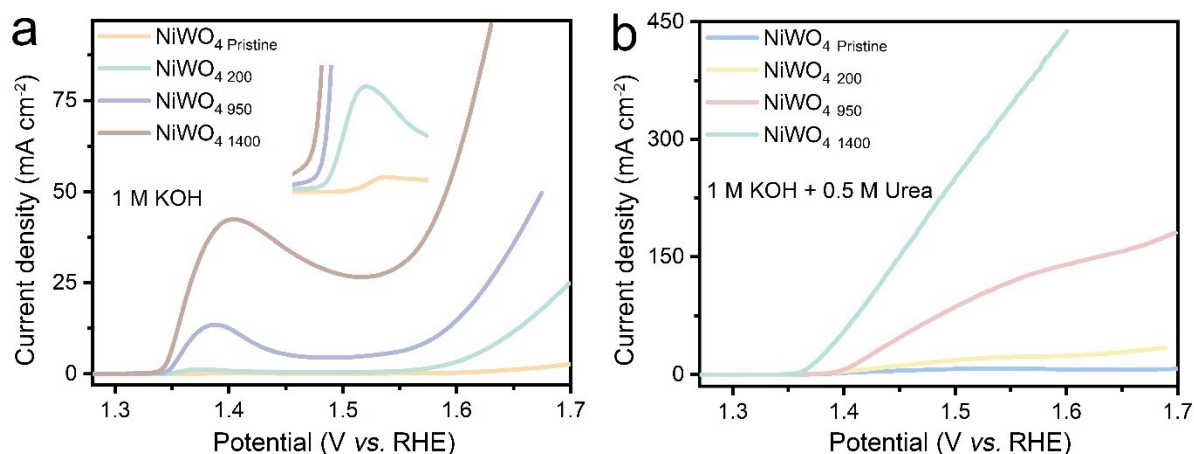**Supplementary Fig. 51** LSVs of $NiWO_4$-TA@700_x (x represents the number of CVs conducted in 1 M KOH prior to water or urea electrolysis test) evaluated in (**a**) 1 M KOH and (**b**) 1 M KOH + 0.5 M urea.

From the XRD pattern in Supplementary Fig. 1a, the TEM images in Supplementary Fig. 1b-i, the Ni K-edge and W L_3-edge XAFS results in Supplementary Fig. 3, a gradually increased $NiWO_4$ crystallinity can be observed after annealing treatment. (please see Supplementary Note 4 for detailed discussion). Interestingly, the ratio of 6+ (regarded as dissoluble W by computational calculation)/4+ W reduces by 80.3% after 950 CV cycles for $NiWO_4$-TA with low-crystallinity but only by 61.1% when it comes to $NiWO_4$-TA@500 (which exhibits higher crystallinity), as can be inferred from the XPS W 4f spectra (Supplementary Fig. 31 and 47). In addition, the Ni^{2+}/Ni^{3+} oxidation peak of $NiWO_4$-TA increased by 65.7 times after 950 CV cycles, much higher than that of $NiWO_4$-TA@500 (only 8.3 times) as shown in Supplementary Fig. 34 and 50. Hence, there is a negative relationship between the catalyst crystallinity and chemical composition/redox behaviour alteration, pointing to the hypothesis that the lower the $NiWO_4$ crystallinity, the higher the W leaching rate.

To further elucidate the relationship between the crystallinity and reconstruction chemistry of the bimetal oxide catalyst, $NiWO_4$-TA was calcinated at 700 °C, after which a highly crystalized structure has been constructed (Supplementary Fig. 1a). According to the electrochemical results in Supplementary Fig. 51a, no obvious Ni redox behaviour change can be noticed for $NiWO_4$-TA@700 even after 200 CVs in 1 M KOH. Surprisingly, a weaker Ni^{2+}/Ni^{3+} transition peak can be witnessed after further 700 cycles of CV which might be attributed to degradation of the catalyst. Similar trend can also be observed in the urea electrolysis test (Supplementary Fig. 51b). The reversed electrochemical behaviour alteration trend of $NiWO_4$-TA@700 compared to that of $NiWO_4$-TA and $NiWO_4$-TA@500 can be explained by the following two scenarios. (1) when the catalyst shows low crystallinity → it exhibits vigorous reconstruction chemistry → benefits from catalyst reconstruction is larger than detriments from degradation → a boost in Ni redox chemistry will be observed → the catalyst will exhibit improved urea electrolysis activity; (2) when the catalyst shows high crystallinity → it exhibits inactive reconstruction chemistry → benefits from catalyst reconstruction is less than detriments from degradation → a decrease in Ni redox chemistry will be observed → the catalyst will exhibit deteriorated urea electrolysis activity. In other words, the reconstruction chemistry can be controlled by manipulating the crystallinity of the catalyst.

It is worth pointing out that the annealing treatment changed not only the crystallinity, but also many other physical/chemical properties of the catalysts (*i.e.* electrical conductivity of the TA-derived substrate, crystal size and defect density of the bimetal oxides). As for the further

investigation, data-driven theoretical study is required to verify the correctness of the proposed hypothesis (please see Supplementary Note 4 for more details).

Supplementary Fig. 52 LSVs of $NiWO_4$ $_x$ (x represents the number of CVs conducted in 1 M KOH prior to water or urea electrolysis test) evaluated in **a** 1 M KOH and **b** 1 M KOH + 0.5 M urea.

Pure $NiWO_4$ was tested in order to investigate the role of the TA-derived hydrochar substrate. As demonstrated in Supplementary Fig. 52a, a significant boost in Ni redox capacitive behaviour of $NiWO_4$ can be confirmed. However, the urea electrolysis results in Supplementary Fig. 52b suggest at least 1400 cycles of CV is required for $NiWO_4$ to eradicate the UOR/OER competition, far more than that of the catalyst which hybrids with carbon support. It is believed the composited $NiWO_4$ has more reconstructable sites exposed to electrolyte, thus showing more facile reconstruction response. In a word, the reconstruction process can be controlled by adjusting the ECSA of the electrode.
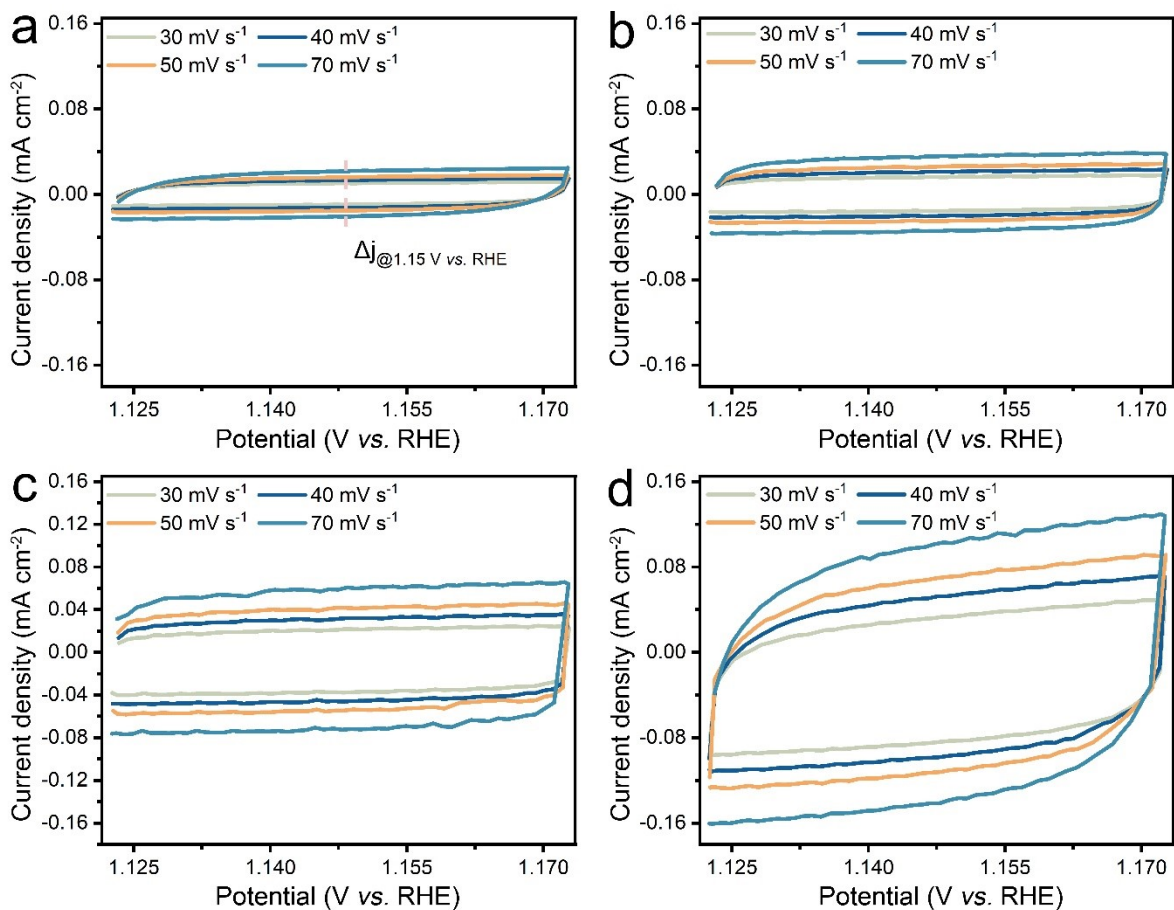
Supplementary Fig. 53 CV scanning curves of **a** $NiWO_4$ $_{Pristine}$, **b** $NiWO_4$ $_{200}$, **c** $NiWO_4$ $_{950}$ and **d** $NiWO_4$ $_{1400}$ catalysts in 1 M KOH solution at different scan rates in the non-Faradaic potential region (1.12-1.17 V *vs*. RHE).
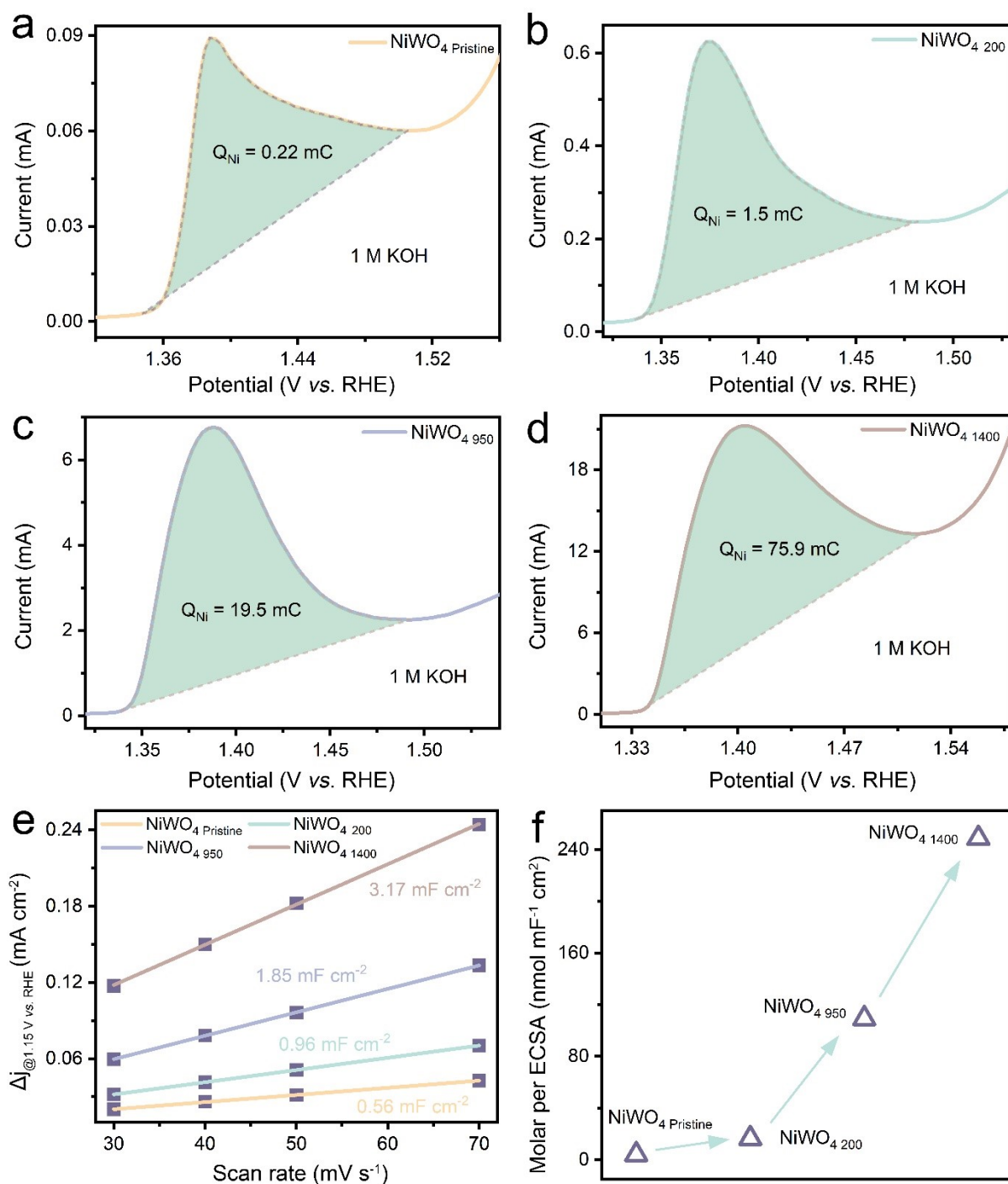
Supplementary Fig. 54 Determination of the dynamic Ni³⁺ formation ability per ECSA for NiWO₄ ₓ catalysts. a-d Integrated Ni^{2+} to Ni^{3+} oxidation peak of (**a**) NiWO₄ ₚᵣᵢₛₜᵢₙₑ, (**b**) NiWO₄ ₂₀₀, (**c**) NiWO₄ ₉₅₀ and (**d**) NiWO₄ ₁₄₀₀. **e** Capacitive current density differences at 1.15 V *vs.* RHE as a function of scan rate (data obtained from Supplementary Fig. 53). The linear slope is equivalent to the ECSA of the catalysts. **f** MPE_Ni under *operando* condition for NiWO₄ ₓ catalysts. Similar to that of NiWO₄-TAₓ, the MPE_Ni value of NiWO₄ ₓ increases with the aging degree of the catalysts, further confirming the formation of the reconstructed redox active Ni-rich phase. It is noteworthy that NiWO₄ requires 1400 CV cycles to boost its Ni^{2+}/Ni^{3+} redox activity to a comparable value with that of NiWO₄-TA₉₅₀ (Supplementary Fig. 34d and 54d), indicating the NiWO₄ particle will deliver more reconstructible sites exposed to the electrolyte if hybridised with TA.
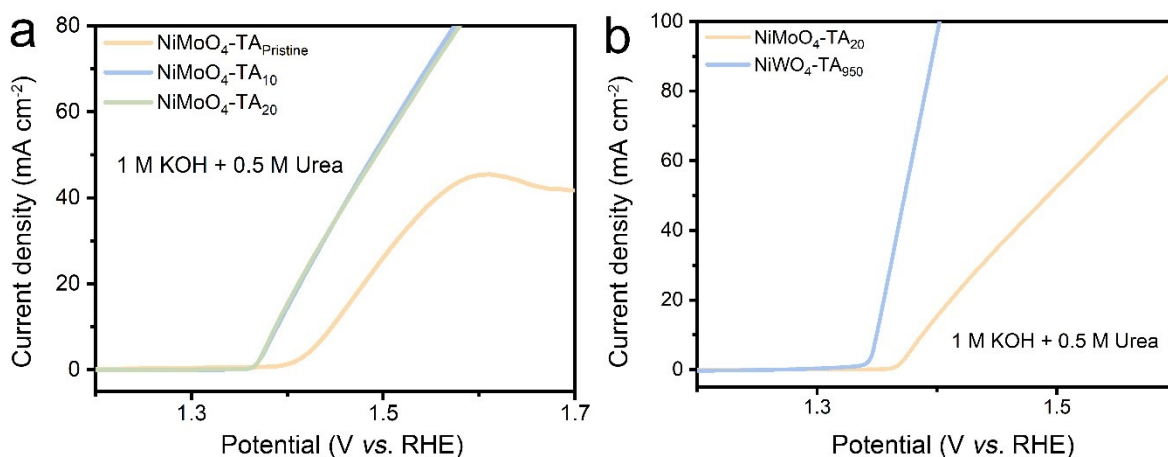
Supplementary Note 4

Through comparing the physical/chemical properties of the $NiWO_4$-series samples, the possible leaching chemistry-influencing factors are listed below.

Crystal structure: Based on the XRD patterns (Supplementary Fig. 1a), $NiWO_4$ and $NiWO_4$-TA have the similar crystallinity (nearly identical diffraction peak FWHM at each corresponding diffraction angles). While the $NiWO_4$-TA@500 has much narrower XRD peak FWHM at 2theta = 14 which can be attributed to (002) lattice plane. In contrast, the $NiWO_4$-TA@700 sample has the narrowest XRD peak FWHM, suggesting much better crystallinity and long-range order in the crystal structure.

Particle morphologies: From the TEM images (Supplementary Fig. 1), the morphology differences of these TA samples could be clearly observed. Addition of large-surface-area substrates could lead to dispersed particle distribution. Sintering could result in particle aggregation. Consequently, the sample will show varied ECSA.

Electronic structure: Ni K-edge XANES of all pristine $NiWO_4$-series samples ($NiWO_4$, $NiWO_4$-TA, $NiWO_4$-TA@500 and $NiWO_4$-TA@700) are featured with Ni^{2+} components. Correspondingly, the W^{6+} species is also dominant in the W L3-edge XANES (Fig. 4 in the manuscript and Supplementary Fig. 3, 36 and 43. The peaks around 856-858 eV (dashed lines) in the XPS Ni 2p spectra (Supplementary Fig. 2a) of pristine $NiWO_4$-series samples represent surface Ni in 2+ (oxide or hydroxide) or 3+ (oxyhydroxide) oxidation states. It is worth noting that the shift of Ni spin-orbit peaks of the annealed samples to lower binding energy can be attributed to the conversion of their surface oxyhydroxide component to oxide by calcination. Differently, as demonstrated in Supplementary Fig. 2b, the valence state of W, of which W^{6+} species is dominant, remains stable after sintering.

Coordination structure: On the one hand, for the Ni K-edge, all the four pristine $NiWO_4$-series samples have the same 6-O coordinated first shell, while the Debye-Waller factors of the second shell Ni-W and Ni-Ni scatterings for $NiWO_4$-TA@700 samples become smaller due to the improved crystallinity and long-range order (Supplementary Table 1, Figure 4 in the manuscript and Supplementary Fig. 35) which is in consistent with the XRD patterns. In contrast, the activated $NiWO_4$-TA sample ($NiWO_4$-TA$_{950}$) has completely different second shell coordination structure, the Ni-Ni coordination increased dramatically from 2.0 to 5.1, accompanied with the decrease in Ni-W coordination number from 6.0 to 4.1 (Supplementary Table 1). This means after 950 CV cycles, the coordination environment of Ni in the sample has been changed due to the formation of additional Ni-rich phase (DFT results in Supplementary Note 3 also reach similar conclusion). On the other hand, negligible difference could be observed from the W L3-edge EXAFS spectra of pristine and cycled samples (Supplementary 36, 37and 43). The W species in both samples preserved the 6-O coordinated first shell and also the same W-Ni/W scattering features in the second shell. DFT calculations (Supplementary Note 3) and Pourbaix (Potential-pH) diagram (please refer to ref. 25) indicate the leached W is in the form of WO_4^{2-}.

Supplementary Fig. 55 a LSVs of $NiMoO_4$-TA_x scanned in 1 M KOH + 0.5 M urea (x represents the number of CV cycle treatment conducted in 1 M KOH before urea electrolysis test). **b** Comparison of the urea electrolysis performance of fully-activated $NiMoO_4$-TA ($NiMoO_4$-TA_{20}) and $NiWO_4$-TA ($NiMoO_4$-TA_{950}). When cycling in 1 M KOH, $NiMoO_4$-TA exhibits a relatively limited leaching chemistry (evidencing by the stable urea electrolysis performance after 10 CV cycles shown in Supplementary Fig. 55a) compared to that of $NiWO_4$-TA. This indicates the metal leaching chemistry varies with the leaching agents. Previous literature suggested Al displays even more restricted leaching chemistry compared to that of W and Mo.[29] Consequently, activated $NiMoO_4$-TA exhibits inferior catalytic activity than that of fully-activated $NiWO_4$-TA (Supplementary Fig. 55b). W is considered as an ideal leaching agent due to its active leaching chemistry.
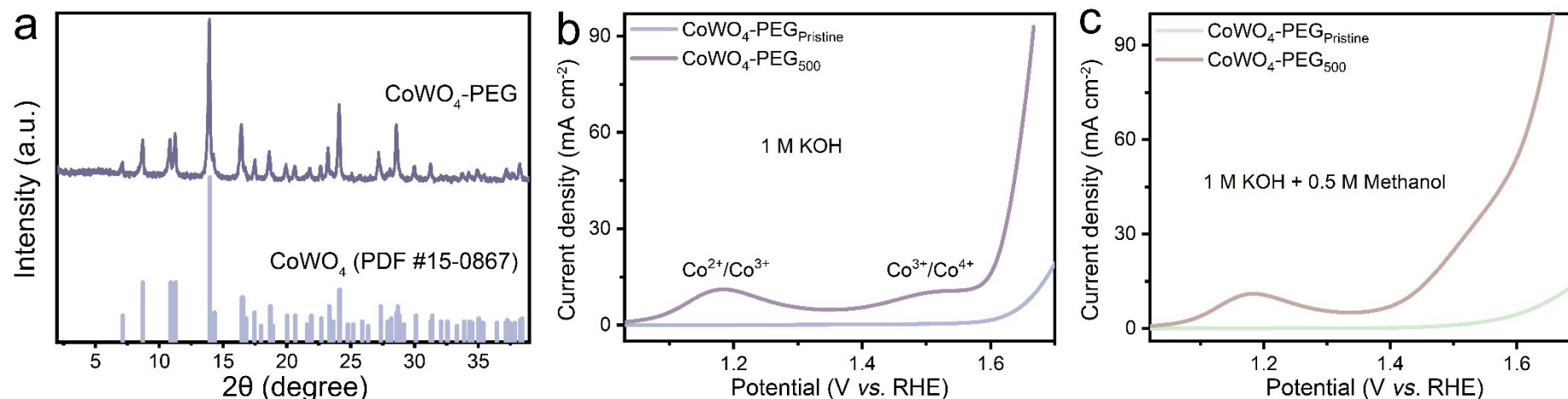
Supplementary Fig. 56 a Powder XRD pattern of $CoWO_4$-polyethylene glycol (PEG). **b, c** LSVs of pristine and activated $CoWO_4$-PEG evaluated in (**b**) 1 M KOH and (**c**) 1 M KOH + 0.5 M urea.

We next attempted to broad the application scope of the as-obtained theories beyond engineering of Ni chemistry and urea electrolysis performance. Therefore, $CoWO_4$-PEG was synthesized (Supplementary Fig. 56a) to check if its Co chemistry can be enhanced by electrochemical treatments. As shown in Supplementary Fig. 56b, boosts in both Co^{2+}/Co^{3+} and Co^{3+}/Co^{4+} transition peaks of $CoWO_4$-PEG have been witnessed after cycling in 1 M KOH. When employed as a MOR catalyst, the aged sample exhibits superior performance over that of the pristine material due to the more flexible Co redox behaviour (more specifically speaking it is the dynamic Co^{4+} that triggers the oxidation of methanol molecule according to previous literatures).[30] Hence, our W leaching theory has been proven appliable to elements beyond Ni in terms of improving their redox chemistry. Furthermore, based on the experimental observation and computational calculation, we believe any metals whose oxides can react with either acid or alkali can be used as leaching agents. In other word, we propose a concept of reconstructable bi- or multi-component oxides whose formula are written as follows:

$$A_xB_yO_z-C$$

Where A represents the metals who possess high catalytic activity towards a certain reaction when at a high valence state (*e.g.* Ni^{3+} for UOR). B represents the metals that can be leached with the help from electrochemical treatments in a proper medium (*e.g.* acidic oxide in base electrolyte or basic oxide in acidic electrolyte). C represents conductive substrates that can help exposing more of the metal oxides to the electrolyte.
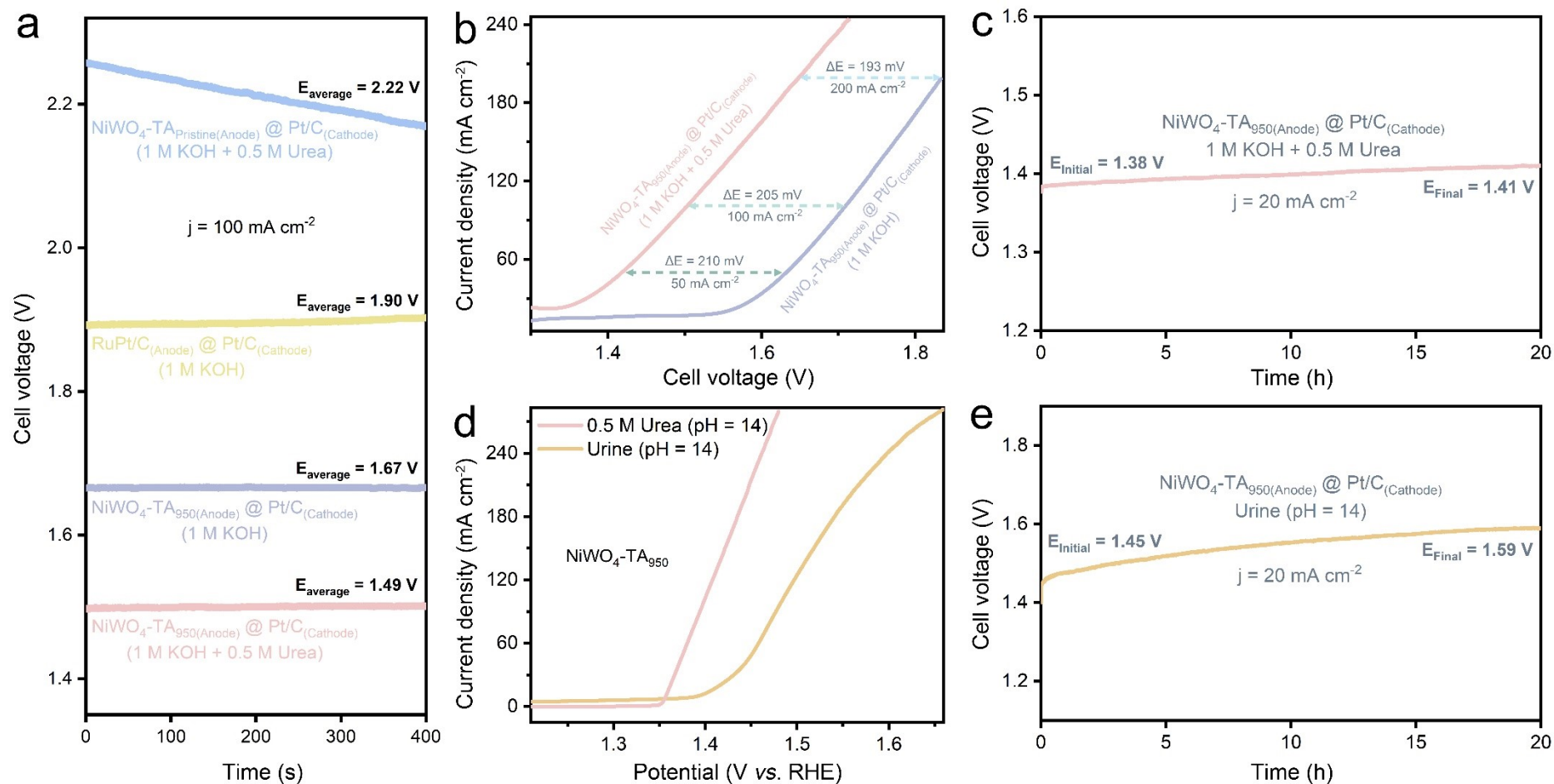
Supplementary Fig. 57 a Cell potential as function of time for various two-electrode electrolysers with different anode catalysts at a current density of 100 mA cm^{-2}. **b** Comparison of polarization curves of two-electrode urea and water electrolysers. **c** Galvanostatic measurement of a urea electrolyser with NiWO$_4$-TA$_{950}$ as the anode and Pt/C as the cathode at a constant current density (20 mA cm^{-2}) for 20 h. **d** LSVs of NiWO$_4$-TA$_{950}$ in 1 M KOH with 0.5 M urea or human urine in a three-electrode cell. **e** Galvanostatic measurement of a urine electrolyser with NiWO$_4$-TA$_{950}$ as the anode and Pt/C as the cathode at a constant current density (20 mA cm^{-2}) for 20 h. The urine used for the electrochemical tests was collected from the same experimenter. To maintain a stable urea concentration of the electrolyte, the experimenter had a fixed daily dietary at least

3 days before the urine collection.

To confirm the supremacy of $NiWO_4$-TA_{950} in practical electrolysis applications, two-electrode electrolysers using commercial Pt/C as the cathode for hydrogen evolution and pristine/activated $NiWO_4$ or commercial RuPt/C catalyst as the anode were assembled. As illustrated in Supplementary Fig. 57a, the $NiWO_4$-TA_{950}@Pt/C urea electrolyser only requires a cell voltage of 1.49 V to achieve a 100 mA cm^{-2} current density, much lower than that of the RuPt/C@Pt/C water electrolyser (1.90 V), $NiWO_4$-TA_{950}@Pt/C water electrolyser (1.67 V), $NiWO_4$-$TA_{Pristine}$@Pt/C urea electrolyser (2.22 V) and most of electrolysers reported by previous papers (Supplementary Table 4). Such superb performance highlights its industrialization potential in H_2 generation. To better understand the thermodynamic and kinetic advantages of a urea electrolysis system over a water electrolyser, LSVs of the $NiWO_4$-TA_{950}@Pt/C electrolysers with the same cell configuration but different electrolytes were recorded. As can be seen from Supplementary Fig. 57b and 58, the urea electrolyser exhibits a ~200 mV smaller cell voltage than that of the water electrolyser under both low- and high-current density operation modes. Aside from catalytic activity, stability is another important factor for a electrolysis device. In the galvanotactic measurement for $NiWO_4$-TA_{950}@Pt/C urea electrolyser, no noticeable cell voltage increase can be observed over 20 h, confirming the rigid performance of the $NiWO_4$-TA_{950} catalyst.

It is crucial to emphasize that electrolysis of urea will release CO_2 which makes it inauspicious for carbon emission cutting. In addition, urea is a high-value, thus expensive chemical product, use of which to produce H_2 is economically unfavourable despite the excellent kinetics of urea electrolysis. To make the urea electrolysis system more environmental and economical friendly, we tried to replace artificial urea by human urine as the source of urea. The vigorous urine electrolysis kinetics shown in Supplementary Fig. 57d proves the feasibility of the proposed urine electrolysis in spite of its slightly inferior performance compared to that of urea electrolysis. Moreover, as presented in Supplementary Fig. 57e, 59 and 60, a urine electrolyser with $NiWO_4$-TA_{950} and Pt/C as the anode and the cathode, respectively successfully reduced the urea concentration in alkaline urine from 0.31 M to 0.22 M over a 20 h operation, revealing its utilization potential in domestic and industrial waste water treatment. However, the cell voltage required for achieving a 20 mA current density increased 150 mV in just a 20-hour operation which might be due to the degradation of the catalysts caused by impurities in the urine electrolyte. Further efforts are needed to develop more rigid catalyst or impurity-free urine

Supplementary Table 4 Comparison of alkaline urea electrolyser performance for $NiWO_4$-TA_{950} and previously reported anode electrocatalysts.

| Anode and cathode catalysts	Cell voltage (V) at 100 mA cm^{-2}	Subtract	Electrolyte	Reference
$NiWO_4$-TA_{950}@Pt/C	1.49	Carbon paper	1 M KOH + 0.5 M urea	This work
$NiWO_4$-$TA_{Pristine}$@Pt/C	2.22	Carbon paper	1 M KOH + 0.5 M urea	This work
NiClO-D@Pt/C	1.69	Nickel foam	1 M KOH + 0.33 M urea	Ref. 31[31]
NF/NiMoO-H$_2$@ NF/NiMoO-Ar	1.55	Nickel foam	1 M KOH + 0.5 M urea	Ref. 32[32]
Ni$_3$N/NF@Ni$_3$N/NF	1.42	Nickel foam	1 M KOH + 0.5 M urea	Ref. 33[33]
CoN/Ni(OH)$_2$@Pt/C	1.55	Nickel foam	1 M KOH + 0.5 M urea	Ref. 34[34]
CoS$_2$/MoS$_2$@CoS$_2$/MoS$_2$	1.54	Nickel foam	1 M KOH + 0.5 M urea	Ref. 35[35]
NiFeRh-LDH@NiFeRh-LDH	1.471	Nickel foam	1 M KOH + 0.33 M urea	Ref. 36[36]
V-Ni$_3$N/NF@V-Ni$_3$N/NF	1.543	Nickel foam	1 M KOH + 0.5 M urea	Ref. 37[37]
CoMn/CoMn$_2$O$_4$@ CoMn/CoMn$_2$O$_4$	1.68	Nickel foam	1 M KOH + 0.5 M urea	Ref. 38[38]
Co$_2$Mo$_3$O$_8$@Co$_2$Mo$_3$O$_8$	1.65	Cobalt foam	1 M KOH + 0.5 M urea	Ref. 39[39]
Ni-S-Se/NF@Ni-S-Se/NF	1.60	Nickel foam	1 M KOH + 0.5 M urea	Ref. 40[40]
NiFe(CN)$_6$	1.50	Nickel foam	1 M KOH + 0.33 M urea	Ref. 41[41]
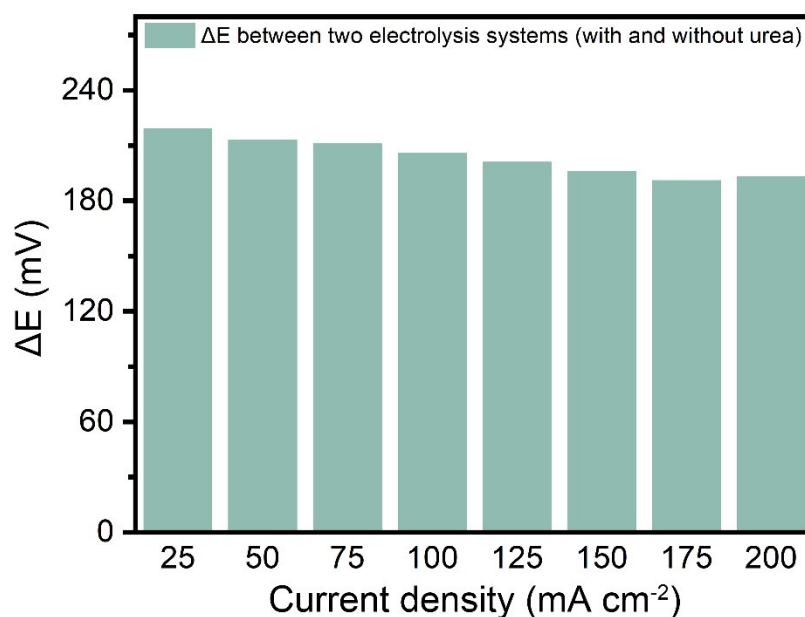
Supplementary Fig. 58 Cell voltage difference between water and urea electrolysers at various

current densities (derived from Supplementary Fig. 57b). The voltage difference between the urea and water electrolysers maintains at ~200 mV at both low and high cell current densities, confirming the superior performance of the urea electrolysis system over that of the water electrolysis system.
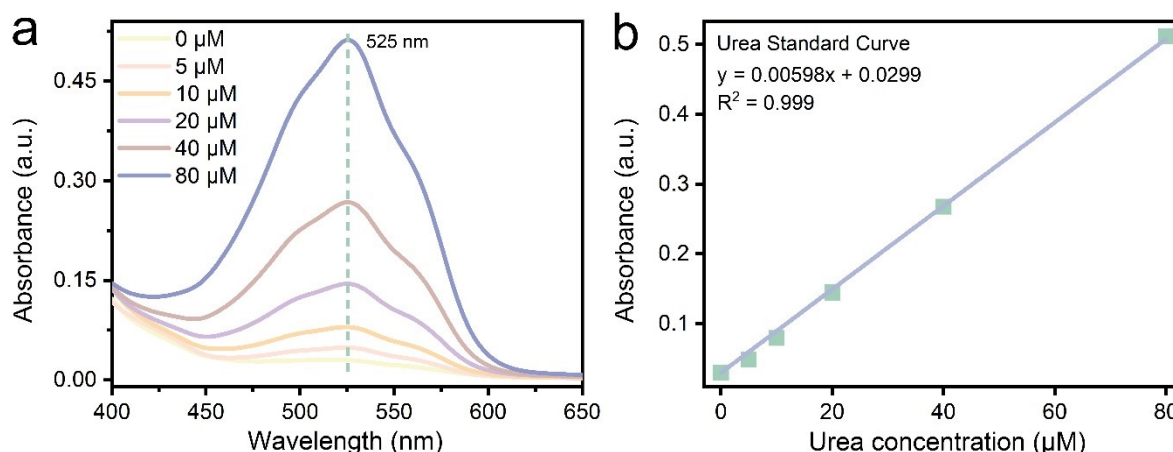
Supplementary Fig. 59 Quantification of urea concentration by diacetyl monoxime method.[42] **a** UV-Vis spectra of a series of standard solutions with urea concentrations of 0 μM, 5 μM, 10 μM, 20 μM, 40 μM and 80 μM, respectively. The colour reagents are prepared as follows. Solution A: 10 and 30 mL of concentrated phosphoric and sulfuric acid were first mixed with 60 mL distilled water. 10 mg ferric chloride was then added into the as-prepared mixture. Solution B: 500 mg diacetyl monoxime and 10 mg thiosemicarbazide were dissolved in 100 mL distilled water. In detail, 2 mL A, 1 mL B and 1 mL standard urea solution were mixed together and stirred at 85 °C for 20 min. Once cooled to room temperature, UV-Vis absorption spectrum of the mixed solution was measured at 525 nm. **b** Calibration curve used for calculation of urea concentrations (derived from Supplementary Fig. 59a).
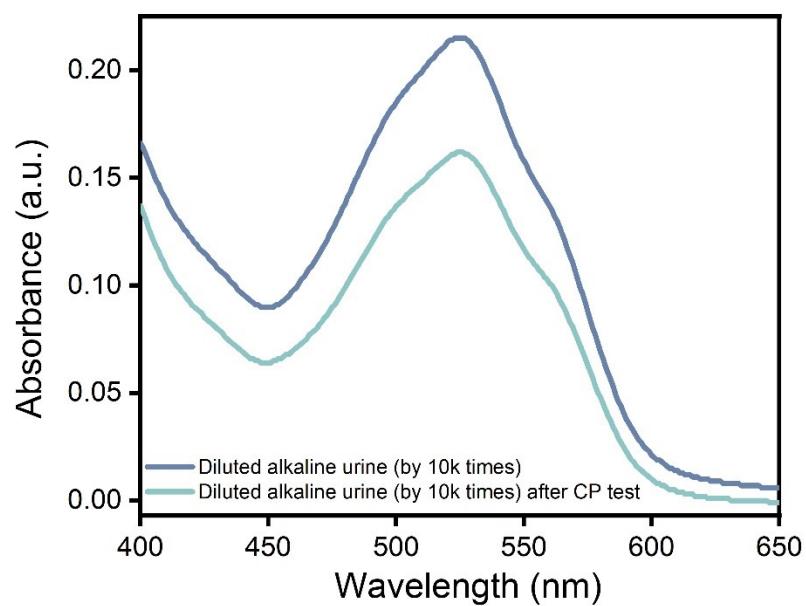
Supplementary Fig. 60 UV-Vis spectra of the alkaline urine electrolyte before and after urine electrolysis test for 20 h. The urea concentration decreased from 0.31 M to 0.22 M after the electrolysis, confirming the successful decomposition of urea.

References

1. Y. Dou, D. Yuan, L. Yu, W. Zhang, L. Zhang, K. Fan, M. Al-Mamun, P. Liu, C.-T. He and H. Zhao, *Adv. Mater.*, 2022, **34**, 2104667.
2. R. Farhat, J. Dhainy and L. I. Halaoui, *ACS Catal.*, 2020, **10**, 20-35.
3. J. Wang, L. Gan, W. Zhang, Y. Peng, H. Yu, Q. Yan, X. Xia and X. Wang, *Sci. Adv.*, 2018, **4**, eaap7970.
4. V. Maruthapandian, S. Kumaraguru, S. Mohan, V. Saraswathy and S. Muralidharan, *ChemElectroChem*, 2018, **5**, 2795-2807.
5. W. Yang, X. Yang, B. Li, J. Lin, H. Gao, C. Hou and X. Luo, *J. Mater. Chem. A*, 2019, **7**, 26364-26370.
6. Q. Zhang, F. M. D. Kazim, S. Ma, K. Qu, M. Li, Y. Wang, H. Hu, W. Cai and Z. Yang, *Appl. Catal. B*, 2021, **280**, 119436.
7. Y. Jin, S. Huang, X. Yue, H. Du and P. K. Shen, *ACS Catal.*, 2018, **8**, 2359-2363.
8. A. J. Tkalych, H. L. Zhuang and E. A. Carter, *ACS Catal.*, 2017, **7**, 5329-5339.
9. A. Govind Rajan, J. M. P. Martirez and E. A. Carter, *J. Am. Chem. Soc.*, 2020, **142**, 3600-3612.
10. C. Genovese, M. E. Schuster, E. K. Gibson, D. Gianolio, V. Posligua, R. Grau-Crespo, G. Cibin, P. P. Wells, D. Garai, V. Solokha, S. Krick Calderon, J. J. Velasco-Velez, C. Ampelli, S. Perathoner, G. Held, G. Centi and R. Arrigo, *Nat. Commun.*, 2018, **9**, 935.
11. M. J. Eslamibidgoli, A. Groß and M. Eikerling, *Phys. Chem. Chem. Phys.*, 2017, **19**, 22659-22669.
12. R. Dovesi, A. Erba, R. Orlando, C. M. Zicovich-Wilson, B. Civalleri, L. Maschio, M. Rérat, S. Casassa, J. Baima, S. Salustro and B. Kirtman, *Wiley Interdiscip. Rev. Comput. Mol. Sci.*, 2018, **8**, e1360.
13. A. Kuzmin, A. Kalinko and R. Evarestov, *Open Phys.*, 2011, **9**, 502-509.
14. N. Doudin, S. Pomp, M. Blatnik, R. Resel, M. Vorokhta, J. Goniakowski, C. Noguera, F. P. Netzer and S. Surnev, *Surf Sci*, 2017, **659**, 20-30.
15. M. W. Lee and M. Meuwly, *Phys. Chem. Chem. Phys.*, 2013, **15**, 20303-20312.
16. V. Vchirawongkwin and B. Rode, *Chem. Phys. Lett.*, 2007, **443**, 152-157.
17. J. Wang, H. Jang, G. Li, M. G. Kim, Z. Wu, X. Liu and J. Cho, *Nanoscale*, 2020, **12**, 1478-1483.
18. F. H. Hsu, S. Y. Hsu, C. W. Pao, J. L. Chen, C. L. Chen, J. M. Chen and K. T. Lu, *Nanoscale*, 2020, **12**, 13388-13397.
19. S. Kreissl, R. Bolanz, J. Göttlicher, R. Steininger, M. Tarassov and G. Markl, *Am. Mineral.*, 2016, **101**, 2701-2715.
20. U. Jayarathne, P. Chandrasekaran, A. F. Greene, J. T. Mague, S. DeBeer, K. M. Lancaster, S. Sproules and J. P. Donahue, *Inorg. Chem.*, 2014, **53**, 8230-8241.
21. Y. Q. Jia, *J. Solid State Chem.*, 1991, **95**, 184-187.
22. R. Shannon, *Acta Cryst. Sect. A*, 1976, **32**, 751-767.
23. W. M. Haynes, *CRC Handbook of Chemistry and Physics, 95th Edition*, CRC Press, Hoboken, 2014.
24. M. Anik, *Corros. Sci.*, 2010, **52**, 3109-3117.
25. M. I. Nave and K. G. Kornev, *Metall. Mater. Trans. A*, 2017, **48**, 1414-1424.
26. Y.-s. Kim, D.-l. Bae, H. Yang, H.-s. Shin, G. W. Wang, J. J. Senkevich and T. M. Lu, *J. Electrochem. Soc.*, 2005, **152**, C89.
27. E. A. Kneer, C. Raghunath, S. Raghavan and J. S. Jeon, *J. Electrochem. Soc.*, 1996, **143**, 4095-4100.
28. W. Chen, L. Xu, X. Zhu, Y.-C. Huang, W. Zhou, D. Wang, Y. Zhou, S. Du, Q. Li, C. Xie, L. Tao, C.-L. Dong, J. Liu, Y. Wang, R. Chen, H. Su, C. Chen, Y. Zou, Y. Li, Q. Liu and S. Wang, *Angew. Chem. Int. Ed.*, 2021, **60**, 7297-7307.
29. T. Wu, S. Sun, J. Song, S. Xi, Y. Du, B. Chen, W. A. Sasangka, H. Liao, C. L. Gan, G. G. Scherer, L. Zeng, H. Wang, H. Li, A. Grimaud and Z. J. Xu, *Nat. Catal.*, 2019, **2**, 763-772.
30. M. Zhai, F. Chen, N. Wu, R. Guo, X. Zhang, T. Hu and M. Ma, *Appl. Surf. Sci.*, 2021, **545**, 149016.
31. L. Zhang, L. Wang, H. Lin, Y. Liu, J. Ye, Y. Wen, A. Chen, L. Wang, F. Ni, Z. Zhou, S. Sun, Y. Li, B. Zhang and H. Peng, *Angew. Chem. Int. Ed.*, 2019, **58**, 16820-16825.
32. Z.-Y. Yu, C.-C. Lang, M.-R. Gao, Y. Chen, Q.-Q. Fu, Y. Duan and S.-H. Yu, *Energy Environ. Sci.*, 2018, **11**, 1890-1897.

33. S. Hu, C. Feng, S. Wang, J. Liu, H. Wu, L. Zhang and J. Zhang, *ACS Appl. Mater. Interfaces*, 2019, **11**, 13168-13175.

34. Y. Cheng, F. Liao, H. Dong, H. Wei, H. Geng and M. Shao, *J. Power Sources*, 2020, **480**, 229151.

35. C. Li, Y. Liu, Z. Zhuo, H. Ju, D. Li, Y. Guo, X. Wu, H. Li and T. Zhai, *Adv. Energy Mater.*, 2018, **8**, 1801775.

36. H. Sun, W. Zhang, J.-G. Li, Z. Li, X. Ao, K.-H. Xue, K. K. Ostrikov, J. Tang and C. Wang, *Appl. Catal. B*, 2021, **284**, 119740.

37. R.-Q. Li, Q. Liu, Y. Zhou, M. Lu, J. Hou, K. Qu, Y. Zhu and O. Fontaine, *J. Mater. Chem. A*, 2021, **9**, 4159-4166.

38. C. Wang, H. Lu, Z. Mao, C. Yan, G. Shen and X. Wang, *Adv. Funct. Mater.*, 2020, **30**, 2000556.

39. K. Zhang, C. Liu, N. Graham, G. Zhang and W. Yu, *Nano Energy*, 2021, **87**, 106217.

40. N. Chen, Y.-X. Du, G. Zhang, W.-T. Lu and F.-F. Cao, *Nano Energy*, 2021, **81**, 105605.

41. S.-K. Geng, Y. Zheng, S.-Q. Li, H. Su, X. Zhao, J. Hu, H.-B. Shu, M. Jaroniec, P. Chen, Q.-H. Liu and S.-Z. Qiao, *Nat. Energy*, 2021, **6**, 904-912.

42. M. Rahmatullah and T. R. C. Boyde, *Clin. Chim. Acta*, 1980, **107**, 3-9.